CHARACTERISTICS AND DESIGN OF MICROSTRIP SQUARE RING ANTENNAS

By:

Seyed Pedram Mousavi Bafrooei

A Thesis

Submitted to the Faculty of Graduate Studies

in Partial Fulfillment of the requirements

for the Degree of

Master of Science

Department of Electrical and Computer Engineering

The University of Manitoba

Winnipeg, Manitoba, Canada.

© August, 1997

National Library of Canada
Bibliothèque nationale du Canada

Acquisitions and Bibliographic Services
Acquisitions et services bibliographiques

395 Wellington Street
Ottawa ON K1A 0N4
Canada

395, rue Wellington
Ottawa ON K1A 0N4
Canada

Your file Votre référence

Our file Notre référence

The author has granted a non-exclusive licence allowing the National Library of Canada to reproduce, loan, distribute or sell copies of this thesis in microform, paper or electronic formats.

L'auteur a accordé une licence non exclusive permettant à la Bibliothèque nationale du Canada de reproduire, prêter, distribuer ou vendre des copies de cette thèse sous la forme de microfiche/film, de reproduction sur papier ou sur format électronique.

The author retains ownership of the copyright in this thesis. Neither the thesis nor substantial extracts from it may be printed or otherwise reproduced without the author's permission.

L'auteur conserve la propriété du droit d'auteur qui protège cette thèse. Ni la thèse ni des extraits substantiels de celle-ci ne doivent être imprimés ou autrement reproduits sans son autorisation.

0-612-23434-7

Canada

THE UNIVERSITY OF MANITOBA

FACULTY OF GRADUATE STUDIES

*****

COPYRIGHT PERMISSION PAGE

CHARACTERISTICS AND DESIGN OF MICROSTRIP SQUARE RING ANTENNAS

BY

SEYED PEDRAM MOUSAVI BAFROOEI

A Thesis/Practicum submitted to the Faculty of Graduate Studies of The University of Manitoba in partial fulfillment of the requirements of the degree of

MASTER OF SCIENCE

Seyed Pedram Mousavi Bafrooei 1997 (c)

Permission has been granted to the Library of The University of Manitoba to lend or sell copies of this thesis/practicum, to the National Library of Canada to microfilm this thesis and to lend or sell copies of the film, and to Dissertations Abstracts International to publish an abstract of this thesis/practicum.

The author reserves other publication rights, and neither this thesis/practicum nor extensive extracts from it may be printed or otherwise reproduced without the author's written permission.

To my parents:

for their life time efforts to teach

me the value of knowledge and wisdom

ACKNOWLEDGMENT

I would like to express my sincere gratitude to my supervisor Professor Lotfollah Shafai for his knowledge, insight, enthusiasm, and continuous encouragement and support through out this research.

I would like also to thank Dr. E. Bridges, and Dr. N. Sepehri for serving in my committee and for their constructive criticisms and suggestions in the preparation of the final report.

Thanks are owed to Mr. B. Tabachnick for his technical help.

I am thankful to Ms. S. Girardin for extending help whenever it was needed.

I am also thankful to my friend Dr. R. Chaitanya Babu for his usefull comments

Assistance by Professor F. Hodjat-Kashani, and Dr. A.A. Salehi, has been instrumental in my acceptance at the University of Manitoba, for which I am greatly indebted.

Financial support during this study was provided by a grant from the Natural Science and Engineering Research Council of Canada (NSERC), their contribution is greatly appreciated.

Last, but not least, endless thanks to the members of Fallah-Rad family; Amir, Shahnaz, Mehran, and Nazanin who with their open arms and warm hearts made me feel at home in Winnipeg. Their continuous moral support helped me achieving my goals at school.

ABSTRACT

In this thesis a method for miniaturisation of a microstrip patch antenna without degrading its radiation characteristics is investigated. It involves perforating the patch to form a microstrip square ring antenna, which is investigated numerically and experimentally. The ring geometry introduces additional parameters to the antenna that can be used to control its impedance, resonance frequency, and bandwidth. For a single square ring increasing the size of perforation increases its input impedance, but decreases the resonance frequency and bandwidth. It has no effect on directivity of the antenna.

A novel transmission-line model is also developed to predict the resonance frequency of a single layer ring antenna. The results of this model show good agreement with those generated by Ensemble software.With the help of the transmission-line model the possibility of using a single stub to decrease the resonance frequency of the patch is also investigated.

To match the antenna to a transmission line and also enhance its bandwidth, the ring is stacked by a square patch or another square ring. The computed results are compared with experimental data and again good agreement is obtained.

TABLE OF CONTENT

AKNOWLEDGMENT i

ABSTRACT ii

LIST OF FIGURES vi

LIST OF TABLES xiii

Chapter 1 INTRODUCTION 1

(1.1) Preface 1

(1.2) Background 2

(1.3) Objective of This Study 4

(1.4) Simulation Tool 5

(1.5) Model Based on The Electric Surface Current 5

(1.5.1) Geometry of the model and boundary conditions 5

(1.5.2) Potentials for the diffracted fields 8

(1.5.3) Green's functions 9

(1.5.4) Mixed potential integral equation (MPIE) 12

(1.6) Method of Moments 12

(1.6.1) Current and charge cells 13

(1.6.2) Basis functions 15

(1.6.3) Discrete Green's function 16

(1.6.4) Test functions 18

(1.6.5) The matrix equations. 18

Chapter 2 CHARACTERISTIC OF SINGLE LAYER MICROSTRIP SQUARE RING ANTENNAS 20

(2.1) Introduction 20

(2.2) Single Layer Square Ring Resonator. 21

(2.2.1) Resonance frequency. 22

(2.2.2) Input impedance 23

(2.2.3) Total Q-factor and impedance bandwidth. 25

(2.2.4) Directivity 28

(2.2.5) Radiation patterns 29

(2.2.6) Current Components 29

(2.2.7) The effect of moving feed probe. 34

(2.3) Miniaturization of Microstrip Antenna with Single Stub 35

(2.4) Summary 40

Chapter 3 RESONANCE FREQUENCY PREDICTION USING TRANSMISSION LINE MODEL 42

(3.1) Introduction 42

(3.2) The Suggested Model. 43

(3.2.1) Effective dielectric constant 46

(3.2.2) Effective length. 46

(3.2.3) Expression for the self-susceptance B_s. 47

(3.2.4) Expression for the self-conductance G_s 47

(3.2.5) Expression for mutual-admittance 50

(3.2.6) Admittance matrix 53

(3.3) Results 57

(3.4) Summary 59

Chapter 4 STACKED RING REESONATORSFOR BANDWIDTH ENHANCMENT 60

(4.1) Introduction 60

(4.2) Theory 61

(4.3) Stacked Ring-Patch 63

(4.4) Stacked Ring-Ring 70

(4.4.1) The effect of changing H_1 76

(4.4.2) The effect of changing H_2 81

(4.4.3) The effect of using different substrates 83

(4.5) Summary 85

Chapter 5 CONCLUSION 86

(5.1) Summary 86

(5.2) Future Research 87

REFERENCES 89

LIST OF FIGURES

Figure 1.1 General view of a microstrip antenna and vertical cut in the y=0 plane. Superscripts e and d refer to the excitation fields and to the scattered fields [29] . . 7

Figure 1.2 Horizontal electric dipole (HED) on a microstrip substrate[27]. 11

Figure 1.3 Segmentation of the patch in elementary charge and current cell 14

Figure 1.4 x-directed current cell centred at r=0 and its associate surface current density J_{sx} and surface charge density q_s 14

Figure 2.1 Geometry of printed loop, ring and microstrip patch antennas. 21

Figure 2.2 Microstrip square ring configuration 22

Figure 2.3 Measured and calculated resonance frequency variation with W_2,W_1=30 mm ε_r=2.5, h=1.59 mm. 24

Figure 2.4 Calculated resonance frequency for various substrate thickness W_1=30 mm ε_r=2.5 24

Figure 2.5 Measured and calculated input impedance variation with W_2/W_1, W_1=30 mm, ε_r=2.5, h=1.59 mm. 26

Figure 2.6 Calculated input impedance for various substrate thicknesses, W_1=30 mm, ε_r=2.5 26

Figure 2.7 Calculated Bandwidth for various substrate thicknesses, W_1=30 mm, ε_r=2.5 27

Figure 2.8 Calculated Total Q-factor for various substrate thicknesses, W_1=30 mm, ε_r=2.5 27

Figure 2.9 Calculated directivities for several substrate thicknesses, W_1=30 mm, ε_r=2.5 28

Figure 2.10 H and E-plane radiation patterns for h=1.59 mm and W_2/W_1=0.5, W_1=30 mm, ε_r=2.5 30

Figure 2.11 Normalized cross-polarization in the E-plane, for ring antenna with W_1=30 mm, ε_r=2.5 31

Figure 2.12 Normalized cross-polarization in the H-plane, for ring antenna with W_1=30 mm, ε_r=2.5 31

Figure 2.13 H-plane 3 dB beamwidths, for ring antenna with W_1=30 mm, ε_r=2.5 . . . 32

Figure 2.14 E-plane 3 dB beamwidths, for ring antenna with W_1=30 mm, ε_r=2.5 . . . 32

Figure 2.15 Real and imaginary current components for ring antennas of W_2/W_1=0.5, W_1=30 mm, ε_r=2.5. 33

Figure 2.16 Input impedance vs. probe position for different ring sizes, Y_p = -13mm, W_1=30 mm, ε_r=2.5. 36

Figure 2.17 Resonance frequency vs. probe position for different ring size, $Y_p = -13$ mm, W_1=30 mm, ε_r=2.5. 36

Figure 2.18 Cross-polarization vs. probe position in H-plane, $Y_p = -13$ mm, W_1=30 mm, ε_r=2.5 37

Figure 2.19 Cross-polarization vs. probe position in E-plane, $Y_p = -13$ mm, W_1=30 mm, ε_r=2.5 37

Figure 2.20 Input impedance vs. probe position in y-direction, $X_p = 0$ mm, W_1=30 mm, ε_r=2.5 38

Figure 2.21 Resonance frequency vs. probe position in y-direction, $X_p = 0$ mm, W_1=30 mm, ε_r=2.5 38

Figure 2.22 Locus of input impedance on Smith chart for a patch with W_1=30 mm, ε_r=2.5 fed by 50Ω transmission line 39

Figure 2.23 Configuration of a patch antenna with single stub 39

Figure 3.1 Configuration of the square ring with radiation slots 44

Figure 3.2 Transmission line model for square ring 45

Figure 3.3 Equivalent slot radiator in an infinite, perfectly conducting plane. 47

Figure 3.4 Slot self conductance as a function of slot width 50

Figure 3.5 Configuration for coupling calculations between rectangular slots 52

Figure 3.6 Normalized mutual conductance between two slots in E-plane. 55

Figure 3.7 Normalized mutual susceptance between two slots in E-plane 55

Figure 3.8 Ensemble and transmission line model results for resonance frequency (h=0.8 mm, ε_r=2.5) 57

Figure 3.9 Ensemble and transmission line model results for resonance frequency (h=1.59 mm, ε_r=2.5) 58

Figure 3.10 Ensemble and transmission line model results for resonance frequency (h=3.18 mm, ε_r=2.5). 58

Figure 4.1 Stacked dual-resonator configuration. 62

Figure 4.2 Equivalent circuit to model input impedance of Figure 4.1 62

Figure 4.3 Configuration of a stacked ring-patch antenna. 63

Figure 4.4 Computed return loss of the stacked ring-patch configuration, W_2/W_1=15/30, W_3=47 mm, H_1=1.6 mm, H_2=5 mm, ε_{r1} =2.5, ε_{r2} = 1.05 64

Figure 4.5 Measured return loss of the stacked patch configuration, of Figure 4.4 . . . 64

Figure 4.6 (a) Computed, (b) measured input impedance of ring-patch antenna of Figure 4.4. 65

Figure 4.7 Computed (a) H-plane and (b) E-plane radiation patterns with normalized cross-polarization of Figure 4.4. 66

Figure 4.8 Measured E-plane radiation pattern for ring-patch antenna. of Figure 4.4 (ground plane is 100 mm) 67

Figure 4.9 Measured H-plane radiation pattern of ring-patch antenna of Figure 4.4 (ground plane is 100 mm) 68

Figure 4.10 Real and imaginary normalized surface current components (a) Real current component on ring, $I_{Rmax} = 0.002974$ (b) Imaginary current component on ring, $I_{Imax} = 0.010179$ (c) Real current component on patch, $I_{Rmax} = 0.008304$ (d) Imaginary current component on patch, $I_{Imax} = 0.003236$. 69

Figure 4.11 Configuration of stacked ring-ring antenna 70

Figure 4.12 Computed return loss of the stacked rings, W_2/W_1=14/30, W_4/W_3=22/36,H_1=1.6 mm, H_2=5 mm, ε_{r1} =2.5, ε_{r2} = 1.05 71

Figure 4.13 Measured return loss of the stacked rings of Figure 4.12. 71

Figure 4.14 (a) Computed, (b) measured input impedance of stacked ring antenna of Figure 4.12 72

Figure 4.15 Computed (a) H-plane (b) E-plane radiation pattern of Figure 4.12 73

Figure 4.16 Measured H-plane radiation pattern with cross-polarization for Figure 4.12 (ground plane is 100 mm) 74

Figure 4.17 Measured E-plane radiation pattern with cross-polarization for Figure 4.12 (ground plane is 100 mm) 75

Figure 4.18 Real and imaginary normalized surface current components (a) Real current component on lower ring, $I_{Rmax} = 0.005615$ (b) Imaginary current component on lower ring, $I_{Imax} = 0.009578$ (c) Real current component on upper ring, $I_{R\text{-}max} = 0.019038$ (d) Imaginary current component on upper ring, $I_{Imax} = 0.002046$. 76

Figure 4.19 (a) Return loss and (b) input impedance for a stacked ring-ring antenna with H_1=3.2 mm. 77

Figure 4.20 (a) H-plane, (b) E-plane radiation pattern of Figure 4.19. 78

Figure 4.21 (a) Return loss, (b) input impedance for a stacked ring-ring configuration with H_1=0.8 79

Figure 4.22 (a) H-plane, (b) E-plane radiation pattern of Figure 4.21. 80

Figure 4.23 Return loss for a stacked ring-ring antenna H_2=9 mm and H_1=0.8mm, W_2/W_1=30/60, W_4/W_3=45/90, ε_{r1} =2.5, ε_{r2} = 1.05 81

Figure 4.24 Input impedance for antenna of Figure 4.23. 82

Figure 4.25 (a) H-plane, (b) E-plane radiation pattern for Figure 4.23 82

Figure 4.26 Return loss for two layer ring-ring antenna with ε_{r1}=ε_{r2}=1.05, H_2=18 mm and H_1=9 mm, W_2/W_1=350/700, W_4/W_3=230/700. 83

Figure 4.27 Input impedance for two layer ring for antenna of Figure 4.26 84

Figure 4.28 (a) H-plane, (b) E-plane radiation pattern for Figure 4.26 84

LIST OF TABLES

Table 1.1 Results of single stub matching 40

Table 1.2 Variation of ring antenna parameters with its width 41

Chapter 1

INTRODUCTION

1.1.Preface

The concept of microstrip antenna discussed by Deschamps in 1953 [1] has been studied and developed extensively since 1974 [2,3]. They are suitable for many applications where, low profile, light weight, low cost, simple geometry, compatibility with integrated circuit and conformability in mounting on the host body are required. Some of these applications are in mobile radio, satellite communications, radars, missile telemetry, biomedical radiators and reflector feeds. Due to the growing demand for these antennas, numerous efforts have been made to reduce their disadvantages, such as the narrow bandwidth, high loss, and practical array gain limits. However, in spite of these innovations, the demand for low profile antennas is increasing. This in turn, means that more precise mathematical models and new software tools are needed to predict the performance of innovative structures and consider practical aspects.

A novel structure that has not been studied well yet is the square ring patch, which is geometrically an intermediate configuration between a printed loop and solid patch [4]. Depending on the selected geometry, it provides additional parameters that can be used to control its resonance frequency and input impedance.

This study is an attempt to miniaturise microstrip patch antennas by using micros-

trip square rings and tuning stubs. The transmission line model is used to predict the resonance frequency of a single layer ring. The possibility of using stacked two layer rings or two layer ring-patch configuration for increasing the antenna bandwidth is also considered.

1.2.Background

The rectangular patch is the most commonly used microstrip antenna, [5] and is characterised by its length and width. Three analytic methods have been developed to analyse this type of patches and they are: the cavity model [6], Transmission line model [7], and the modal expansion model . A large number of numerical techniques [8] have also been developed which are based on the method of moment, finite element, and the finite difference time domain, etc. Their far field radiation pattern, losses, quality factor, input impedance, and the resonance frequency are well documented and reported in [9,10,11]. Another configuration is the circular patch antenna, and its geometry is characterised by a single parameter namely, the radius. Its mathematical analysis involves Bessel functions. The expression for the far field radiation pattern, losses, quality factor and input impedance of these are also documented and reported by Bahl, and Baharita [12] and Shafai, and Antoszkrewicz [13].

The annular ring was first studied by Bergman and Schultz [14] as a travelling wave antenna. It has also been used as a resonator [15,16] and as a radiator in medical applications [17]. Mink [18] studied the resonant behaviour of a microstrip annular ring. It was found that for the ring resonator, the resonant frequency of the lowest order mode can

be much lower than that of the circular disc of approximately the same size. This fact could be appreciated physically by noting that, for the lowest order mode the average path length travelled by the current in the annular ring is much larger than the circular disk. There are other features associated with this patch. First, it is possible to combine the annular ring with a second microstrip element, such as a circular disc within its central aperture, to form a compact dual band antenna system [18]. Second, the separation of the modes can be controlled by the ratio of the outer to inner radii. Finally, it has been found that, when operating in one of the higher-order broadside-modes, i.e. TM_{12}, the impedance bandwidth is several times larger than that achievable in other patches of comparable dielectric thickness.

The idea of stacking two elements came soon after the original microstrip antenna was proposed. A stacked circular antenna was constructed [19] using two discs etched on different boards, feeding the lower disc by a coaxial connector through the ground plane. Two distinct resonances were observed, and it was found that the lower resonant frequency was relatively constant over a range of different diameters, while the second resonance was highly dependent on them. However up until 1979, making a precise design was a difficult task. Nevertheless since 1986 many theoretical and experimental studies have been published, reporting results with bandwidth up to 26 percent (SWR=2), using contiguous stacked elements [20,21],. Multilayer microstrip patch antennas with radiating elements of various geometries were also realized [22], revealing some interesting features. Larger bandwidths can also be obtained by optimizing the coupled patch heights, or selecting different substrates.

Between 1974 and 1988, the evolution of the transmission line type modelling was mainly to the manner in which different components are calculated. The earliest model is the model for a microstrip patch fed by a microstrip line at one of its edges introduced by Munson in 1974 [3]. It only takes into account the two slots at the ends of the transmission line and calculates their admittances based on known expressions for thin slots of infinite length and with uniform field distribution. Concerning radiation, details are only given about the way in which the gain of the antenna has to be calculated. Mutual coupling is neglected completely. Starting from this model, a whole range of authors have introduced various improvements. One of the first improvements was the introduction of a more rigorous description of the two slot model. Derneryd [23] used the well-known radiation field of a slot of small width and finite length and with uniform field distribution to determine its self-conductance. The self-susceptance is derived from the end effect as modelled by Hamerstad [24]. Derneryd was also the first author who considered mutual coupling. The expression given by him for the self-conductance and the mutual conductances are integral expressions.

1.3.Objective of This Study

The purpose of this research is to miniaturise the physical length of microstrip patch antennas without affecting their radiation performances. Mixed potential integral equations in conjunction with method of moment is used in the first part of this study that computes the input impedance, radiation pattern, directivity, and surface current distribution. Then, the characteristics of single microstrip square ring antenna are investigated. It

is found that, this kind of patch is inherently narrow band.

Shafai [25] increased the bandwidth of the ring by increasing its substrate height and using large inductive feed probes. In the present study the bandwidth is increased by stacking a solid patch or another ring on the first ring.

An improved transmission line model is developed to predict the resonance frequency of a single layer ring. With the help of this model the possibility of using a single stub for decreasing the resonance frequency of the patch is also investigated. To confirm the numerical results, adequate experiments are also conducted and compared.

1.4.Simulation Tool

Most of the simulations in this study have been done by "Ensemble 4.02" of "Boulder Microwave Technologies, Inc."[26]. This software is based on a fullwave approach using the mixed potential integral equation formulation in conjunction with the method of moments. A brief discussion of the method is provided, which is based on the work of Mosig given in [8].

1.5.Model Based on The Electric Surface Current

1.5.1. Geometry of the model and boundary conditions

In Figure 1.1 the substrate is assumed to extend to infinity in the transverse direction and is made of nonmagnetic, isotropic, homogeneous material which can be lossy.

The ground plane is also infinite and the patch has no thickness and may have ohmic losses[8].

The patch is denoted by surface S_0. The interface of two dielectric media is called S. Indexes 1 and 2 are used, respectively, for the region above substrate, usually the air, and for the substrate itself. so

$$\varepsilon_1 = \varepsilon_0, \qquad z > 0 \tag{1.1}$$

$$\varepsilon_2 = \varepsilon_0 \varepsilon_r \qquad -h < z < 0$$

where h is the substrate thickness and $\mu_1 = \mu_2 = \mu_0$

The excitation fields can be the fields of a plane wave coming from infinity or the local fields created by the source like probe located on the microstrip structure. In each case they produce surface currents on the upper side of the ground plane and on both sides of the patch. Due to the zero thickness of the patch, it is modelled as a sheet of current J_s whose value at any point is the algebraic sum of the upper and lower surface currents J_{s1} and Js_2 existing at z=0+ and z=0-. These induced currents produce scattered electromagnetic fields which add to the excitation fields to give the total fields $\vec{E}, \vec{H}$ existing in the entire space.

The boundary conditions on the interface of dielectric and air are:

$$\vec{e}_z \times \left(\vec{E}_1 - \vec{E}_2 \right) = 0 \tag{1.2}$$

$$\vec{e}_z \times \left(\vec{H}_1 - \vec{H}_2 \right) = 0 \tag{1.3}$$

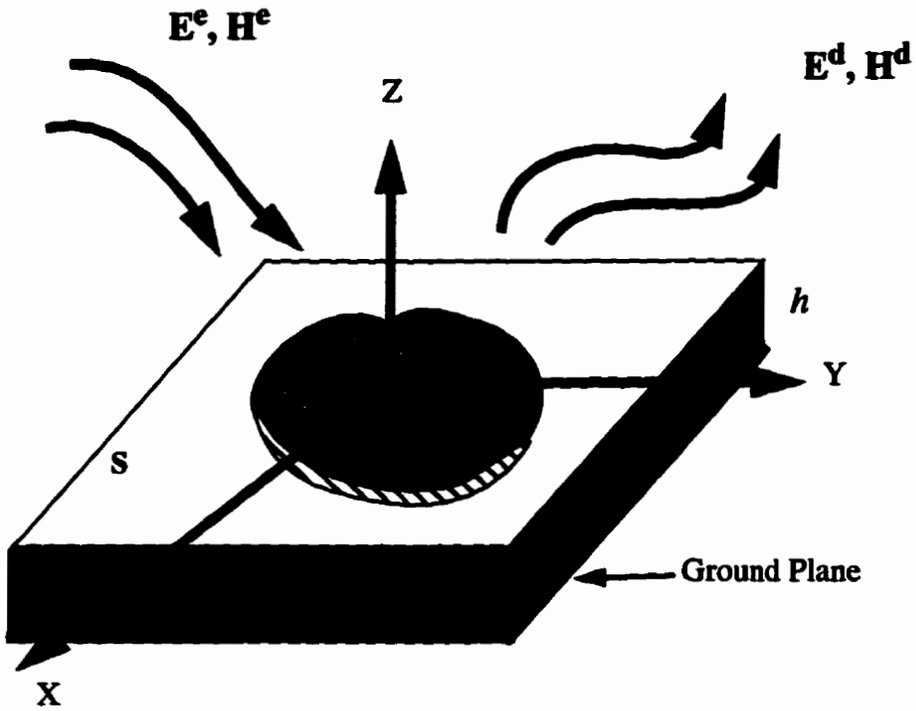

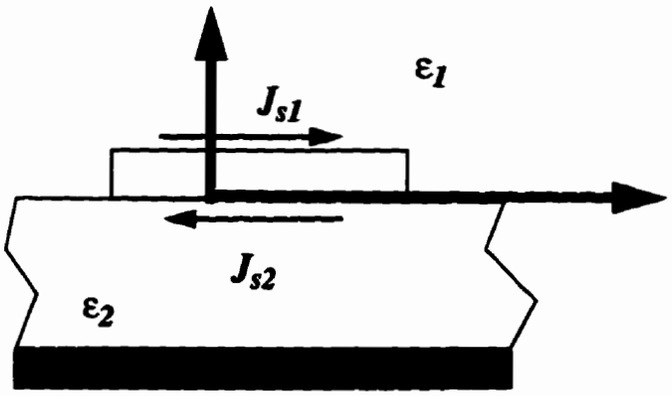

Figure 1.1: General view of a microstrip antenna and vertical cut in the y=0 plane. Superscripts e and d refer to the excitation fields and to the scattered fields [29]

Assuming that the patch and ground plane are perfect conductor, the boundary conditions for the upper side of S_0 are:

$$\hat{e}_z \times \vec{E}_1 = 0; \quad \hat{e}_z \times \vec{H}_1 = \vec{J}_{s1} \tag{1.4}$$

and, on the lower side they are

$$\hat{e}_z \times \vec{E}_2 = 0; \quad \hat{e}_z \times \vec{H}_2 = \vec{J}_{s2} \tag{1.5}$$

Combining the above pair of equations one find

$$\vec{e}_z \times \left(\vec{E}_1 - \vec{E}_2 \right) = 0 \tag{1.6}$$

$$\vec{e}_z \times \left(\vec{H}_1 - \vec{H}_2 \right) = \vec{J}_{s1} + \vec{J}_{s2} \tag{1.7}$$

Because the excitation fields are assumed to be continuous, the above boundary conditions show the diffracted tangential electric field is continuous across the patch, while the jump in diffracted tangential magnetic fields equals the total surface current on the patch.

The boundary conditions for the ground plane (z=-h) are

$$\hat{e}_z \times \vec{E}_2 = 0: \tag{1.8}$$

$$\hat{e}_z \times \vec{H}_2 = \vec{J}_s \tag{1.9}$$

1.5.2. Potentials for the diffracted fields

Since there are no volume sources in this model, the diffracted fields satisfy the homogeneous Maxwell's curl equations [27]:

$$\nabla \times \vec{E}^d = -j\omega\mu_0 \vec{H}^d \tag{1.10}$$

$$\nabla \times \vec{H}^d = j\omega\varepsilon \vec{E}^d \tag{1.11}$$

By introducing the scalar and vector potential for the diffracted fields, we can simplify the problem:

$$\vec{H}^d = \left(\frac{1}{\mu_0}\right) \nabla \times \vec{A} \tag{1.12}$$

$$\vec{E}^d = -j\omega\vec{A} - \nabla V \tag{1.13}$$

These two potentials are related to each other by Lorentz's gauge:

$$\nabla \bullet \vec{A} + j\omega\mu_0\varepsilon V = 0 \tag{1.14}$$

Inserting equations (1.12)-(1.14) into Maxwell's equations, homogeneous Helmoltz's equations for potentials are obtained:

$$\nabla^2 \vec{A} + k_i^2 \vec{A} = 0 \tag{1.15}$$

$$\nabla^2 V + k_i^2 V = 0 \tag{1.16}$$

where $k_i = \omega\,(\mu_0\varepsilon_i)^{1/2}$ is the wavenumber in medium i.

1.5.3. Green's functions

In Figure 1.2 we consider an arbitrarily oriented Hertz dipole of moment $\vec{I}dl$ located at the point $\vec{r}'$. The vector potential at the point $\vec{r}$ due to this dipole is given by the linear relationship

$$d\vec{A}(\vec{r}) = \overline{\overline{G}}_A(r|r') \bullet I(r')\, d\vec{l} \tag{1.17}$$

where $\overline{\overline{G}}_A$ is a three-dimensional dyadic Green function. For a given direction $\vec{t}$ of the Hertz dipole, there are three possible components of the dyadic related to the potential, namely $\overline{\overline{G}}_A^{st}$ $(s=x,y,z)$, where s is the component of the vector potential existing at point $\vec{r}$.

For a microstrip antenna the solution is to include in the Green's functions effect of the dielectric substrate and of the ground plane. Therefore, the Green's functions must satisfy the boundary condition of equations (1.2),(1.3), (1.8), and (1.9). By meeting these conditions, the boundary conditions for the magnetic fields are satisfied.

Because of the complexity of the problem there is no closed analytical expression for it. The method of evaluation of the function numerically is fully detailed in references [27,31].

Due to the linearity of Maxwell's equations, for an arbitrary current distribution, the vector potential can be written as a superposition integral involving the corresponding dyadic Green's function:

$$\vec{A}(\vec{r}) = \int_{S_0} \overline{\overline{G}}_A(r|r') \bullet \vec{J}(r')\, dS' \tag{1.18}$$

Introducing in the Lorentz's gauge the integral equation for $\vec{A}$ one gets

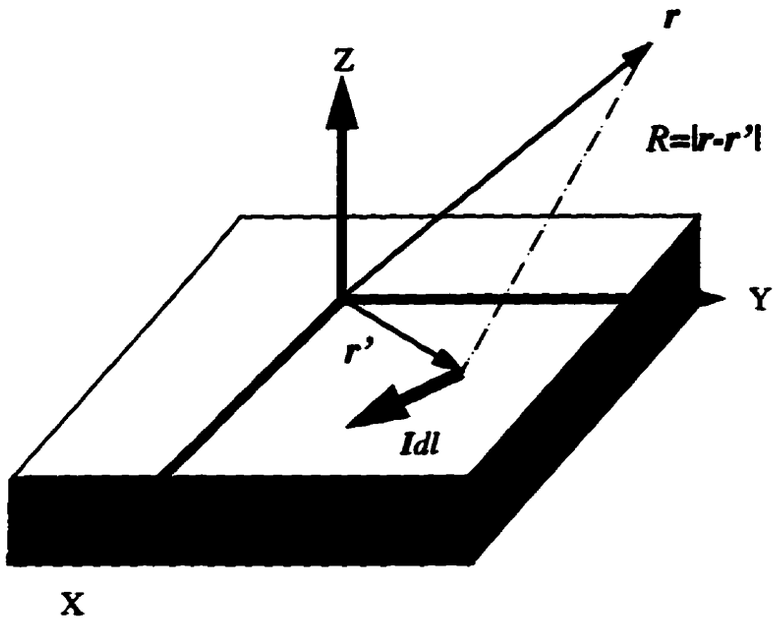

Figure 1.2: Horizontal electric dipole (HED) on a microstrip substrate[27]

$$j\omega\mu\varepsilon V(\vec{r}) = -\int_{S_0} \left[\nabla \bullet \overline{\overline{G}}_A(r|r')\right] \bullet J_s(r')\, dS' \tag{1.19}$$

In electrostatics the scalar potential depends only on the charge density q_s through the scalar Green's function G_v:

$$V(\vec{r}) = \int_{S_0} G_V(r|r')\, q_s(r')\, dS' \tag{1.20}$$

where the surface charge on the surface of the conductors is linked to the surface current J_s via the continuity equation:

$$\nabla \bullet J_s + j\omega q_s = 0 \tag{1.21}$$

1.5.4. Mixed potential integral equation (MPIE)

The diffracted fields from the potentials of equations (1.18)and (1.20) satisfy Maxwell's equations and the boundary condition of the problem. The next step is to relate these fields to the excitation fields via the equations (1.4) and (1.5). By taking into account the ohmic losses on the patch, the total tangential electric field is proportional to the total surface current:

$$\vec{e}_z \times \left(\vec{E}^e + \vec{E}^d \right) = \vec{e}_z \times Z_s \vec{J}_s \tag{1.22}$$

or, replacing by the potentials:

$$\vec{e}_z \times \left(j\omega \vec{A} + \nabla V + Z_s \vec{J}_s \right) = \vec{e}_z \times \vec{E}^e \tag{1.23}$$

where Z_s is a surface impedance which is due to the finite conductivity of the patch.

Finally, introducing the integral form of the potentials in equation (1.23), one gets the final expression for the mixed potential integral equation:

$$\vec{e}_z \times \left(j\omega \int_{S_0} \overline{G}_A \bullet \vec{J}_s dS' + \nabla \int_{S_0} G_V q_s dS' + Z_s \vec{J}_s \right) = \vec{e}_z \times \vec{E}^e \tag{1.24}$$

1.6.Method of Moments

In order to apply the mixed potential integral equation to irregular microstrip shapes, one needs a very flexible numerical technique and the method of moment has been selected. This technique transforms the integral equation into a matrix algebraic equation that can be easily solved by a computer [31].

1.6.1. Current and charge cells

A successful technique should decompose any arbitrary shape of the patch into small elementary cells and define simple approximations for the surface current on each cell. Ensemble uses both rectangular and triangular shapes for the elementary cells.

To eliminate the use of basis functions defined over the entire domain, no a priori assumptions will be made for the distribution of currents. The best selection for the surface current J_s is rooftop functions. To implement these functions, the patch boundary is replaced by a Manhattan-type polygonal [27] line Figure 1.3.

The patch's surface is divided into rectangular cells, called charged cells, which are all chosen of equal size, if possible. The dimension of the cell is $a \times b$. The equality of the cell sizes considerably decrease the length of the computations.

An x-directed (y-directed) current cell will be formed by two adjacent charge cells sharing a common border perpendicular to the x-direction (y-direction). An automatic overlapping of current cells is obtained in this manner, in which a charge cell may belong to up to four different current cells. The number of charge cells is dependent on the number of current cells and on the shape of the patch. For rectangular patches with $m \times n$ charge cells, the number of x-directed current cells is $M = n(m-1)$, and that of y-directed current cells $N = m(n-1)$

Each current cell supports one rooftop basis function, to which is associated one test segment joining the centres of the two charge cells belonging to the current cell. The centre and the ends of the segment C_{xj} associated to the j-th x-directed current will be

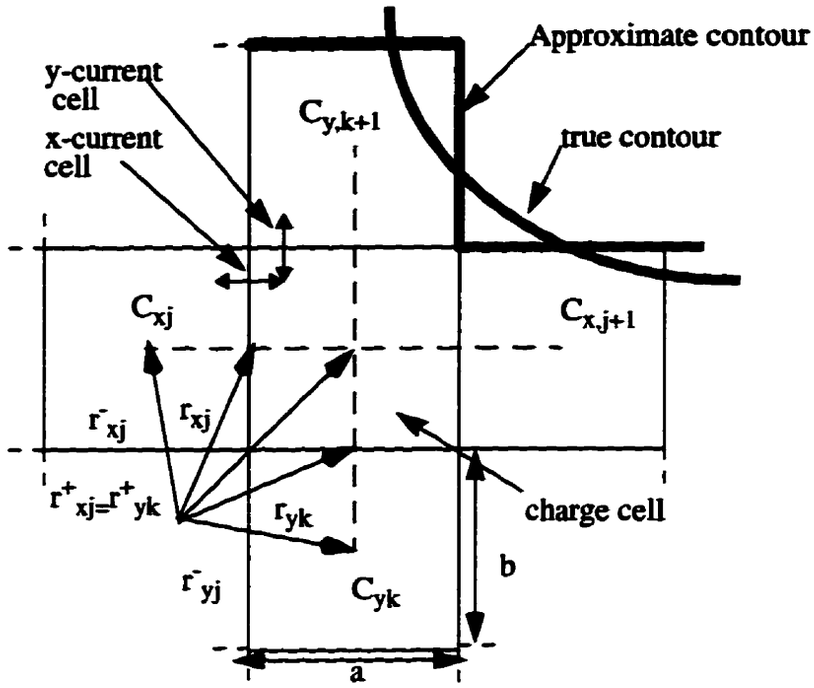

Figure 1.3: Segmentation of the patch in elementary charge and current cell

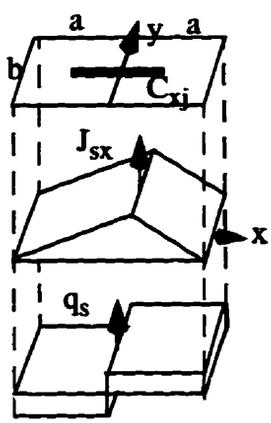

Figure 1.4: x-directed current cell centred at r=0 and its associate surface current density J_{sx} and surface charge density q_s

denoted by the vectors r_{xj}, and r^{+}_{xj}, r^{-}_{xj} respectively.These three vectors are related through

$$\vec{r}^{\pm}_{xj} = \vec{r}_{xj} \pm \vec{e}_x (a/2) \tag{1.25}$$

1.6.2. Basis functions

The Cartesian components of the surface current are expanded over a set of basis functions T_x, T_y:

$$J_{sx} = \frac{1}{b} \sum_{j=1}^{M} I_{xj} T_x (\vec{r} - \vec{r}_{xj}) \tag{1.26}$$

$$J_{sy} = \frac{1}{a} \sum_{j=1}^{N} I_{yj} T_y (\vec{r} - \vec{r}_{yj}) \tag{1.27}$$

where the basis functions are of rooftop type defined as

$$T_x(\vec{r}) = \begin{cases} 1 - |x|/a & |x| < a, |y| < b/2 \\ 0 & elsewhere \end{cases} \tag{1.28}$$

A similar expression is obtained for T_y by interchanging $a \leftrightarrow b, x \leftrightarrow y$ in equation 1.28

The associated surface charge density is obtained from equation 1.27 by using the continuity equation,

$$q_s = \frac{1}{j\omega ab} \left\{ \sum_{j=1}^{M} I_{xj} \left[\Pi\left(\vec{r} - \vec{r}^{+}_{xj}\right) - \Pi\left(\vec{r} - \vec{r}^{-}_{xj}\right) \right] + \sum_{j=1}^{N} I_{yj} \left[\Pi\left(\vec{r} - \vec{r}^{+}_{yj}\right) - \Pi\left(\vec{r} - \vec{r}^{-}_{yj}\right) \right] \right\} \tag{1.29}$$

where $\Pi(\vec{r})$ is a two dimensional unit pulse function defined over a rectangle of dimensions $a \times b$, centred at $\vec{r} = 0$.

The charge density within every elementary cell remains constant, justifying name charge cell. For charge cell of Figure 1.4, with four test segments ending at its centre, the surface charge density is simply given by

$$q_s = \frac{1}{j\omega ab}[I_{x,j+1} - I_{x,j} + I_{y,k+1} - I_{y,k}] \tag{1.30}$$

1.6.3. Discrete Green's function

The notation and computation can be simplified by using discrete Green's function instead of the traditional elementary point sources.

A rooftop distribution produces the vector potential $\overline{\Gamma}_A$, whereas rectangular distribution of unit surface charge creates scalar potential Γ_v. The following dimensionless expressions are introduced the discrete Green's functions:

$$\Gamma_A^{xx}(\vec{r}|\vec{r}_{xj}) = \int_{S_{xj}} \frac{1}{\mu_0 k_0} G_A^{xx}(\vec{r}|\vec{r}') T_x(\vec{r}' - \vec{r}_{xj}) k_0^2 dS' \tag{1.31}$$

$$\Gamma_V(\vec{r}|\vec{r}_{Oj}) = \int_{S_{Oj}} \frac{\varepsilon_0}{k_0} G_V(\vec{r}|\vec{r}') \Pi(\vec{r}' - \vec{r}_{Oj}) k_0^2 dS' \tag{1.32}$$

A similar expression hold for $\Gamma^{yy}{}_A$. In these formulas, $\vec{r}_{xj}(\vec{r}_{Oj})$ denotes the centre and $S_{xj}(S_{Oj})$ the surface of the current (charge) cell.

The discrete Green's functions exhibit the same properties of translational invariance and symmetry as the conventional Green's functions. In general case the surface inte-

grals in equations (1.31), (1.32),must be evaluated numerically. When the observation point $\vec{r}$ belongs to the source cell, some difficulties arise in integration process. To avoid them the Green's function must be separated into singular and regular part. The singular part of the Green's function correspond to the dominant term of their static value be extracted, i.e. $G = G_s + (G - G_s)$ where the static value G_s given by:

$$G_A^{xx}(\vec{r}|\vec{r}') = \frac{\mu_o}{4\pi(\vec{r}-\vec{r}')} \tag{1.33}$$

for the vector potential and

$$G_V(\vec{r}|\vec{r}') = \frac{1}{4\pi\varepsilon_0(\vec{r}-\vec{r}')} \tag{1.34}$$

for the scalar potential.

The singular part of G_s can be analytically integrated over the cell's surface. For example the singular part of equation (1.32) is

$$2\pi(\varepsilon_r + 1)\Gamma_V(0|0) \approx 2k_0 a \ln\tan\left(\frac{\alpha}{2} + \frac{\pi}{4}\right) - 2k_0 b \ln\tan\left(\frac{\alpha}{2}\right) \tag{1.35}$$

with $\alpha = \frac{b}{a}$

When the observer is located many cells away from the sources, the sources can be concentrated at the centre of the cell. The following approximations may then be used:

$$\Gamma_A^{xx}(\vec{r}|\vec{r}_{xj}) \approx \frac{1}{\mu_0 k_0} G_A^{xx}\left(\vec{r}|\vec{r}_{xj}\right) k_0^2 ab \tag{1.36}$$

$$\Gamma_V(\vec{r}|\vec{r}_{Oj}) \approx \frac{\varepsilon_0}{k_0} G_V\left(\vec{r}|\vec{r}_{xj}\right) k_0^2 ab \tag{1.37}$$

1.6.4. Test functions

The last step of the resolution with a moment's method is the selection of the suitable test functions. The best choice is use of unidimensional rectangular pulses. The use of these test functions is equivalent to integrating the boundary condition of equations (1.22) and (1.23) along the segments linking the centres of adjacent cells, and therefore the testing procedure yields equations of the type:

$$\begin{aligned} j\omega \int_{C_{xj}} A_x dx + V\left(\vec{r}_{xj}^{+}\right) - V\left(\vec{r}_{xj}^{-}\right) + Z_s \int_{C_{xj}} J_{sx} dx \\ = \int_{C_{xj}} E_x^e dx = V_{xj}^e \end{aligned} \tag{1.38}$$

where C_{xj} is the x-directed test segment extending from $\vec{r}_{xj}^{-}$ to $\vec{r}_{xj}^{+}$ and V_{xj}^e is the excitation voltage along the segment. A similar relationship is obtained for y-directed test segment. The integration of J_{sx} can be done easily using the expansion given by equations 2.27 and 2.28.

$$\int_{C_{xj}} J_{sx} dx = \frac{a}{4b}\left[2I_{xi} + I_{xi+1} + I_{xi-1}\right] = \frac{a}{b} I_{xi} \tag{1.39}$$

1.6.5. The matrix equations

Introducing the expansions (1.26), (1.27) and (1.29) in equation (1.38) and using the discrete Green's functions defined above, the following matrix equation is obtained:

$$\begin{bmatrix} C^{xx} & C^{xy} \\ C^{yx} & C^{yy} \end{bmatrix} = \begin{bmatrix} I_x \\ I_y \end{bmatrix} = \frac{1}{jZ_0}\begin{pmatrix} V_x^e \\ V_y^e \end{pmatrix} \tag{1.40}$$

The elements in submatrices are given by

$$C_{ij}^{xx} = \frac{1}{k_0^2 ab}\left[-\Gamma_V\left(\vec{r}_{xi}^{\,+} \,\middle|\, \vec{r}_{xj}^{\,-}\right) - \Gamma\left(\vec{r}_{xi}^{\,-} \,\middle|\, \vec{r}_{xj}^{\,+}\right) + \Gamma_V\left(\vec{r}_{xi}^{\,+} \,\middle|\, \vec{r}_{xj}^{\,+}\right) + \Gamma\left(\vec{r}_{xi}^{\,-} \,\middle|\, \vec{r}_{xj}^{\,-}\right)\right]$$
$$-\frac{1}{k_0 b}\int_{C_{xi}} \Gamma_A^{xx}\left(\vec{r} \,\middle|\, \vec{r}^{\,-}_{xj}\right) k_0 dx + j\frac{Z_s a}{Z_0 b}\varsigma_{ij} \tag{1.41}$$

$$i = 1 \ldots M, j = 1 \ldots N$$

$$C_{ij}^{xy} = \frac{1}{k_0^2 ab}\left[-\Gamma_V\left(\vec{r}_{xi}^{\,+} \,\middle|\, \vec{r}_{yj}^{\,-}\right) - \Gamma\left(\vec{r}_{xi}^{\,-} \,\middle|\, \vec{r}_{yj}^{\,+}\right) + \Gamma_V\left(\vec{r}_{xi}^{\,+} \,\middle|\, \vec{r}_{yj}^{\,+}\right) + \Gamma\left(\vec{r}_{xi}^{\,-} \,\middle|\, \vec{r}_{yj}^{\,-}\right)\right] \tag{1.42}$$

$$i = 1 \ldots M, j = 1 \ldots N$$

where ς_{ij} is the Kronecker delta. The expression for C_{ij}^{xy} is obtained by interchanging the couples *(x,y)*, *(a,b)* and *(M,N)*, and $C_{ij}^{yx} = C_{ji}^{xy}$.

Chapter 2

CHARACTERISTIC OF SINGLE LAYER MICROSTRIP SQUARE RING ANTENNAS

2.1.Introduction

Conducting patch antennas are the most commonly used microstrip antennas. The two extreme cases are the printed patch and the printed loop antennas, as shown in Figure 2.1. In spite of their relatively similar geometry, their electrical behaviour is quite different. The printed patch behaves as a one-dimensional resonator, and thus its width **W**, at resonance, is about a half wavelength, $1/2\lambda_{eff}$. On the other hand, the printed loop behaves as a shorted ring, and thus resonates when its circumference is about a multiple of the substrate effective wavelength and each side length **L** becomes about a quarter wavelength, $1/4\lambda_{eff}$. It is therefore half the size of the printed patch antenna. The loop is a relatively narrow band antenna.

The intermediate configuration is a printed ring antenna, which is similar to the patch,except its central conducting portion of width $\mathbf{W_2}$, is removed. This width $\mathbf{W_2}$, provides a new parameter to control its resonance and impedance [4].

Perforated microstrip patches have been used previously to allow dual frequency operations [25]. Their performance, however, has not been investigated adequately. In this chapter, the characteristics and design parameters of a single layer square ring microstrip

antenna are discussed.

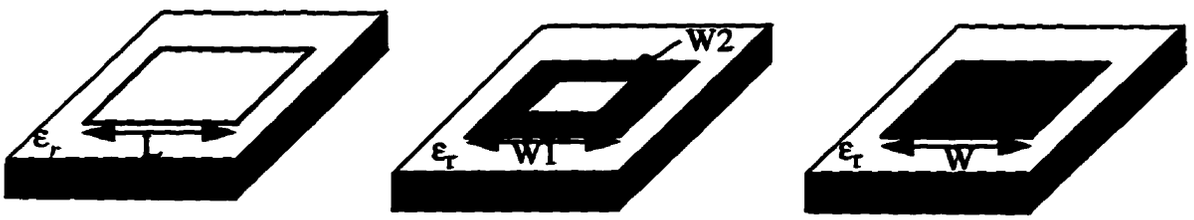

Printed loop
$L \cong \frac{1}{4}\lambda_{eff}$

Printed ring
$\frac{1}{4}\lambda_{eff} < W_1 < \frac{1}{2}\lambda_{eff}$

Microstrip patch
$W \cong \frac{1}{2}\lambda_{eff}$

Figure 2.1: Geometry of printed loop, ring and microstrip patch antennas

2.2. Single Layer Square Ring Resonator

The printed ring antenna is similar to a solid patch except that its central conducting portion W_2 is removed. In order to study the characteristics of a square ring resonator, a solid patch with W_1=30 mm, dielectric substrate relative permittivity ε_r=2.5 and thickness H=0.8,1.59,3.18 mm is considered. The ground plane is assumed infinite and the patch is fed coaxially at X_p=0 mm, Y_p=-13 mm with a probe diameter of d=1.27 mm Figure. 2.2

Extensive computations are carried out to obtain the characteristics of the resonator.

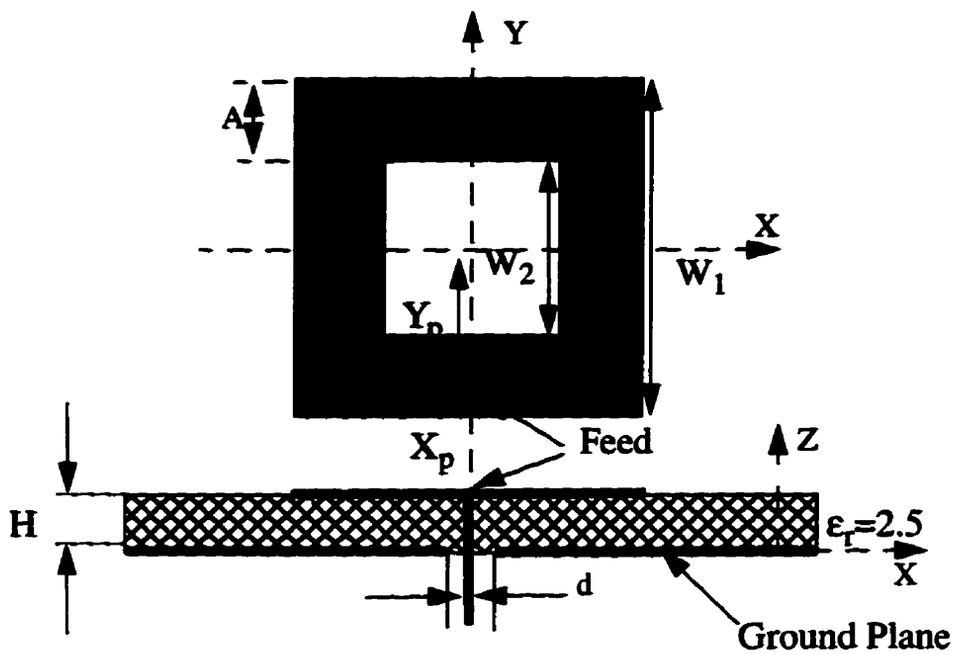

Figure 2.2: Microstrip square ring configuration

2.2.1. Resonance frequency

The resonance frequency of the solid patch for h=1.59 mm and W_1 =30 mm is 3.041 GHz. By increasingly removing the central conducting portion, the resonance frequency decreases, and make it possible to achieve the resonance frequency with a smaller ring size. For instance, when W_2/W_1=0.7 or W_2=21 mm the resonance frequency is 2.147 GHz, which is 70% of the patch resonance frequency. This resonance frequency corresponds to a patch having larger size of 43 mm. The simulation and measurement results for different ring sizes are shown in Figure.2.3. The resonance frequency f_r, is predicted very well for all values of W_2.

The effect of various substrate thicknesses on the resonance frequency is also investigated and the results are shown in Figure.2.4. According to these graphs the resonance frequency of the solid patch increases slightly by decreasing the thickness of substrate. However, this situation is not true for the ring. As the size of perforation is increased the resonance frequency reduces, but the rate of the reduction is faster for the thinner substrate. When the ratio is W_2/W_1=0.7 the resonance frequency is 2.084 GHz for h=0.8 mm, which is 67% of its initial value of 3.111 GHz for a solid patch. Comparing to that of the h=1.59 mm, we see that the resonance frequency has further decreased by 3% .

2.2.2. Input impedance

The calculated and measured values of the input impedance for a coaxial-fed square ring resonator with ε_r=2.5 and h=1.59 mm are shown in Figure.2.5. When W_2 is increased the input impedance at resonance frequency for the ring, i.e. R_{in}, increases. The comparison between its measured and computed Ensemble and Zeland results, which are shown in Figure.2.5, show increasing discrepancies for larger values of W_2 in Ensemble results. However, Zeland shows good agreement with measurement. So, the inaccuracy is in the computed results. In Ensemble, as W_2 increases the convergence of the solution deteriorates and requires finer segmentations to account for rapid current changes.

The values of the input impedance at resonance frequency are also dependent on the substrate thickness.It increases by decreasing *h*, Figure.2.6. For all cases, when the ring width decreases the input impedance increases to the range of thousand ohms, which causes difficulty in impedance matching to a 50Ω transmission line.

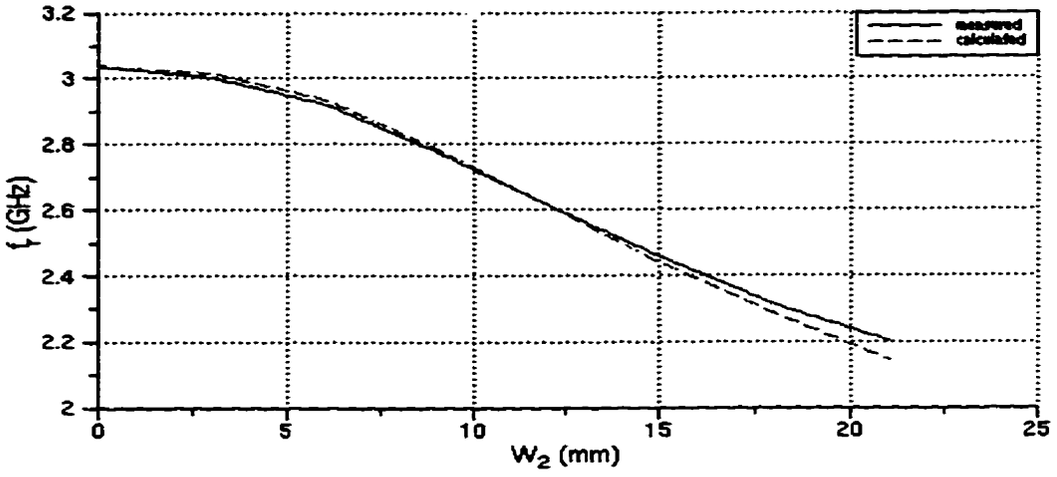

Figure 2.3: Measured and calculated resonance frequency variation with W_2, W_1=30 mm ε_r=2.5, h=1.59 mm

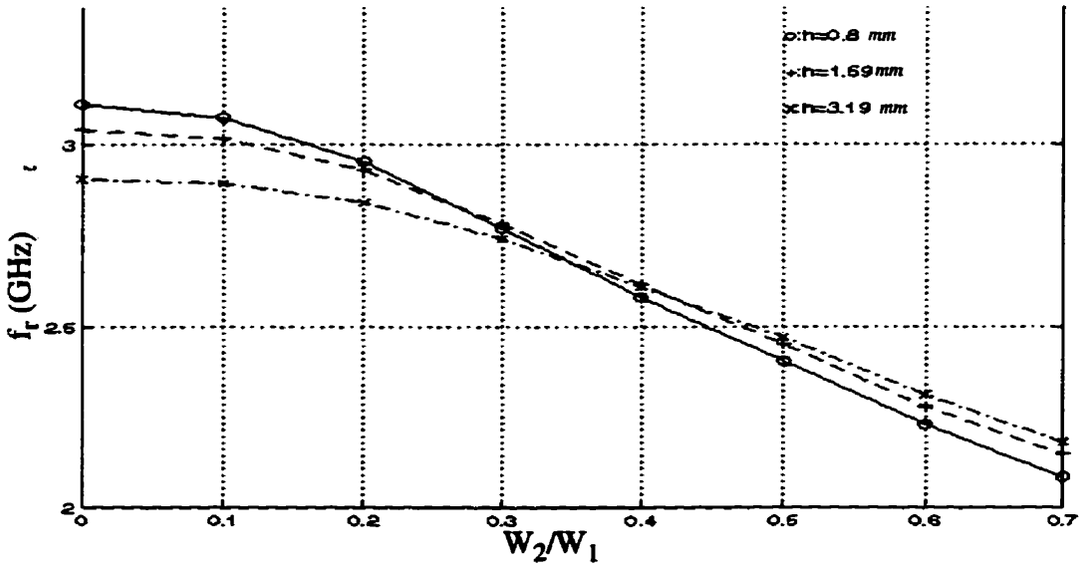

Figure 2.4: Calculated resonance frequency for various substrate thickness W_1=30 mm ε_r=2.5

2.2.3. Total Q-factor and impedance bandwidth

The bandwidth of the antenna in practical designs depends upon how severe the effect of variation of antenna characteristics with frequency has upon the overall system performance. Although in practical situations any of the antenna parameters may limit the antenna bandwidth. In most cases, it is the antenna VSWR which limits the performance. This is particularly true for strongly resonant devices such as a ring. Even then, the tolerance set on the VSWR by the system varies and so to enable a general characterisation of a microstrip ring antennas we make use of the circuit Q-factor, Q_T. This factor may be defined as the ratio of the resonance frequency of the device and the frequency band Δf over which the reflected power is not more than one ninth (VSWR<2) of that absorbed at resonance when matched to the feed line [27].

$$Q_T = \frac{f_r}{\Delta f} \tag{2.1}$$

or for VSWR < S, then the usable bandwidth of the antenna is [27]

$$Bandwidth = \frac{100\,(S-1)}{Q_T\sqrt{S}} \tag{2.2}$$

The ring resonator bandwidths for different values of h are shown in Figure.2.7. The bandwidth for the patch increases by increasing the substrate thickness. But, as the size of its perforation is increased the bandwidth reduces rapidly. The rate of this reduction is increased by decreasing h. For h=3.19 mm the bandwidth reduces from 2.96% for a solid patch to 0.69% for W_2/W_1=0.7 which decreases by about 76%. The reduction for h=1.69 mm is 80.7%, and for h=0.8 mm is 88%. If one compares these numbers with the

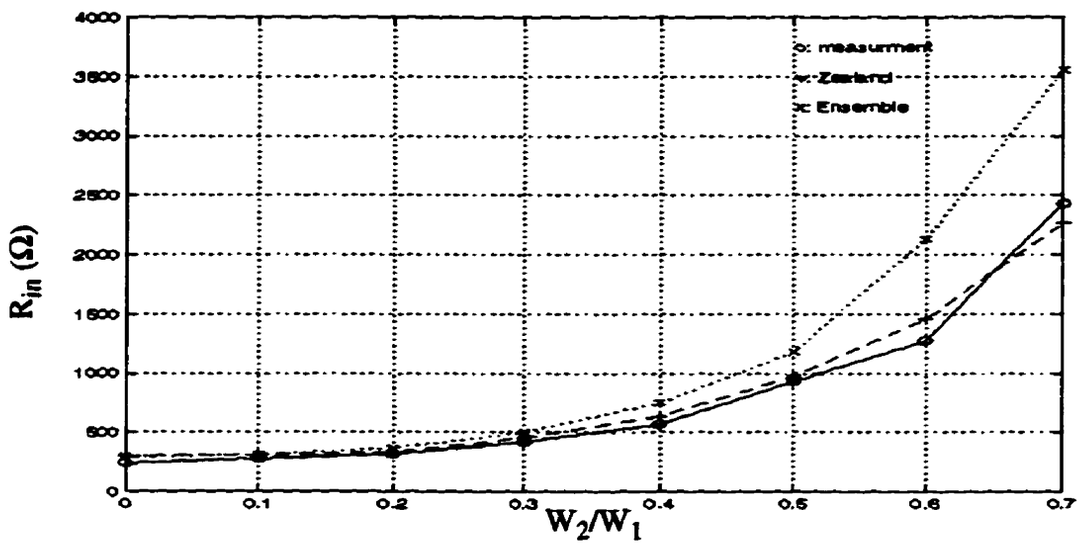

Figure 2.5: Measured and calculated input impedance variation with W_2/W_1, W_1=30 mm, ε_r=2.5, h=1.59 mm

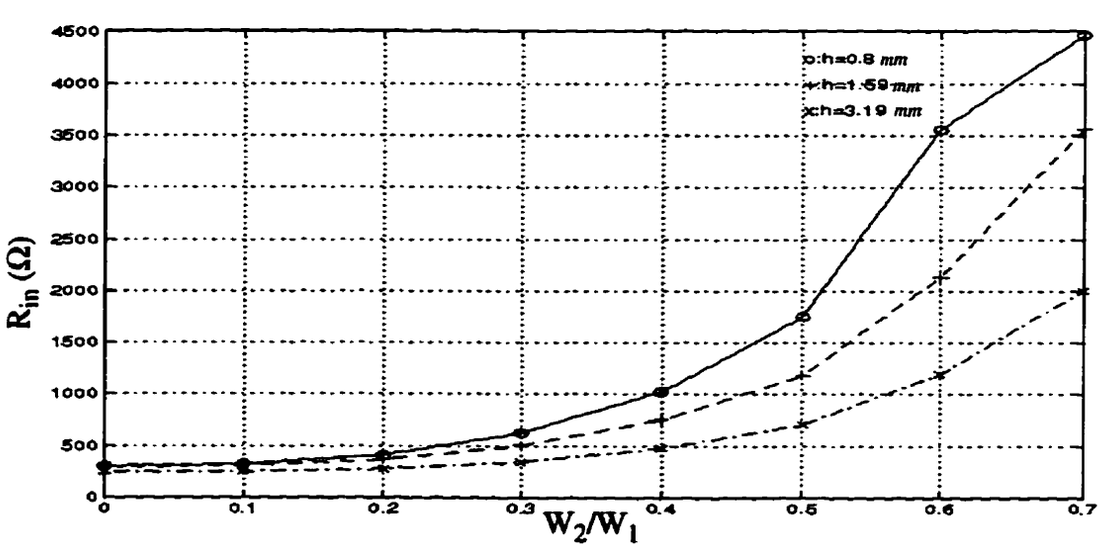

Figure 2.6: Calculated input impedance for various substrate thicknesses, W_1=30 mm, ε_r=2.5

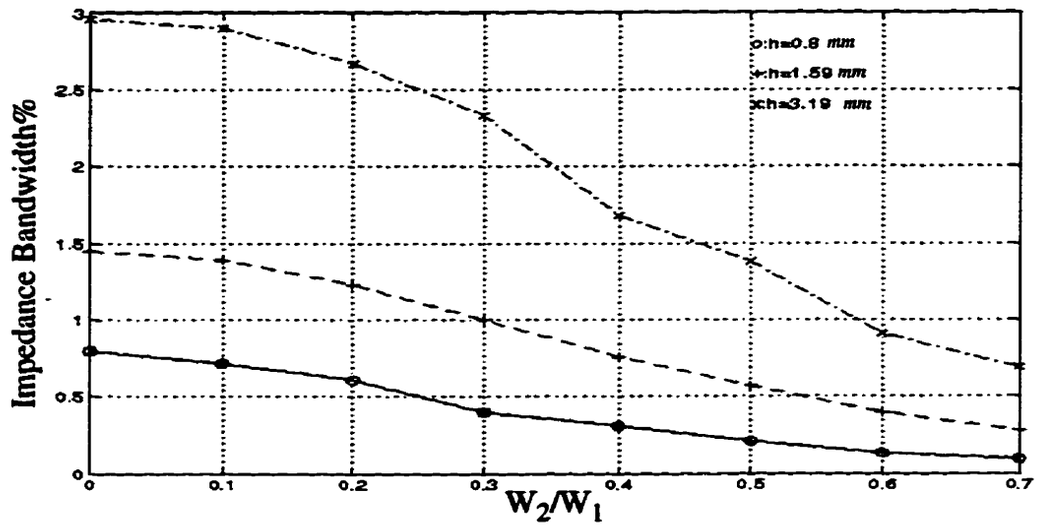

Figure 2.7: Calculated Bandwidth for various substrate thicknesses, W_1=30 mm, ε_r=2.5

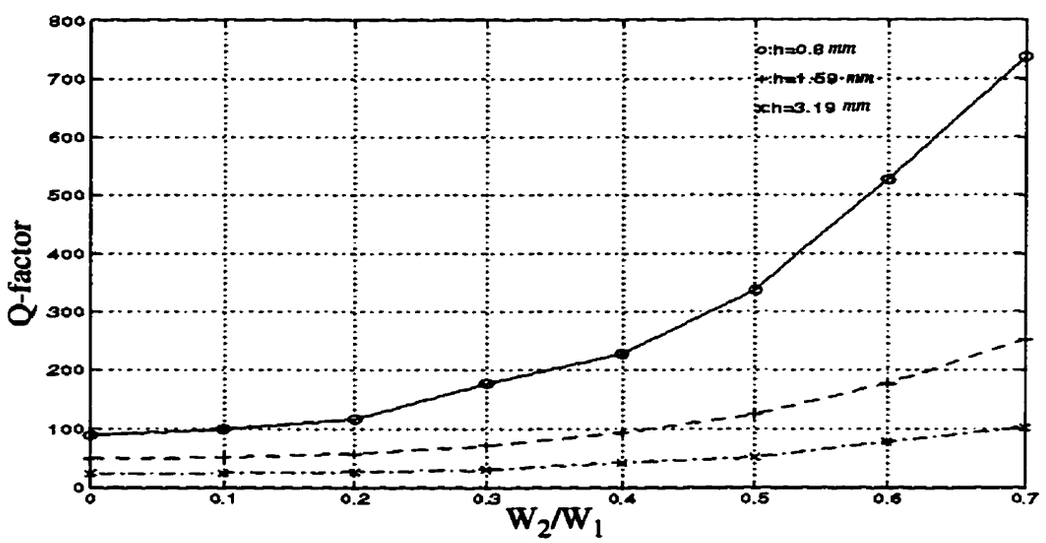

Figure 2.8: Calculated Total Q-factor for various substrate thicknesses, W_1=30 mm, ε_r=2.5

size reductions, which is about 37%, it will be clear that the bandwidth decreases faster. The Q-factor is also shown in Figure.2.8.

2.2.4. Directivity

The directivity of an antenna is defined as the ratio of power density in the main beam to the average power density. The ring directivity as a function of W_2/W_1 for three substrate heights is illustrated in Figure.2.9. The dielectric thickness has almost no effect on the directivity, similar to the solid patch, and the variation due to the ring width, *A*, is not considerable

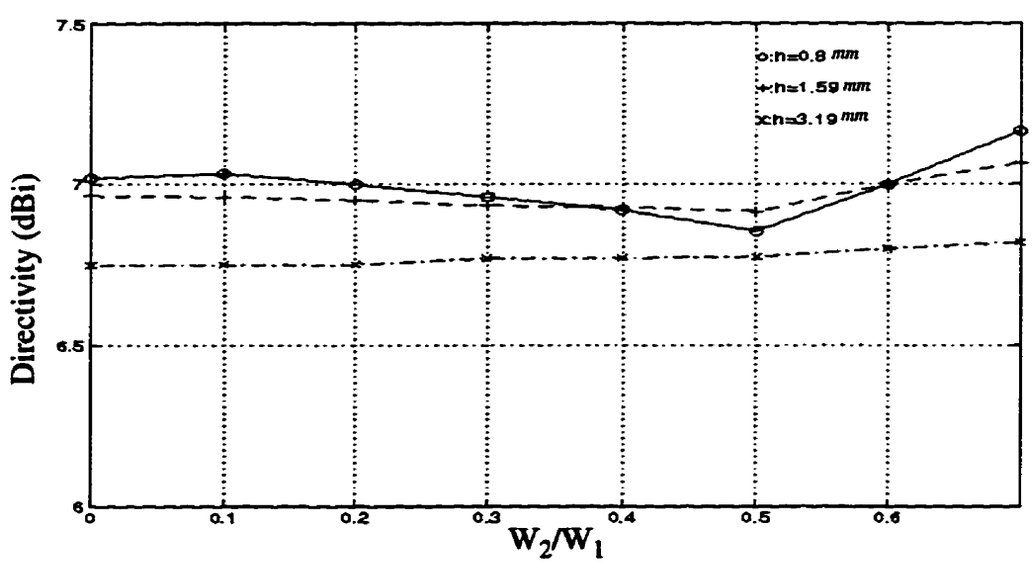

Figure 2.9: Calculated directivities for several substrate thicknesses, W_1=30 mm, ε_r=2.5

This is a very important feature of the square ring antennas. Since by decreasing the antenna size, it is expected that its effective aperture reduces, according to following relationship:

$$D_0 = 4\pi\frac{A_{em}}{\lambda^2} \tag{2.3}$$

the directivity decreases. However Figure 2.9 shows that the antenna effective aperture is independent of the ring outer size, and increases with increasing W_2/W_1.

2.2.5. Radiation patterns

The E and H-plane radiation pattern of the ring with W_2/W_1=0.5 is shown in Figure.2.10. Like a patch, the ring has also a broadbeam radiation pattern. In this figure both E_θ and E_ϕ were calculated in each of the two cuts, ϕ=0, and ϕ=90. It was found that in each case, one of the component has a negligible value,when compared to the other. This indicates a linear polarization with low cross polarization.

The cross-polarization versus W_2/W_1 in both planes is shown in Figures.2.11 and 2.12. By decreasing the thickness of the substrate the variations of cross-polarization increases. These values are not the maximum cross-polarization, which occurred in ϕ=45 plane.

From figures 2.13, and 2.14 the 3 dB beamwidth for H-plane is about 81° and for the E-plane is 110°. These values are not sensitive to the substrate height and the size of perforation, W_2.

2.2.6. Current Components

The real and imaginary components of the currents for W_2/W_1=0.5 and different values of the substrate thickness are shown in Figure 2.15. It is apparent that the perfora-

tion of a conducting patch causes current discontinuities and, therefore, results in rapid variations in its magnitude and direction.

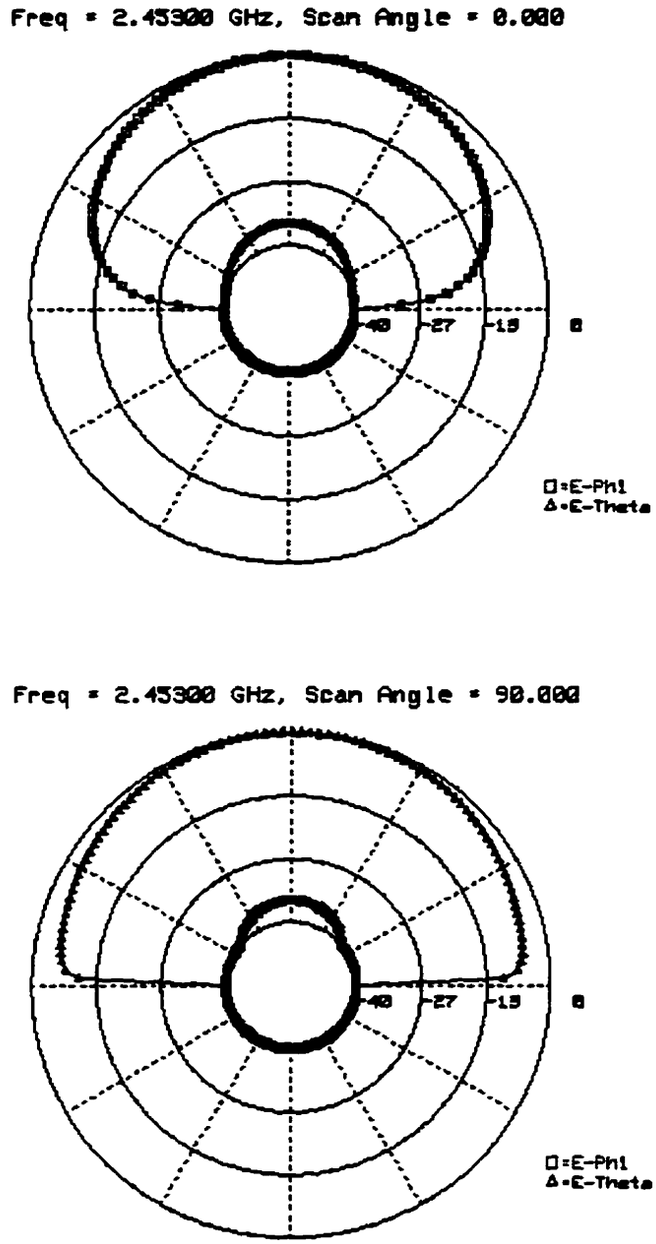

Figure 2.10: H and E-plane radiation patterns for h=1.59 mm and W_2/W_1=0.5, W_1=30 mm, ε_r=2.5

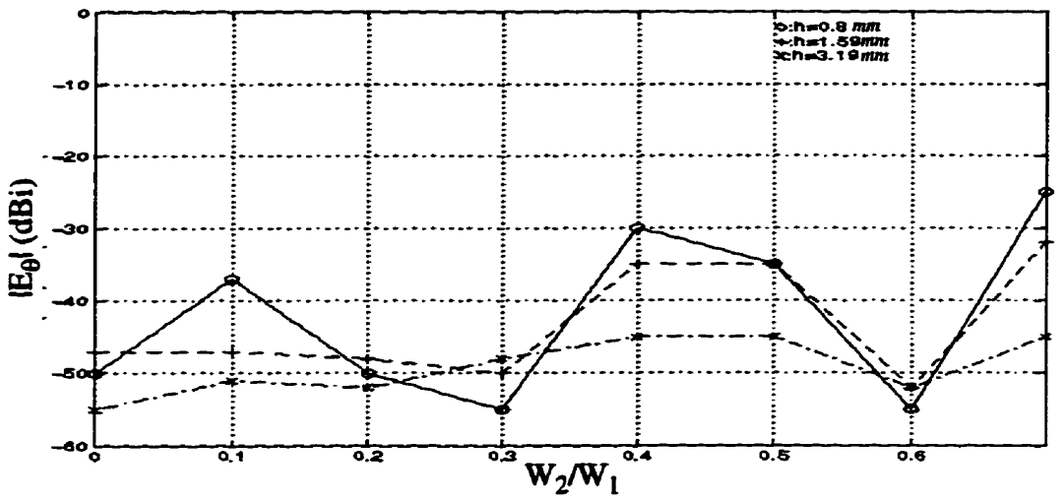

Figure 2.11: Normalized cross-polarization in the E-plane, for ring antenna with W_1=30 mm, ε_r=2.5

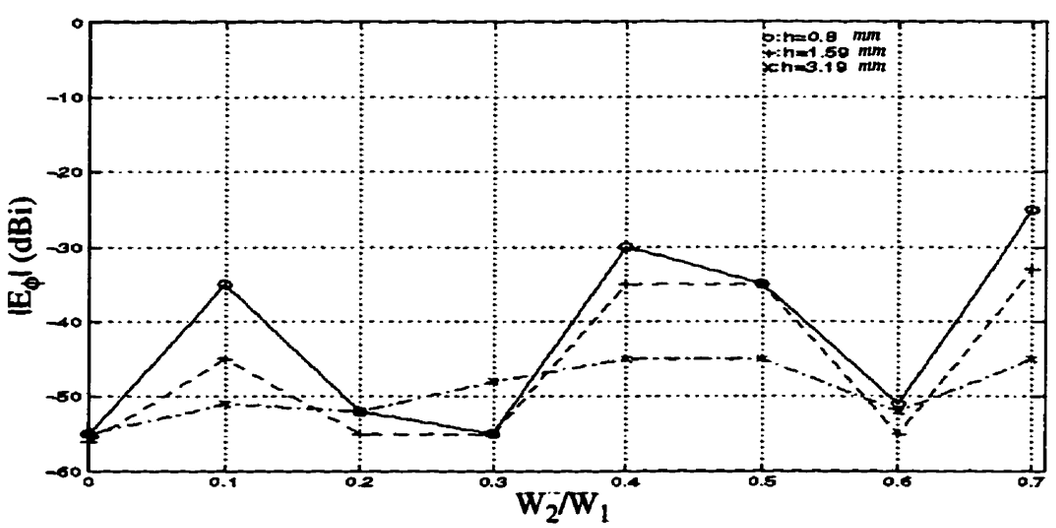

Figure 2.12: Normalized cross-polarization in the H-plane, for ring antenna with W_1=30 mm, ε_r=2.5

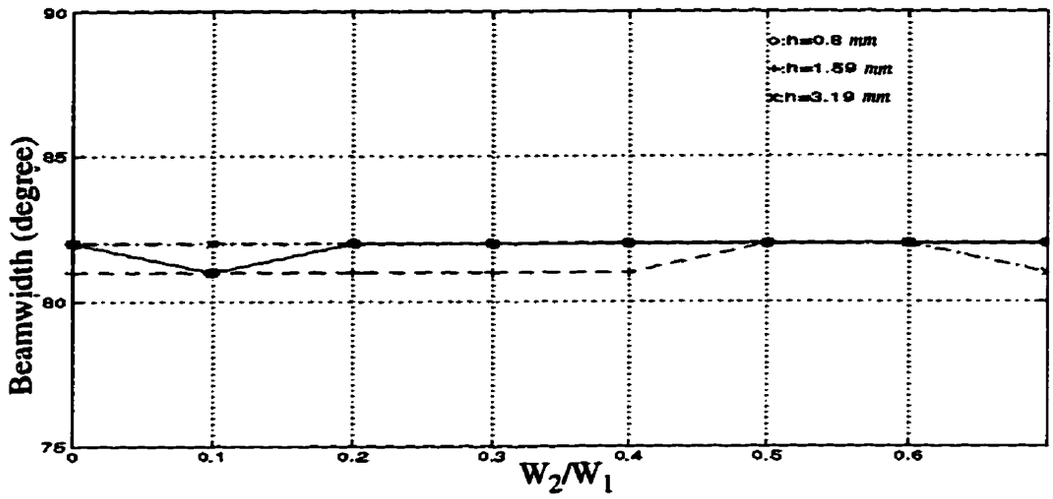

Figure 2.13: H-plane 3 dB beamwidths, for ring antenna with W_1=30 mm, ε_r=2.5

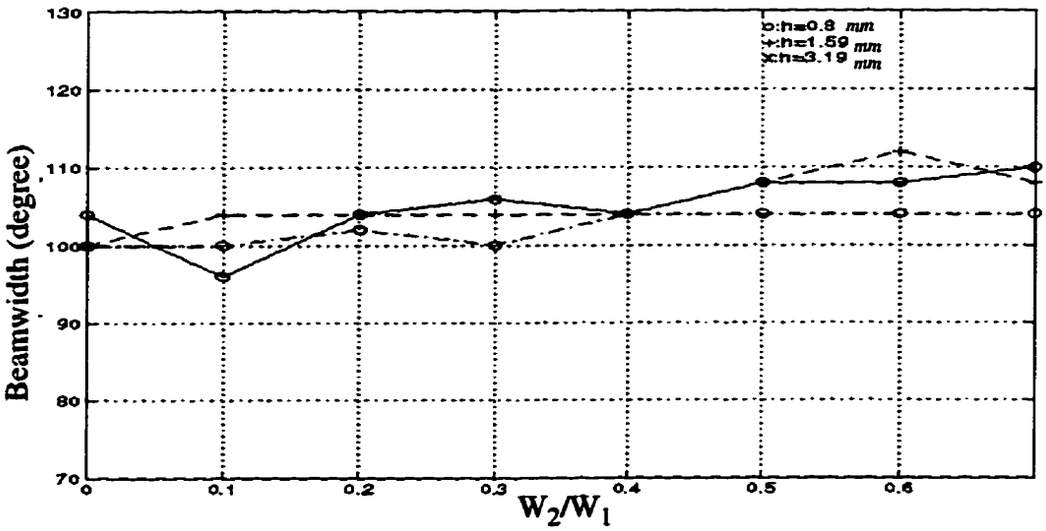

Figure 2.14: E-plane 3 dB beamwidths, for ring antenna with W_1=30 mm, ε_r=2.5

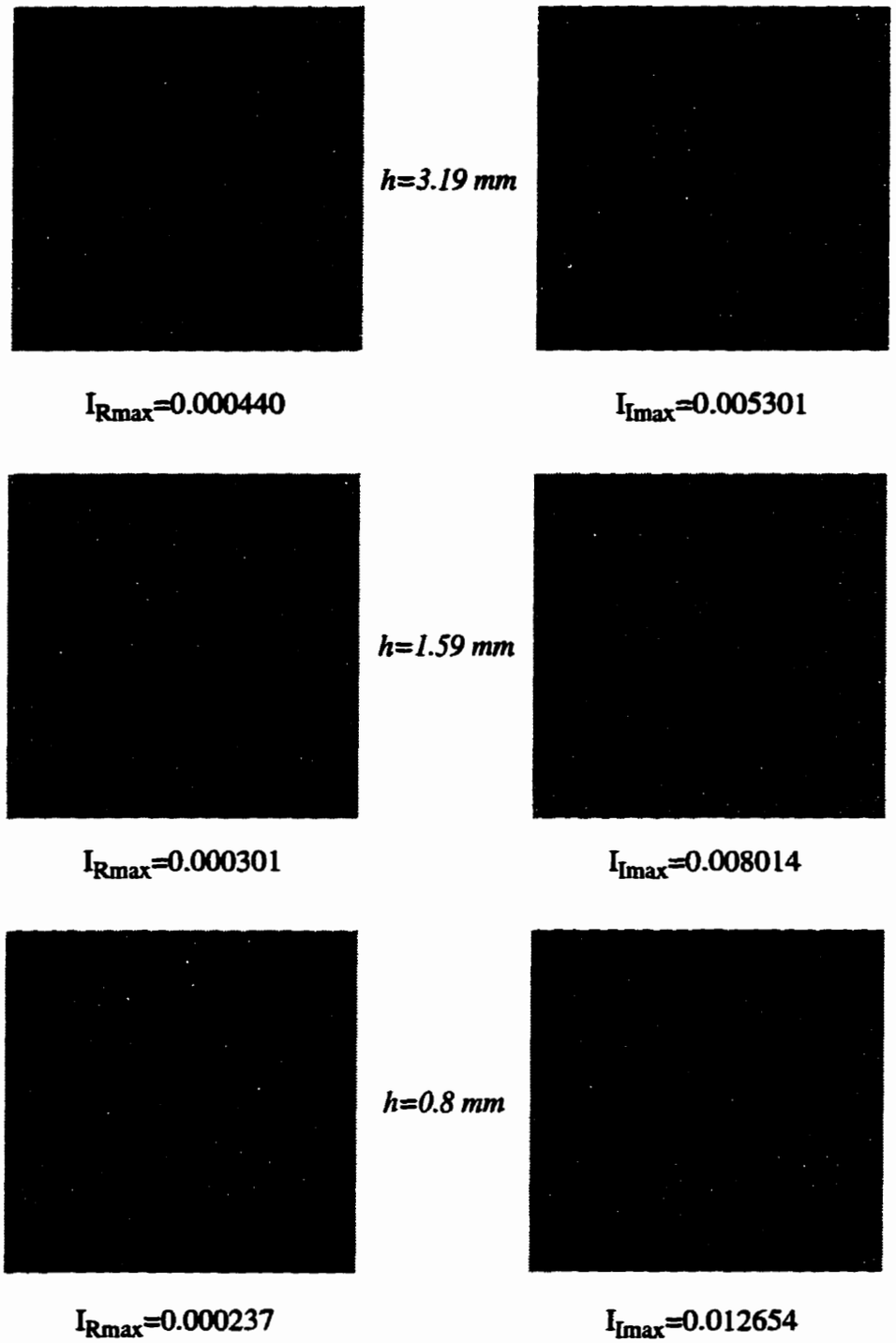

Figure 2.15: Real and imaginary current components for ring antennas of W_2/W_1=0.5, W_1=30 mm, ε_r=2.5

2.2.7. The effect of moving feed probe

In the previous sections the effects of changing the ring width, A, were investigated, and it was found that by increasing the perforation size W_2, the input impedance increases. In a solid patch usually by locating the feed probe in an appropriate place, we are able to match the antenna to a 50Ω transmission line. To investigate the possibility of matching the ring to a 50Ω transmission line, the effect of moving the probe in various directions is investigated.

When the feed probe is located on the symmetry axis of the ring, i.e. on the y-axis in Figure 2.2 its impedance increases toward the outer edge, but the resonance frequency remains constant which is similar to a solid patch. Figures.2.16, and 2.17 show these properties. In the case of a square ring antenna, moving the probe toward the outer edge deteriorates its radiation patterns by increasing the cross-polarization in both E and H-planes. This effect is illustrated in Figures.2.18, and 2.19. So, it seems that the best place to feed the ring, is along its edge, in the x=0 plane, to lower the input impedance at resonance and cross-polarization in both planes.

The effect of moving the probe toward its inner edge is also investigated. It is found that, this displacement has no influence on the resonance frequency, but the input impedance decreases. In this case, no variation in the radiation patterns is observed. The resonance frequency and input impedance for different probe locations and different ring sizes are shown in Figures.2.20, and 2.21. The reduction in the input impedance value helps with impedance matching. Because the probe is located close to the perforated area, it is possible to implement the feeding network or an MMIC circuit in the middle of the

ring. In arrays, this may be an advantage and can be used in reducing the separation distance of its elements to avoid the appearance of grading lobes.

2.3.Miniaturization of Microstrip Antenna with Single Stub

To understand the advantage of using a square ring over other methods, to reduce the size of antenna, method of single stub for size reduction is introduced. It was shown in [32] that, on an impedance locus of the patch in Smith chart, any impedance, which has resistive component, can be matched at any frequency to a 50 Ω transmission line.

For the previous patch, W_1=30 mm, h=1.59 mm ε_r=2.5, the input impedance locus on Smith chart is shown in Figure 2.22. This patch normally resonates at 3.047 GHz with an input impedance of 292Ω . It is possible to match it to a 50Ω line using a quarter-wave transformer. One can also match the impedance at point M, in Figure 2.22, which belongs to a frequency f_l, lower than the resonance frequency of the patch f_r , using 50Ω transmission lines with a stub of length L_1 located a distance L_2 from the patch, Figure2.23. Thus, the patch will resonate at f_l, which is the resonance frequency of a larger patch.

Table 2.1 shows the results of this method for different frequencies. To obtain L_1 and, L_2 , the conventional transmission line model [27] is used. the gain and impedance bandwidth are obtained by Ensemble.

From Table 2.1 the gain is decreasing as the resonance frequency, and as a result the size of the antenna decreases. This, according to equation 2.3, is due to decreasing the

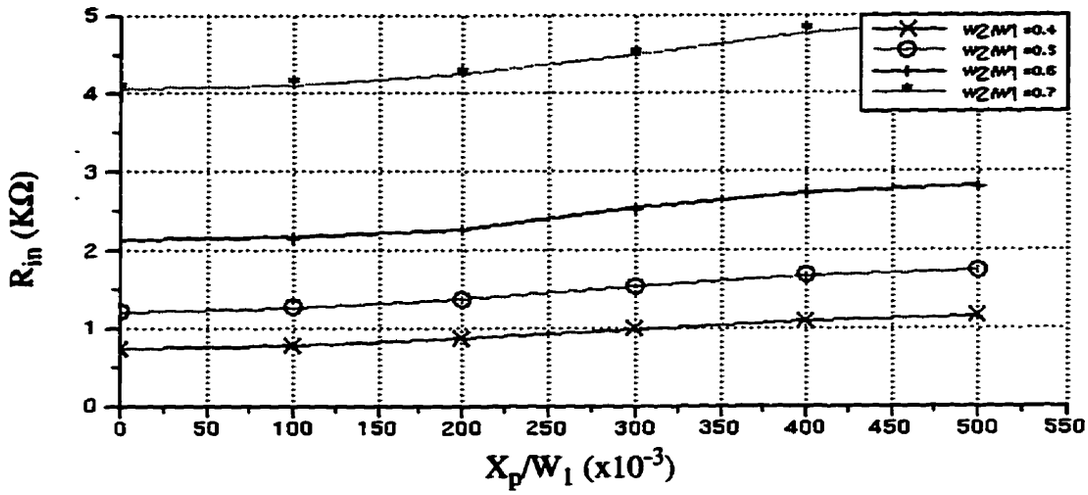

Figure 2.16: Input impedance vs. probe position for different ring sizes, Y_p = -13mm, W_1=30 mm, ε_r=2.5

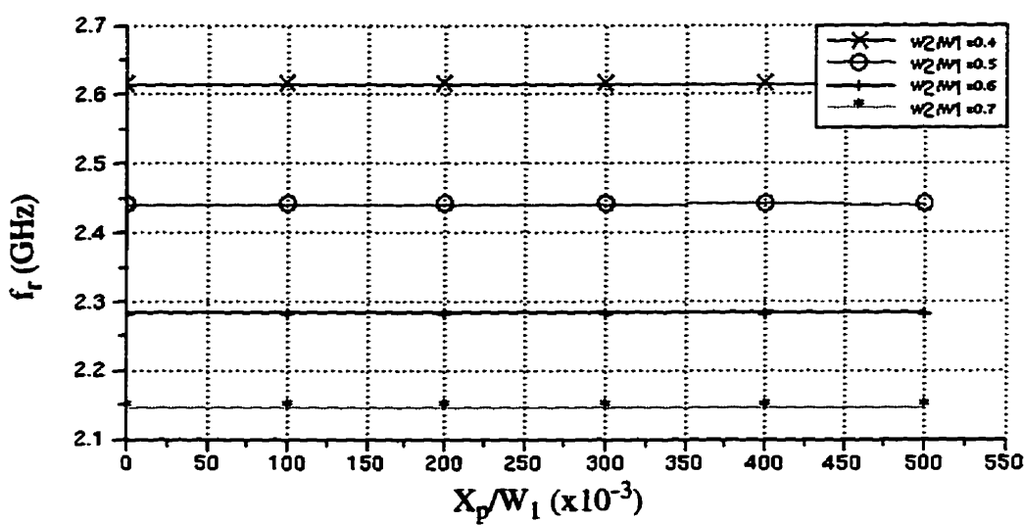

Figure 2.17: Resonance frequency vs. probe position for different ring size, Y_p = -13 mm, W_1=30 mm, ε_r=2.5

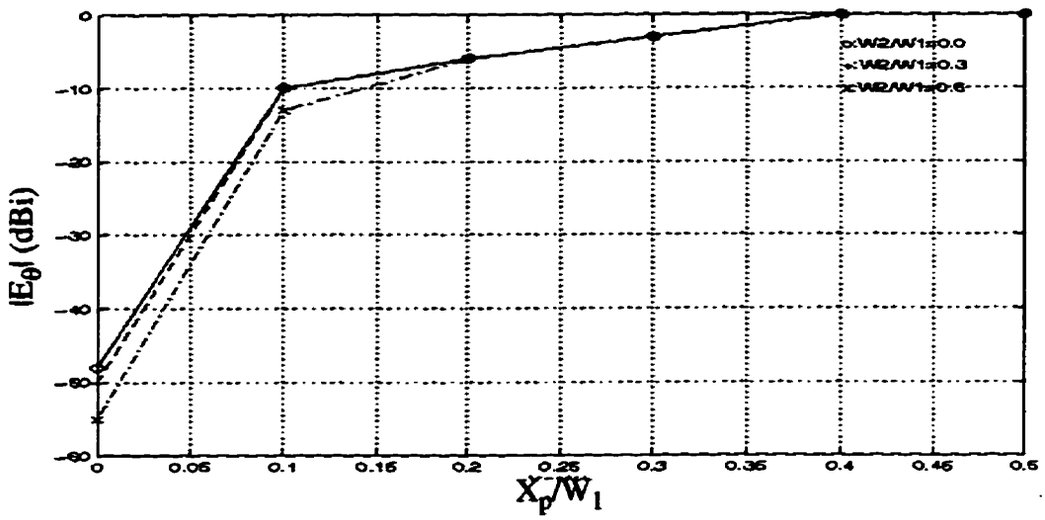

Figure 2.18: Cross-polarization vs. probe position in H-plane, Y_p = -13 mm, W_1=30 mm, ε_r=2.5

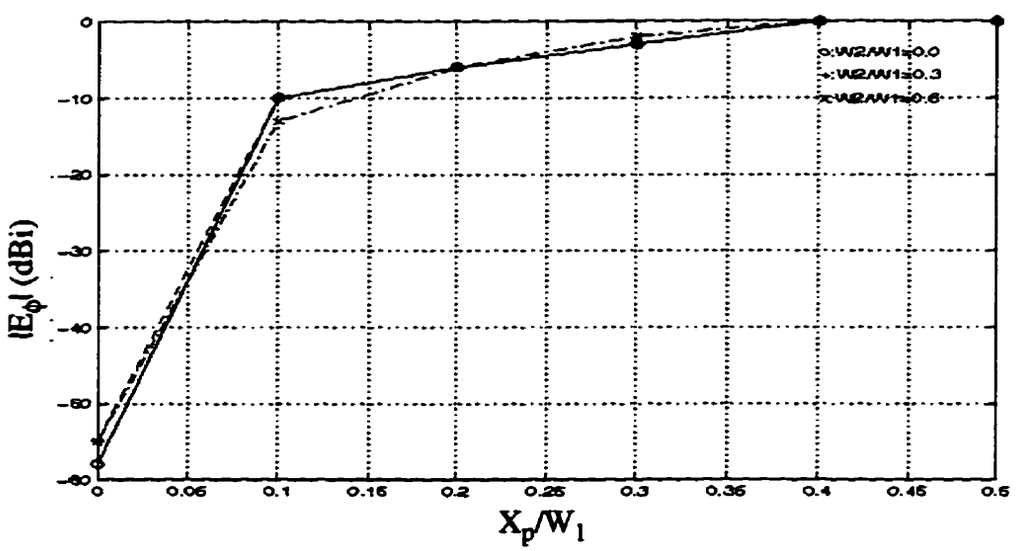

Figure 2.19: Cross-polarization vs. probe position in E-plane, Y_p = -13 mm, W_1=30 mm, ε_r=2.5

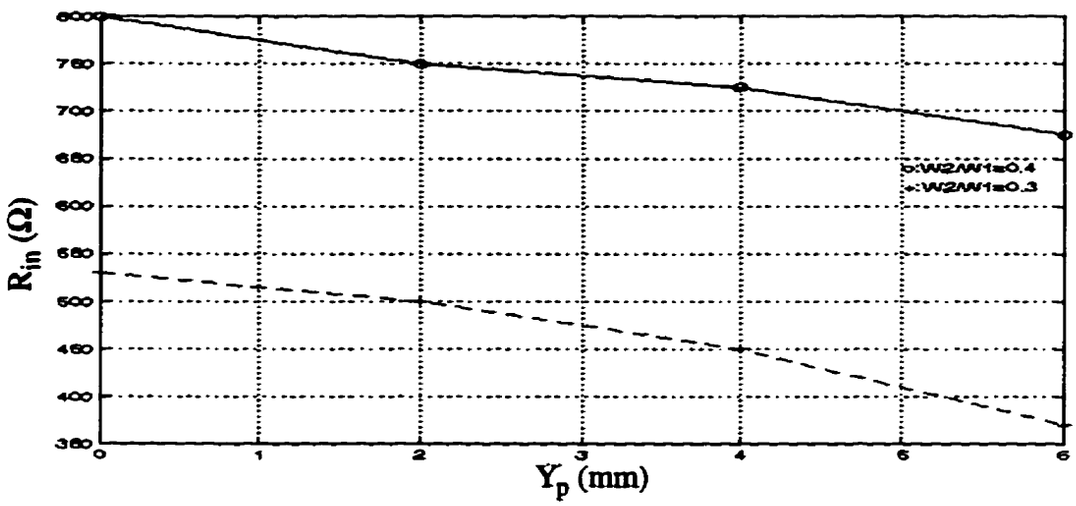

Figure 2.20: Input impedance vs. probe position in y-direction, X_p = 0 mm, W_1=30 mm, ε_r=2.5

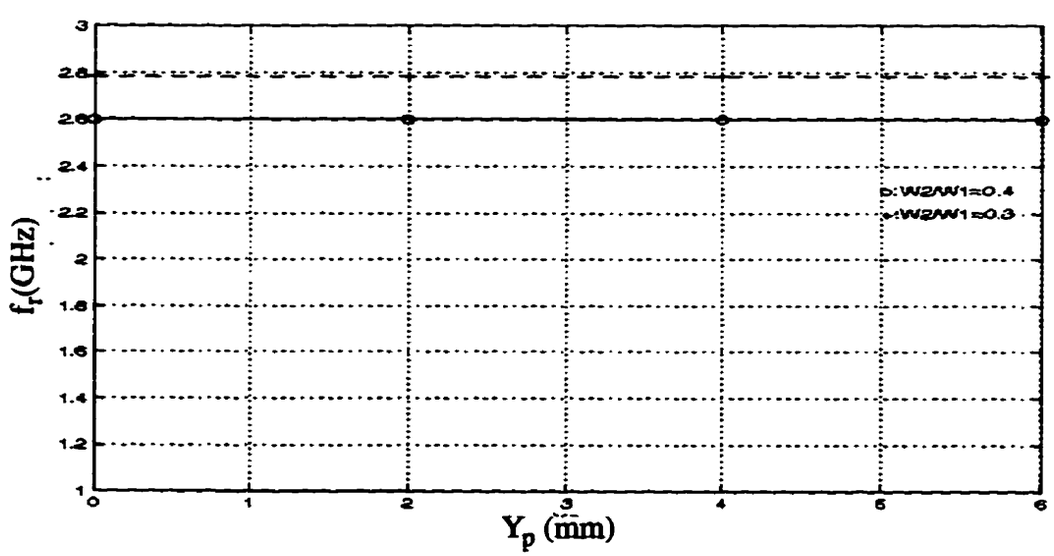

Figure 2.21: Resonance frequency vs. probe position in y-direction, X_p = 0 mm, W_1=30 mm, ε_r=2.5

effective aperture of the antenna which is related to physical area of the patch.

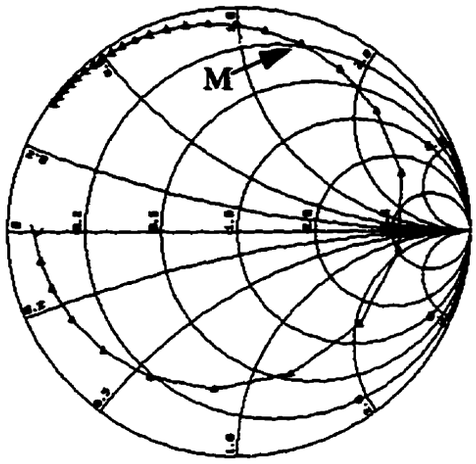

Figure 2.22: Locus of input impedance on Smith chart for a patch with W_1=30 mm, ε_r=2.5 fed by 50Ω transmission line

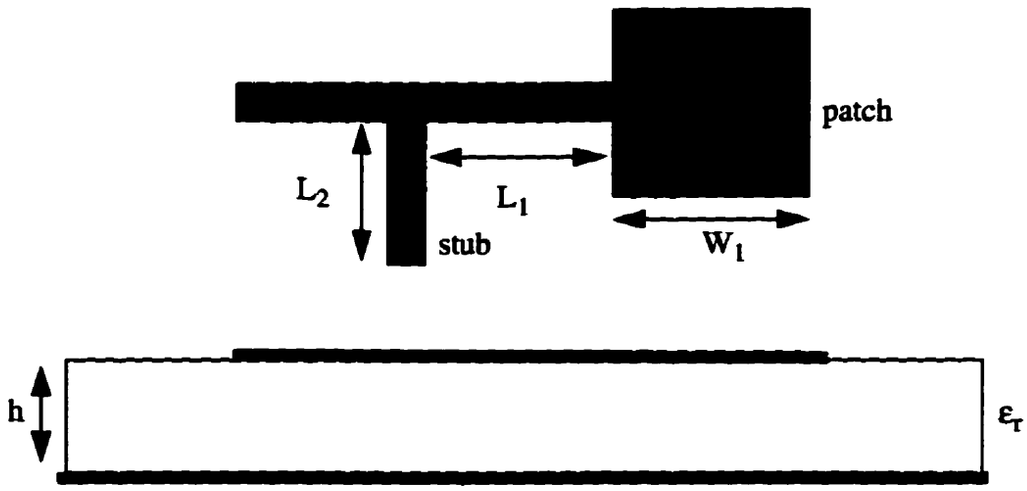

Figure 2.23: Configuration of a patch antenna with single stub

Table 2.1: Results of single stub matching

f_r (GHz)	L_1 (mm)	L_2 (mm)	Directivity (dBi)	BW%
3.045	0	0	7	1.45
2.8	32	14.5	5.41	1.05
2.580	37.7	17.6	4.56	0.4
2.385	41.6	19.6	3.84	0.21
2.228	45.3	21.5	3.43	0.11

2.4.Summary

In this chapter the effects of removing the central conducting portion of a square patch, to form a ring, on its electrical characteristics were studied. Some of the results were compared with experiment and showed good agreements.

It was shown that, by decreasing the ring width, *A*, the input impedance at its resonance increased. However, the resonance frequency decreased and made it possible to reduce the antenna size, as compared to a solid patch.

Unfortunately, the impedance bandwidth also decreased progressively by decreasing the ring width. The bandwidth normally decreases, at the faster rate, than the rate of element size reduction. In practice therefore, one must use other means to increase the element bandwidth.

It was found that, perforation of a patch to form the ring causes rapid changes in

the current directions, making numerical computation more difficult.The ring impedance also increases toward its outer edge, however, the resonance frequency remains constant.

The results of decreasing ring width are summarized in table2.2

Table 2.2: Variation of ring antenna parameters with its width

Width	Resonance Frequeny	Input Impedance	Directivity	3-dB Beamwidth H-plane	3-dB Beamwidth E-plane	BW%
decreased	decreased	increased	constant	82°	$\approx 110^{\circ}$	decreased

Chapter 3

RESONANCE FREQUENCY PREDICTION USING TRANSMISSION LINE MODEL

3.1.Introduction

The radiation from microstrip patch antennas can be calculated from the equivalent magnetic current distributions around the edges of radiating patch. The magnetic current values can be obtained from the edge voltage (with respect to the ground plane) distributions. Thus the problem of microstrip antenna analysis reduces to that of finding the edge voltage distributions, for a given excitation and for a specified mode of the resonance of the patch. If one considers a rectangular microstrip patch operating in the TM_{10} (or any TM_{m0}) mode, voltage distribution at the edges may be obtained by using a transmission line model.

The transmission line equivalent of a TM_{m0} mode microstrip patch may be used to represent the network equivalents of various microstrip antenna configurations, and also for the patches described by the generalized curvilinear coordinate system, where the separation of variable method can be applied to the wave equation. This modelling approach has been used extensively in the analysis and design of microstrip antennas. However its applications are limited because of the following inherent assumption/ approximations in this approach [33].

1) It is very inconvenient to incorporate the effect of feed junction reactances into account. The junction discontinuity causes higher order evanescent modes to be excited in the vicinity of a junction. The resonance frequency and the edge voltage distribution become modified because of these higher order modes.

2) The transmission line model can be constructed only when a single mode is present. The modelling approach is not applicable when two modes are present simultaneously, as in the case of circularly polarized antennas.

3) The transmission line modelling approach is not applicable for the geometries like rectangular ring and cross shaped antennas according to K.C. Gupta [33].

Based on these assumptions, it is inappropriate to use the transmission line model for square ring antennas. However, by deploying new circuit elements to this model, and after some complicated calculations, one can predict the resonance frequency with an acceptable degree of accuracy.

3.2.The Suggested Model

The proposed transmission line model for the square ring antenna is based on the following assumption and simplifications [30]:

1) The mutual coupling is caused by the simultaneous effects of

- interaction through free space radiation;
- interaction through surface waves.

It is assumed that the influence of surface waves can be neglected. The method, thus is limited to antennas having substrates of small electrical thicknesses and low permittivity.

2) It is assumed further that the square ring microstrip antenna can be represented by four narrow slots (Figure. 3.1).

Starting from these assumptions and using improved transmission line model [27] the corresponding network model, which is shown in Figure 3.2 will be derived.

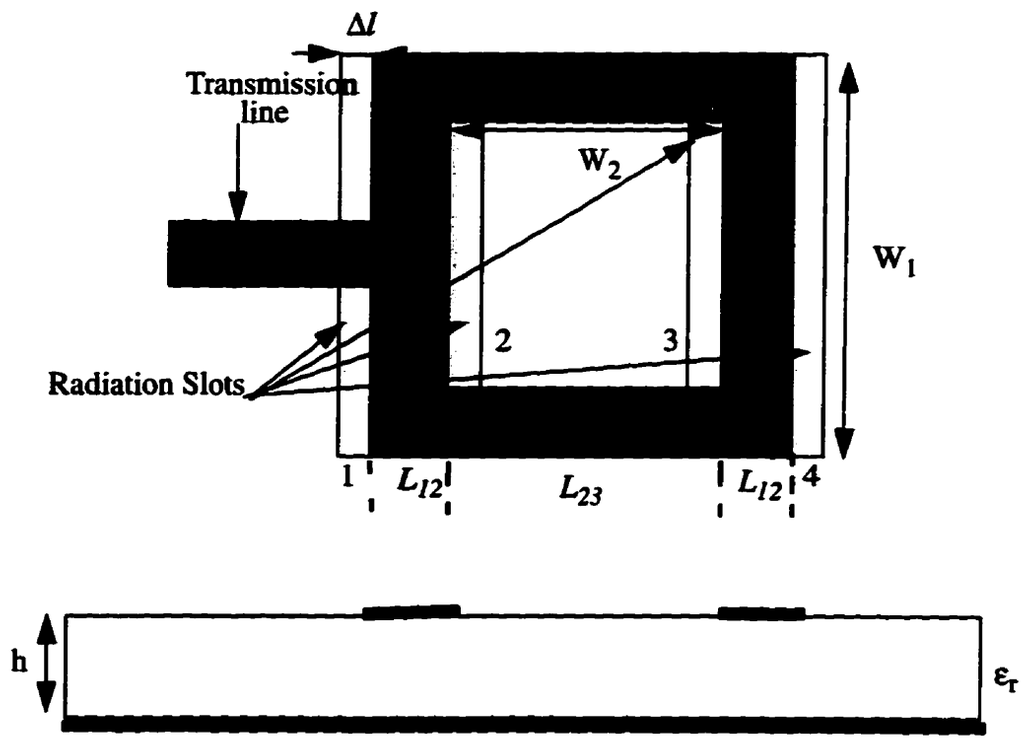

Figure 3.1: Configuration of the square ring with radiation slots

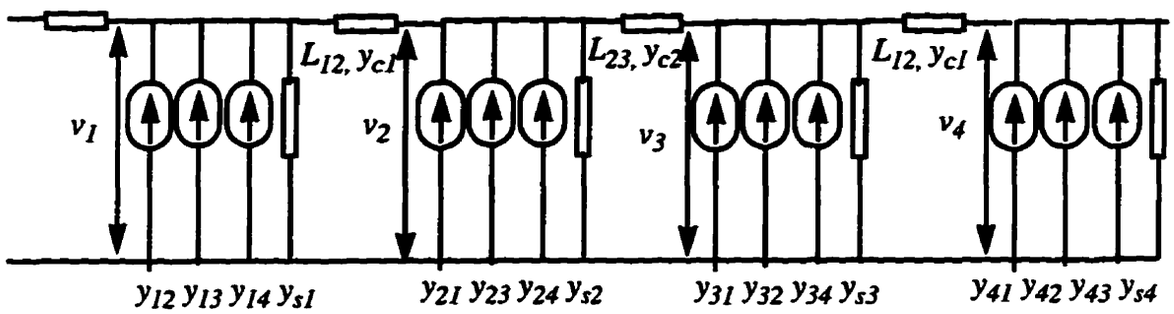

Figure 3.2: Transmission line model for square ring

In this model the square ring is divided into three transmission lines, and each transmission line connects two neighbouring slots. The first one, which connects slots 1 and 2, has the length of L_{12}, characteristic admittances y_{c1}, and propagation constant γ_1. The second one consists of two parallel transmission lines connecting slots 2 and 3. These lines are represented by a length, characteristic admittance, and propagation constant of L_{23}, y_{c2}, and γ_2 , respectively. Due to the symmetry of structure the third transmission line is the same as the first one.

For each slot the self-admittance is denoted by y_{sm}, where m is the slot number. The mutual admittance between the equivalent slots within this structure is given by y_{mn}. The aperture field in the equivalent slots is assumed to be uniform, The slots have the length W_m, width Δl_m and a centre distance $L_e = L_{mn} + \Delta l_m/2 + \Delta l_n/2$.

The next step is to evaluate the parameters of the equivalent network.

3.2.1. Effective dielectric constant

To introduce the effective dielectric constant it is assumed that the centre conductor of the microstrip line with its original dimensions and height above the ground plane is embedded into one dielectric, The effective dielectric constant is defined as the dielectric constant of the uniform dielectric material so that the line has the identical electrical characteristics particularly the propagation constant, as the actual line.

For the low frequencies, the effective dielectric constant is essentially constant. At intermediate frequencies its value begins to monotonically increase and eventually approaches the values of dielectric constant of the substrate. The initial values (at low frequencies) of the effective dielectric constant are referred to as the static values, and they are given by[27]:

$$\varepsilon_{reff} = \frac{\varepsilon_r + 1}{2} + \frac{\varepsilon_r - 1}{2}\left[1 + 12\{\frac{h}{w}\}\right]^{-\frac{1}{2}} \tag{3.1}$$

3.2.2. Effective length

Because of the fringing effects, electrically the patch of the microstrip antenna looks greater than its physical dimensions. A very popular and practical approximated relation for the normalized extension of the length is [27]

$$\frac{\Delta l}{h} = 0.412\frac{(\varepsilon_{reff} + 0.3)}{(\varepsilon_{reff} - 0.258)} \times \frac{\left(\frac{W}{h} + 0.264\right)}{\left(\frac{W}{h} + 0.8\right)} \tag{3.2}$$

Since the length of the ring has been extended by Δl on each side, the effective

length of the ring is now $L_{eff} = L + 2\Delta l$

3.2.3. Expression for the self-susceptance B_s

For the self-susceptance B_s, the correct transmission-line formula is used [27]:

$$B_s = Y_c \tan(\beta \Delta l) \tag{3.3}$$

where Y_c ($\sqrt{\frac{\varepsilon_0 \varepsilon_{reff}}{\mu_0}} \frac{W_{eff}}{h}$) and β ($\omega \sqrt{\mu_0 \varepsilon_0 \varepsilon_{reff}}$) are respectively, the characteristic admittance, and phase constant of the microstrip line.

3.2.4. Expression for the self-conductance G_s

To calculate the self-conductance, one such equivalent slot is considered, as shown in Figure 3.3. [27]The electric field in the slot aperture is assumed to be uniform:

$$E_a = \frac{V_s}{\Delta l}\hat{y} \qquad for \qquad |y| \le \frac{\Delta l}{2}; |x| \le \frac{W_e}{2} \tag{3.4}$$

where Vs=excitation voltage of equivalent slot; Δl = width of the equivalent slot and $\hat{y}$ is the unit vector in y-direction.

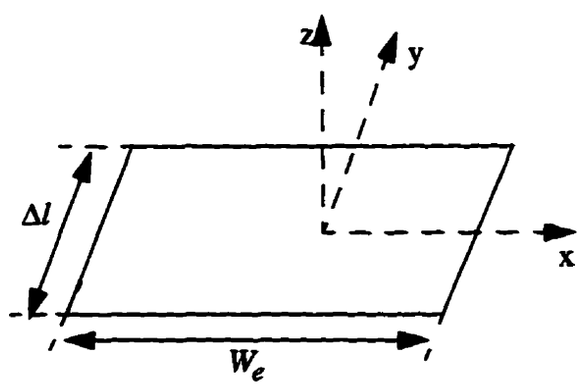

Figure 3.3: Equivalent slot radiator in an infinite, perfectly conducting plane

The spatial Fourier transform of the aperture field is defined as[27]

$$\tilde{E}_a = \int_{-\infty}^{\infty}\int_{-\infty}^{\infty} E_a e^{jk_x x} e^{jk_y y} dxdy \tag{3.5}$$

The aperture field has only a y-component, so that the Fourier transform becomes

$$\tilde{E}_a = \tilde{E}_y \hat{y} \tag{3.6}$$

where [27]

$$\tilde{E}_y = V_s W_e \frac{\sin\left(k_x \frac{W_e}{2}\right)\sin\left(k_y \frac{\Delta l}{2}\right)}{\left(k_x \frac{W_e}{2}\right)\left(k_y \frac{\Delta l}{2}\right)} \tag{3.7}$$

The complex power radiated by this slot may be found by integrating the complex Poynting vector over the aperture surface A:

$$P + jQ = \frac{1}{2}\iint_A \vec{E}_a \times \overrightarrow{H^*}_a \cdot \hat{z} dxdy \tag{3.8}$$

with $\vec{H}_a$ the magnetic field in the slot aperture A, and $\hat{z}$ is unit vector in z-direction

Aperture field can be written in the term of the Fourier-transform [27]

$$P + jQ = \frac{1}{8\pi^2 \eta k}\int_{-\infty}^{\infty}\int_{-\infty}^{\infty} \{\left(k_z^2\right)\left|\tilde{E}_y\right|^2 + \left|k_y \tilde{E}_y\right|^2\} \frac{dk_x dk_y}{k^*_z} \tag{3.9}$$

where

$$k_z \begin{cases} = \left(k^2 - k_x^2 - k_y^2\right)^{1/2} & for \quad k^2 \geq k_x^2 + k_y^2 \\ = -j\left(k_x^2 + k_y^2 - k^2\right)^{1/2} & for \quad k^2 < k_x^2 + k_y^2 \end{cases} \tag{3.10}$$

This complex power can also be written in terms of the network parameters as

$$P + jQ = \frac{1}{2} Y_s^* |V_s|^2 = \frac{1}{2}(G_s - jB_s)|V_s|^2 \tag{3.11}$$

Equating equations (3.9) and (3.11), the expression for G_s follows

$$G_s = \frac{1}{\pi^2 \eta k |V_s|^2} \int_0^k \left\{ \int_0^{\sqrt{k^2 - k_x^2}} \left(k^2 - k_x^2\right) |\tilde{E}_y|^2 \frac{dk_y}{\sqrt{k^2 - k_x^2 - k_y^2}} \right\} dk_x \tag{3.12}$$

using equation (3.7) for $\tilde{E}_y$, G_s is obtained as:

$$G_s = \frac{4}{\pi^2 \eta k_0} \int_0^k \frac{k^2 - k_x^2}{k_x^2} sin^2(k_x W_e/2) \times \left\{ \int_0^{\sqrt{k^2 - k_x^2}} \frac{sin^2(k_y \Delta l/2)}{(k_y \Delta l/2)^2} \frac{dk_y}{\sqrt{k^2 - k_x^2 - k_y^2}} \right\} dk_x \tag{3.13}$$

The inner integral can be written as a double integral of the Bessel function of the first kind and zero order. An expansion of the Bessel function in Maclaurin series and double integration term by term gives [27]:

$$\begin{aligned} &\int_0^{\sqrt{k^2 - k_x^2}} \frac{sin^2(k_y \Delta l/2)}{(k_y \Delta l/2)^2} \frac{dk_y}{\sqrt{k^2 - k_x^2 - k_y^2}} \\ &= \frac{\pi}{2} \{ 1 - \frac{1}{24}\left(\sqrt{k^2 - k_x^2}\Delta l\right)^2 + \frac{1}{960}\left(\sqrt{k^2 - k_x^2}\Delta l\right)^4 \ldots \} \end{aligned} \tag{3.14}$$

The first two terms of this series expression are used to obtain [27]

$$G_s \approx \frac{1}{\pi\eta}\left(\left[wSi(w) + \frac{\sin w}{w} + \cos w - 2\right] \times \left(1 - \frac{s^2}{24}\right) + \frac{s^2}{12}\left(\frac{1}{3} + \frac{\cos w}{w^2} - \frac{\sin w}{w^3}\right)\right) \tag{3.15}$$

where $w = kW_e$ = normalized slot length; $s = k\Delta l$ = normalized slot width; and $Si(x) = \int_0^x \frac{\sin u}{u} du$

The plot of G_s as a function of W_e/λ_0 is shown in Figure.3.4.

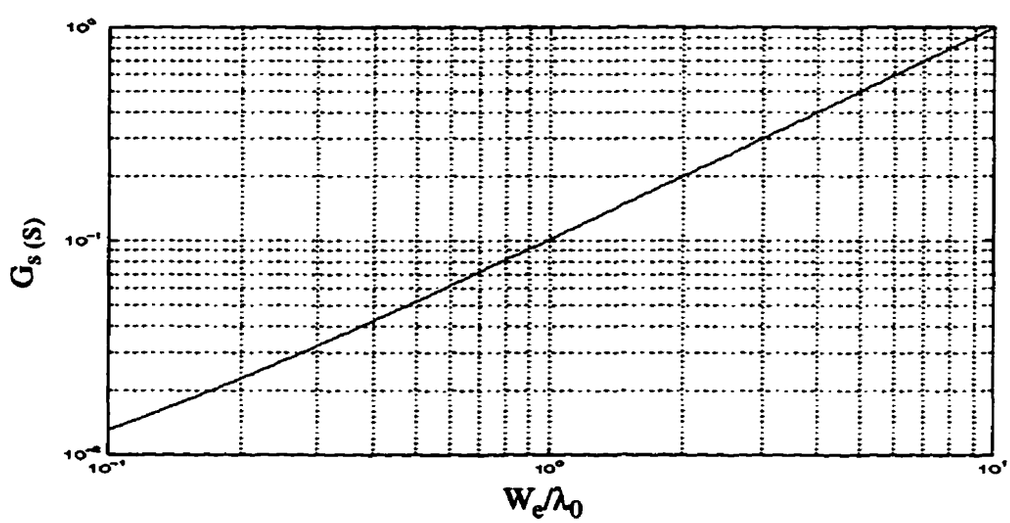

Figure 3.4: Slot self conductance as a function of slot width

3.2.5. Expression for mutual-admittance

Starting from the expression for radiating power [30]:

$$P_{rad} = \int_S \frac{\left(\vec{E} \times \vec{H}^*\right)}{2} \bullet \hat{n} dS \tag{3.16}$$

where the surface S encloses antenna and $\hat{n}$ is unit vector normal to surface S. Applying Gauss' theorem and supposing the antenna is perfectly conducting, the following expression is obtained:

$$P_{rad} = -\frac{1}{2}\int\left(\vec{H}^{*\prime} \bullet \vec{K}_{f,m} + \vec{E} \bullet \vec{K}^{*}_{f,e}\right)dS \tag{3.17}$$

where $K_{f,e}$ and $K_{f,m}$ are the electric and magnetic surface current densities, respectively, and the prime denotes the transposition operator ($\vec{H}$ is 1×3 matrix and $\vec{H}$ is 3×1).

For planar apertures in perfectly conducting plane, one can apply the equivalence or image theorem to replace $K_{f,e}$ and $K_{f,m}$ by $2K_{f,m}$. After identification of the power contributions from each aperture, the mutual admittance becomes [30]

$$Y^{*}_{12} = -\frac{1}{V^{*}_{1}V_{2}}\int_{S_2}\vec{H}_{1}^{\prime *} \bullet \vec{K}_{f,m,2}dS_2 \tag{3.18}$$

where V_1 and V_2 are the equivalent slot voltage (Figure 3.5) and [30]

$$\vec{H}_1 = \int\vec{K}_{f,m,1} \bullet \tilde{H}dS_1 \tag{3.19}$$

where $\tilde{H}$ is a 3×3 matrix containing the field components of the H-field on the place of slot 2 (Figure3.5)caused by an infinitesimal current element on slot 1.

The element of the matrix $\tilde{H}$ are found from the radiation of infinitesimally small magnetic dipole as given in [29]

$$\tilde{H} = \frac{je^{-jk_o r}}{Z_o 2\pi k_0}\left(-\left(j\frac{k_o}{r^2} + \frac{1}{r^3}\right)\cos\theta\hat{r} + \frac{1}{2}\left(\frac{k^2_o}{r} - j\frac{k_o}{r^2} - \frac{1}{r^3}\right)\sin\theta\hat{\theta}\right) \tag{3.20}$$

The most relevant element of $\tilde{H}$ is

$$H_{yy} = \frac{je^{-jk_o r}}{Z_o 2\pi k_0}\left(\left(j\frac{k_o}{r^2}+\frac{1}{r^3}\right)cos^2\theta + \frac{1}{2}\left(\frac{k^2_o}{r} - j\frac{k_o}{r^2} - \frac{1}{r^3}\right)sin^2\theta\right) \tag{3.21}$$

So the four-dimensional integral for mutual impedance is [30]:

$$Y^*_{12} = -\frac{1}{V^*_1 V_2}\iint \overrightarrow{K^{*'}}_{f,m,1}\left(\vec{r}_1\right) \bullet \tilde{H}^*(\vec{r}_2 - \vec{r}_1) \bullet \vec{K}_{f,m,2}(\vec{r}_2)\, dS_2 dS_1 \tag{3.22}$$

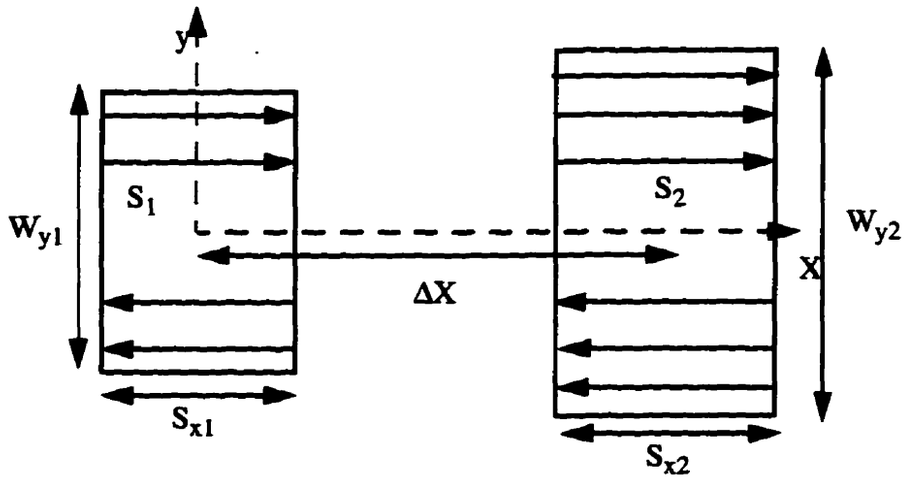

Figure 3.5: Configuration for coupling calculations between rectangular slots

It is possible to rewrite equation (3.22), which is a four-dimensional integral, as a two dimensional one. The procedure is as follows:

Equation 3.22 can be written as

$$Y^*_{12} = -\frac{1}{V^*_1 V_2} \int_{-S_{x1}/2}^{S_{x1}/2} \int_{\Delta x - S_{x2}/2}^{\Delta x + S_{x2}/2} \int_{-W_{y1}/2}^{W_{y1}/2} \int_{-W_{y2}/2}^{W_{y2}/2} \tag{3.23}$$

$$\vec{K}_{f,m,1}(\vec{r}_1) \bullet \tilde{H}^*(\vec{r}_2 - \vec{r}_1) \bullet \vec{K}_{f,m,2}(\vec{r}_2)\, dy_2 dy_1 dx_1 dx_2$$

With substitution [30]

$$\begin{aligned} \vec{u} &= \vec{r}_2 - \vec{r}_1 \\ \vec{v} &= \vec{r}_2 + \vec{r}_1 \end{aligned} \tag{3.24}$$

$$Y^*_{12} = -\frac{1}{4V^*_1 V_2} \int_{-S_{x1}/2 - S_{x2}/2 - \Delta x}^{S_{x1}/2 + S_{x2}/2 - \Delta x} \int_{\Delta x - S_{x1}/2 - S_{x2}/2 + |u_x + \Delta x|}^{\Delta x + S_{x1}/2 + S_{x2}/2 - |u_x + \Delta x|}$$

$$\int_{-W_{y1}/2 - W_{y2}/2}^{W_{y1}/2 + W_{y2}/2} \int_{-W_{y1}/2 - W_{y2}/2 + |u_y|}^{W_{y1}/2 + W_{y2}/2 - |u_y|} \tag{3.25}$$

$$\vec{K}^*_{f,m,1}\left(\frac{\vec{v} - \vec{u}}{2}\right) \bullet \tilde{H}^*(\vec{u}) \bullet \vec{K}_{f,m,2}\left(\frac{\vec{u} + \vec{v}}{2}\right) dv_y du_y dv_x du_x$$

This enables to do the integration with respect to $\vec{v}$ if the current distribution within the rectangular aperture is known and independent from the position of each slot. In this case the field distribution within the equivalent slots is suppose to be

$$\vec{E}_t = -\hat{x} E_o \tag{3.26}$$

Hence the magnetic current is given by [30]:

$$\vec{K}_{f,m} = -2\hat{z} \times \vec{E}_t \tag{3.27}$$

The real and imaginary parts of y_{12} are shown in Figures 3.6 and 3.7.

3.2.6. Admittance matrix

To obtain the resonance frequency of the suggested model, one needs to find the

input impedance of the network. The resonance frequency is the frequency, at which the imaginary part of input impedance is zero.

Due to the symmetry of the network and reciprocity theorem the following simplification can be made:

$$\begin{aligned} y_{12} = y_{21} = y_{34} = y_{43} \\ y_{14} = y_{41} \\ y_{23} = y_{32} \\ y_{13} = y_{24} \end{aligned} \tag{3.28}$$

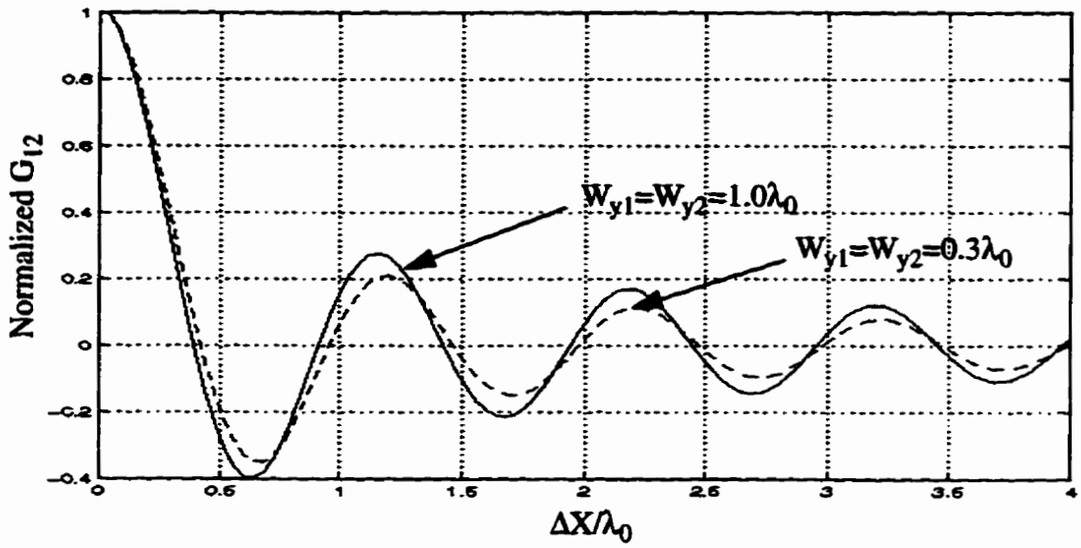

Figure 3.6: Normalized mutual conductance between two slots in E-plane

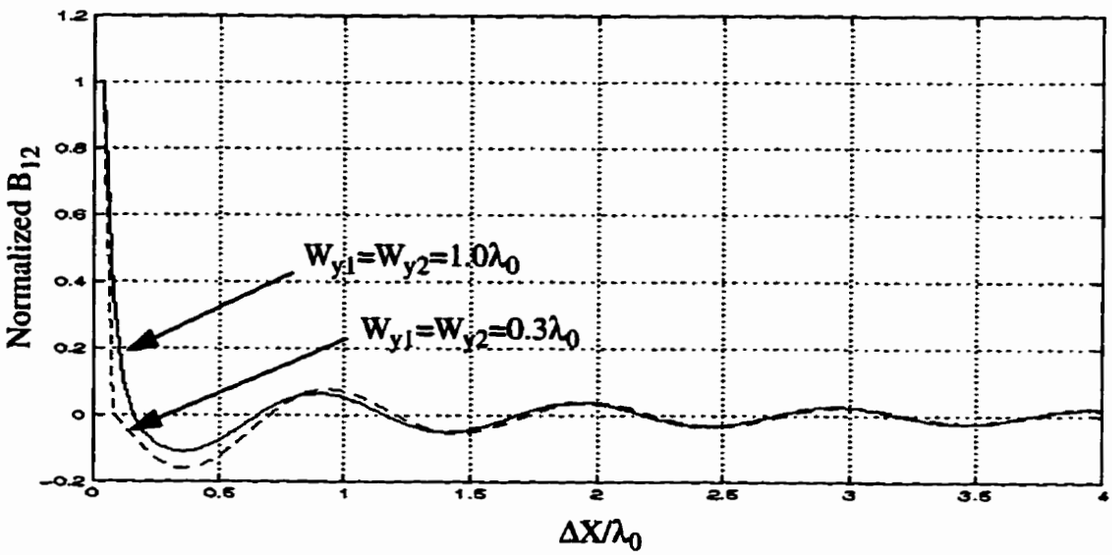

Figure 3.7: Normalized mutual susceptance between two slots in E-plane

and thus the admittance matrix of this one-port model is given by:

$$[Y] = \begin{bmatrix} y_{s1} + y_{c1}\cot\left(j\beta_1 L_{12}\right) & y_{12} - y_{c1}\operatorname{csch}\left(j\beta_1 L_{12}\right) & -y_{13} & -y_{14} \\ y_{12} - y_{c1}\operatorname{csch}\left(j\beta_1 L_{12}\right) & y_{s2} + y_{c1}\cot\left(j\beta_1 L_{12}\right) + y_{c2}\cot\left(j\beta_2 L_{23}\right) & -y_{23} - y_{c2}\operatorname{csch}\left(j\beta_2 L_{23}\right) & -y_{13} \\ -y_{13} & -y_{23} - y_{c2}\operatorname{csch}\left(j\beta_2 L_{23}\right) & y_{s2} + y_{c2}\cot\left(j\beta_2 L_{23}\right) + y_{c1}\cot\left(j\beta_1 L_{12}\right) & y_{12} - y_{c1}\operatorname{csch}\left(j\beta_1 L_{12}\right) \\ -y_{14} & -y_{13} & y_{12} - y_{c1}\operatorname{csch}\left(j\beta_1 L_{12}\right) & y_{s1} + y_{c1}\cot\left(j\beta_1 L_{12}\right) \end{bmatrix} \tag{3.29}$$

3.3.Results

The resonance frequency of a ring antenna for different substrate thicknesses are shown in Figures 3.8, 3.9, and 3.10. The result are compared with simulation results obtained from Ensemble. It seems, the results obtained from the transmission line model approach Ensemble's results by increasing the substrate thickness. Also the transmission line model gives more accurate results for narrow perforations.

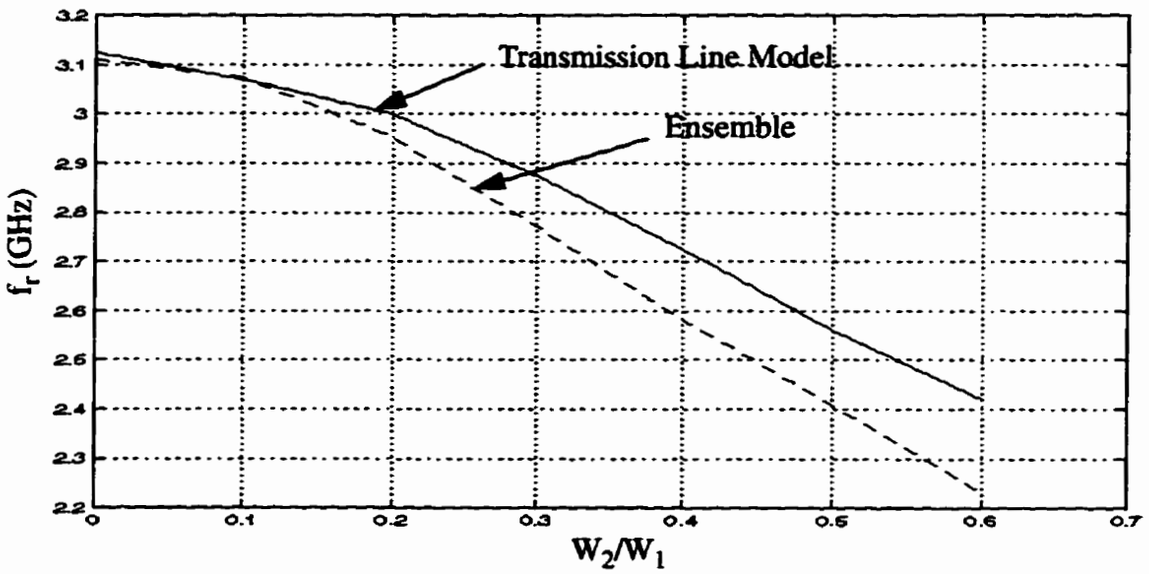

Figure 3.8: Ensemble and transmission line model results for resonance frequency (h=0.8 mm, ε_r=2.5)

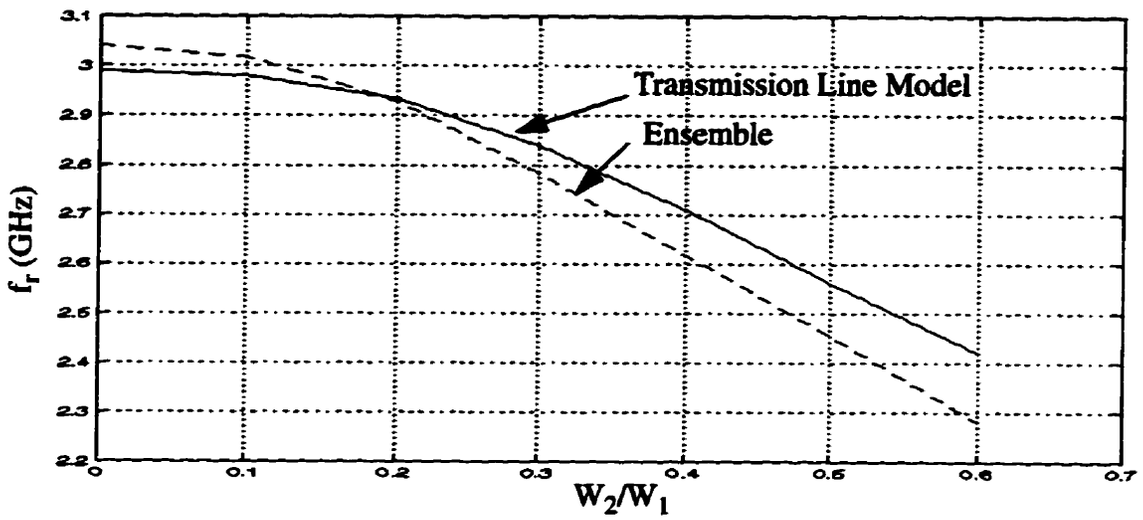

Figure 3.9: Ensemble and transmission line model results for resonance frequency (h=1.59 mm, ε_r=2.5)

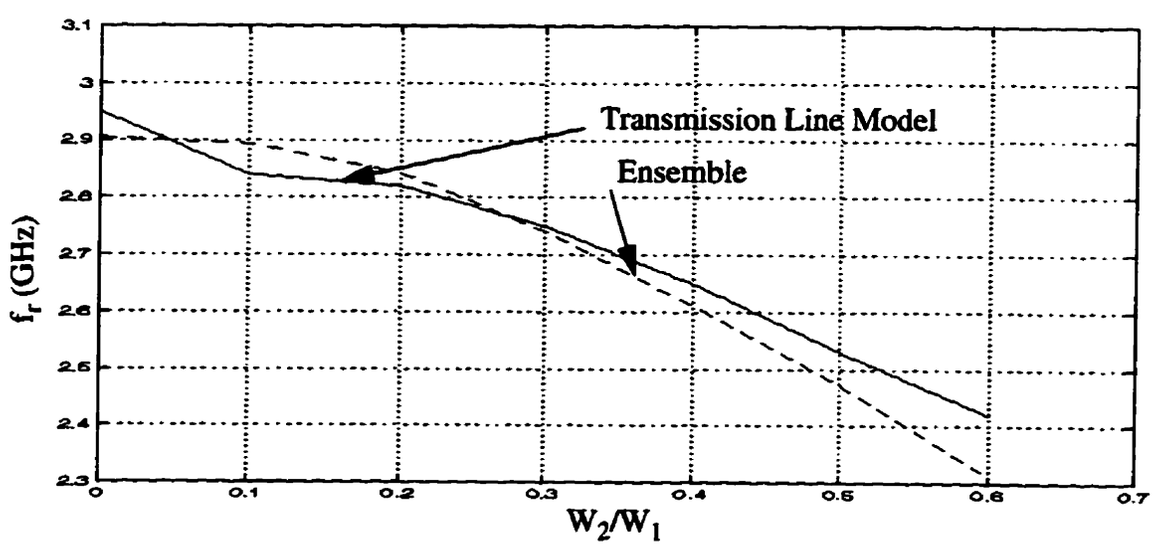

Figure 3.10: Ensemble and transmission line model results for resonance frequency (h=3.18 mm, ε_r=2.5)

3.4.Summary

In this chapter, the transmission line model is used to predict the resonance frequency of microstrip square ring antennas.

This model is based on the improved transmission line model discussed in[27]. To consider the effect of the perforation area two more slots were added. With accurate formulas, the self-admittance and the mutual coupling between each slots were calculated. Using the symmetry of the structure and reciprocity principle, the admittance matrix was derived. The resonance frequency was obtained by equating the imaginary part of the input admittance to zero.

By comparing the results of transmission-line model with those of Ensemble, it was observed that former will give reasonably accurate results for thick substrates and wide ring antennas.The advantage of this model over Ensemble is that, it is easier to use and faster than Ensemble if it is desired to know only the resonance frequency.

Chapter 4

STACKED RING REESONATORS

FOR BANDWIDTH ENHANCMENT

4.1.Introduction

It was observed in chapter 2 that the input impedance of a microstrip square ring, at the resonance frequency, increases rapidly as its width decreases. Thus, it becomes impractical to match the ring to a 50Ω transmission line, using a stub or quarter-wave line. Also it becomes very narrow band. These disadvantages are serious, and prevent its use in many practical applications. Thus, efforts have been made in this study to overcome these limitations.

Increased bandwidth and matched impedance can be obtained in a variety of ways by using parasitically coupled elements to produce a double-tuned resonance configuration. A convenient approach uses a stacked resonators. Two resonators which are stacked must have resonance frequencies near each other. The bandwidth of the stacked antenna is dependent on the heights and dielectric constant of the two substrates. Thus, by tuning these parameters it is possible to achieve desirable bandwidth and also to match the antenna to any given impedances.

In this chapter the effects of stacking a patch on a ring, or two rings on the bandwidth, radiation patterns, gain and resonance frequency are investigated. Different sub-

strate heights and permittivities are considered and studied.

4.2.Theory

A typical two stacked resonator configuration is shown in Figure 4.1. The antenna can be regarded as consisting of two coupled cavities and its performance can be explained qualitatively by considering the fringing field of the two cavities. This fringing field for each cavity is different even when resonator shapes and size are identical, so that each resonator in the stacked antenna will resonate at different frequencies, resulting in a bandwidth enhanced antenna.

Because this structure is field-coupled and involves both electric and magnetic fields, it results in a near ellipsoidal surface over which a perfect match can be found [28]. The surface is illustrated in Figure 4.1. For a given spacing between the two resonators, the upper one intersects the ellipsoid such that the locus of positions for a perfect match is an ellipse centred over the lower resonator. As this spacing is increased, the ellipse is reduced in size until it is a single point. For spacing larger than this value [$H_{D(max)}$], the coupling is too weak to match the structure.

In order to understand the role of electromagnetic coupling in matching the structure and enhancing its bandwidth, an equivalent circuit has been used successfully to model the input impedance of the stacked antenna. This circuit, depicted in Figure 4.2, consists of two coupled parallel resonant circuits, standing for two patches, or rings, and a series inductor to model the feed inductance that is usually observed in a probe-fed reso-

nator. Each resonant circuit has its own resonance frequencies and bandwidth. If these two resonance frequencies are close enough to each other, the total circuit seems to have a bandwidth equal for the sum of the two individual ones.

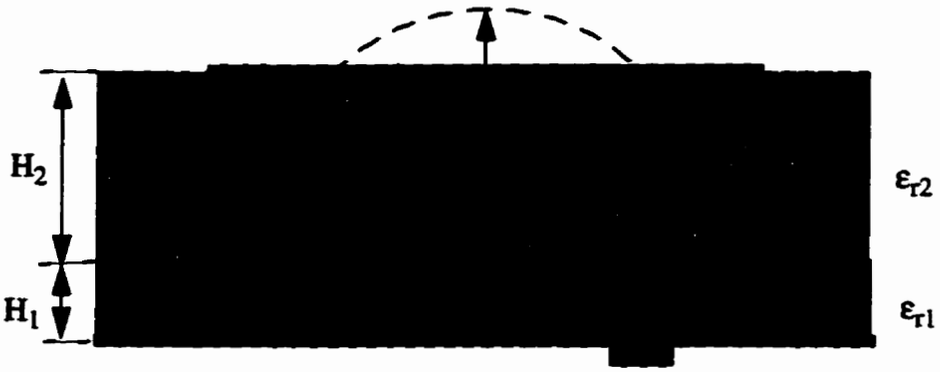

Figure 4.1: Stacked dual-resonator configuration

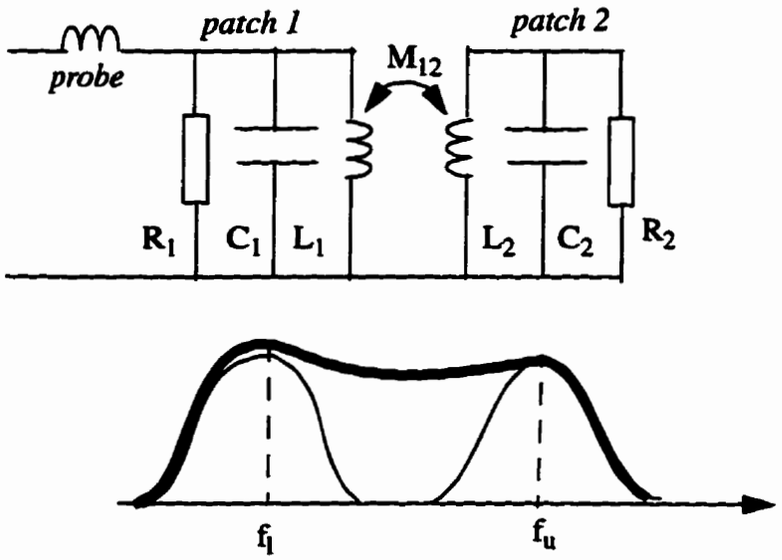

Figure 4.2: Equivalent circuit to model input impedance of Figure 4.1

4.3.Stacked Ring-Patch

First we consider stacking a patch over a ring [34]. A design was completed with ε_{r1} =2.5, H_1 =1.5 mm, W_1 =30 mm, W_2 =15 mm, ε_{r2} = 1.05 (foam) H_2=5 mm, W_3=47 mm, d=1.27 mm, X_p=0 mm and Y_p= -13 mm (X_p, Y_p are shown in Figure 2.2) and simulated (Figure 4.3).

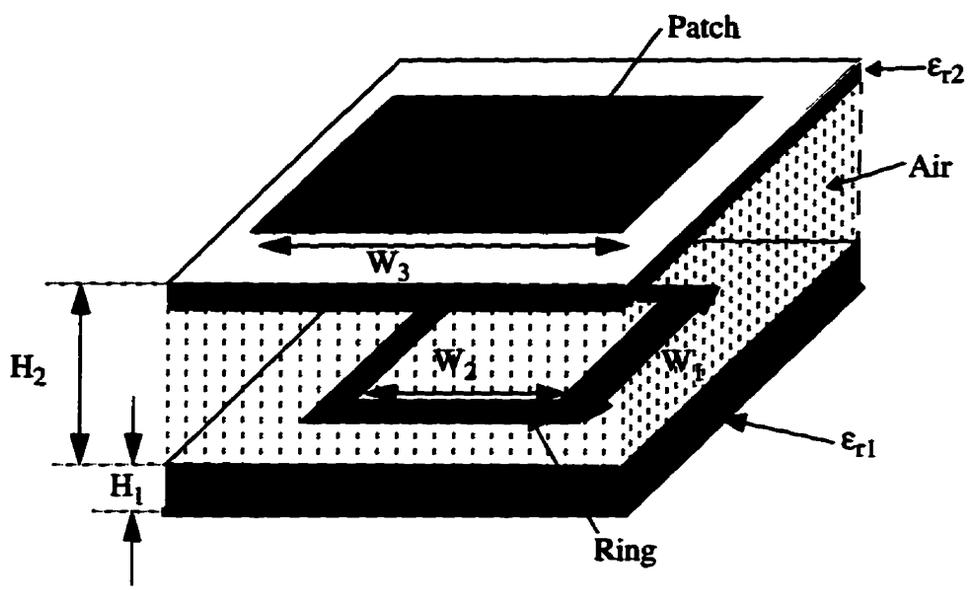

Figure 4.3: Configuration of a stacked ring-patch antenna

One sample was fabricated and tested by "Wiltron 37269A" network analyser and its midband radiation pattern measured in the "Anechoic Chamber". They are shown in Figure 4.4 to Figure 4.10.

Excellent agreement between the theory and experiment is observed for a coaxially fed antenna. In numerical computation, the cell size for the top layer is $0.01\lambda_0$, and for the bottom layer $0.034\lambda_0$, where λ_0 is the wavelength at midband frequency of 2.5 GHz.

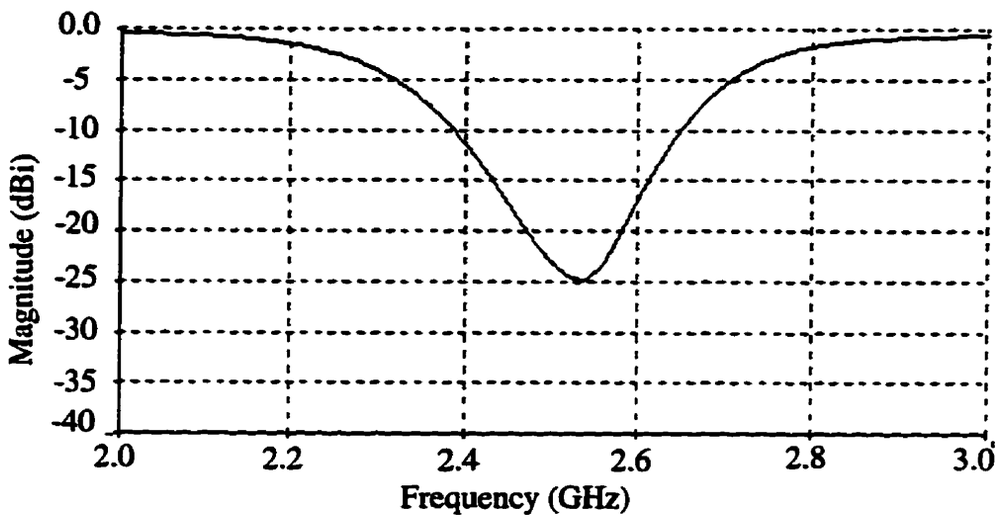

Figure 4.4: Computed return loss of the stacked ring-patch configuration, W_2/W_1=15/30, W_3=47 mm, H_1=1.6 mm, H_2=5 mm, ε_{r1} =2.5, ε_{r2} = 1.05

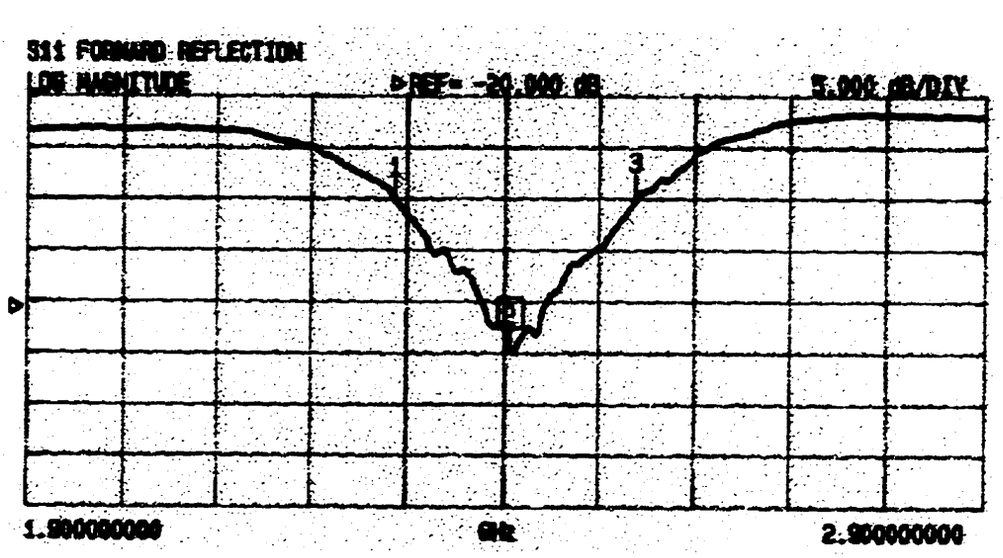

Figure 4.5: Measured return loss of the stacked patch configuration, of Figure 4.4

Figures 4.4 and 4.5 show the computed S11 and its corresponding measured results. They agree well. From Figs 4.4 to 4.6, the resulting bandwidth, for a VSWR<2, is about 10.5 percent

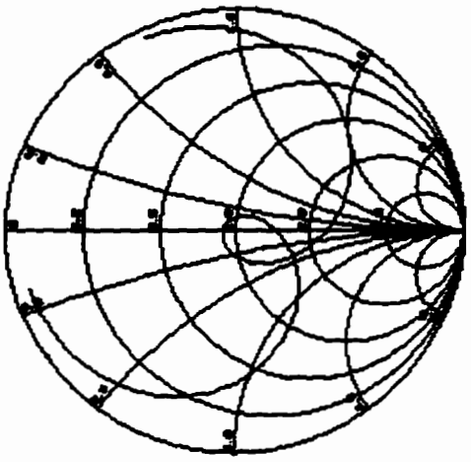

(a)

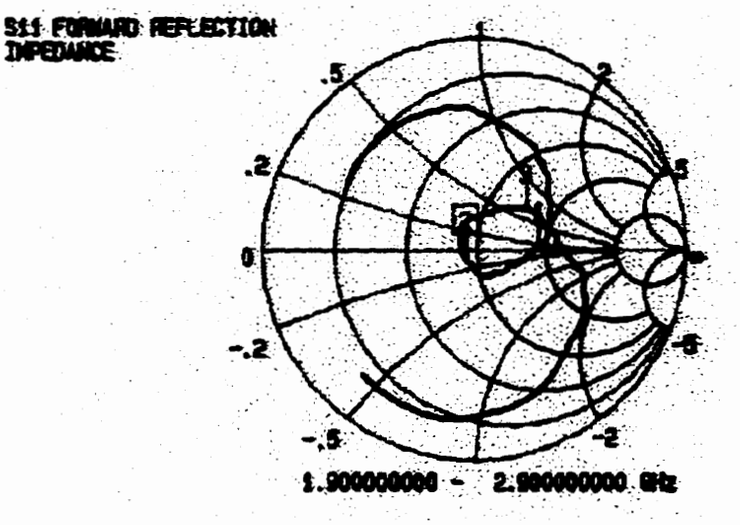

(b)

Figure 4.6: (a) Computed, (b) measured input impedance of ring-patch antenna of Figure 4.4

For the ring-patch antenna the 3dB beamwidths are 65° (H-plane) and 75° (E-plane), having a difference of 10 degrees. Figures 4.7 to 4.9 give the midband calculated and measured radiation patterns in both E and H planes.

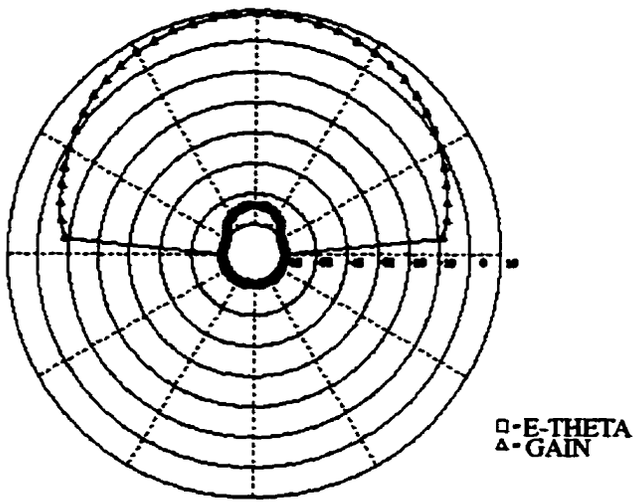

(a)

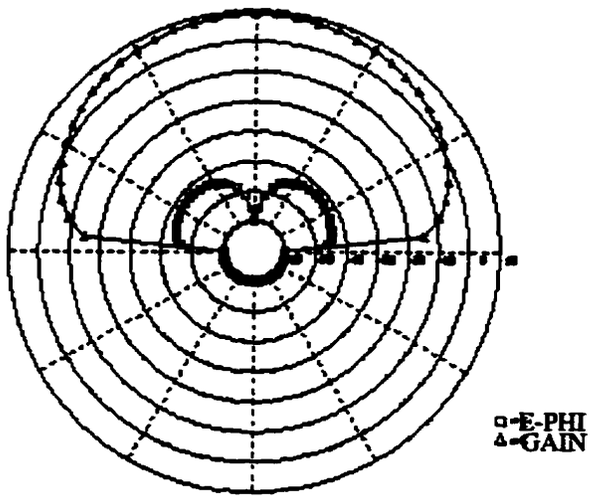

(b)

Figure 4.7: Computed (a) H-plane and (b) E-plane radiation patterns with normalized cross-polarization of Figure 4.4

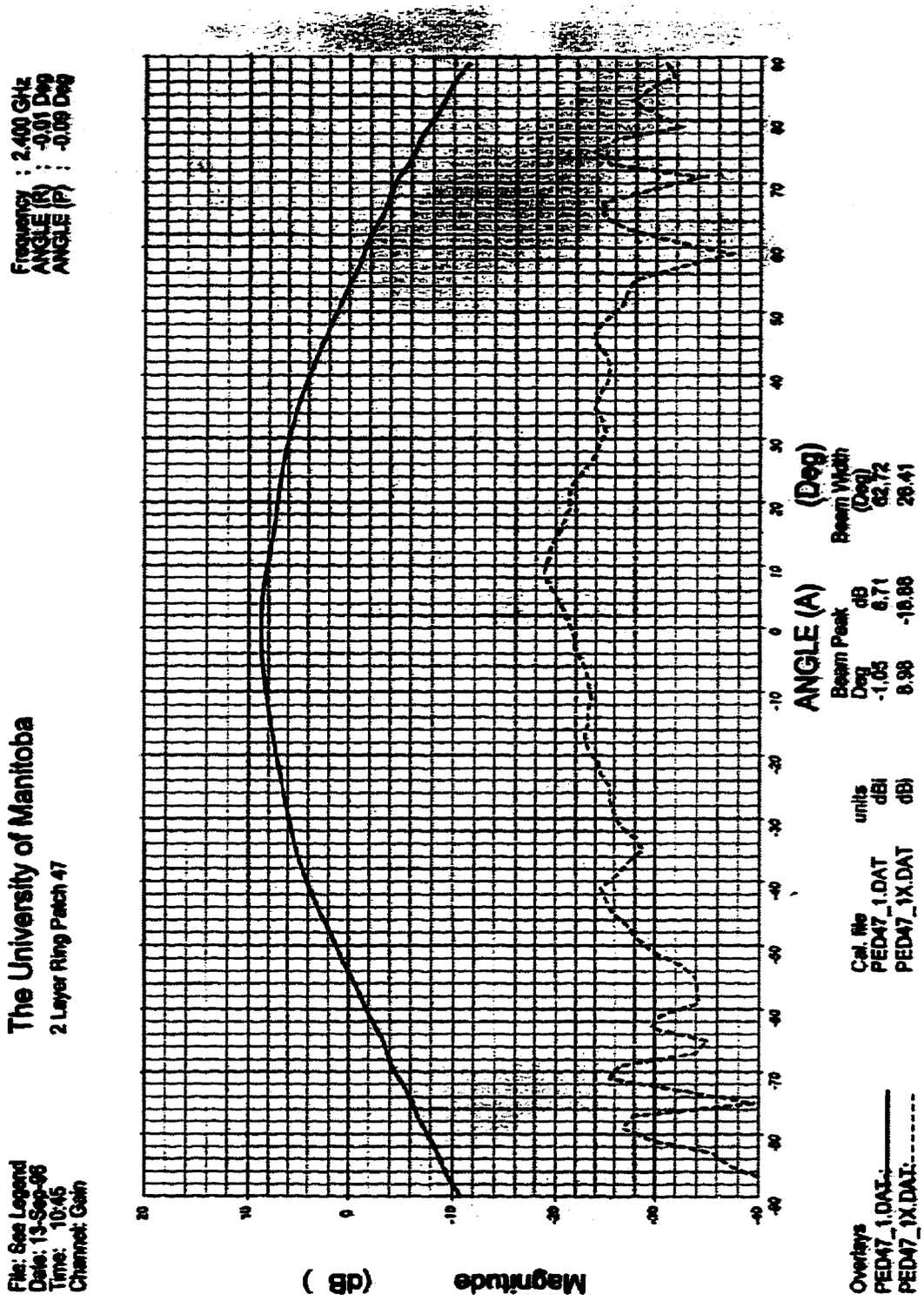

Figure 4.8: Measured E-plane radiation pattern for ring-patch antenna. of Figure 4.4 (ground plane is 100mm)

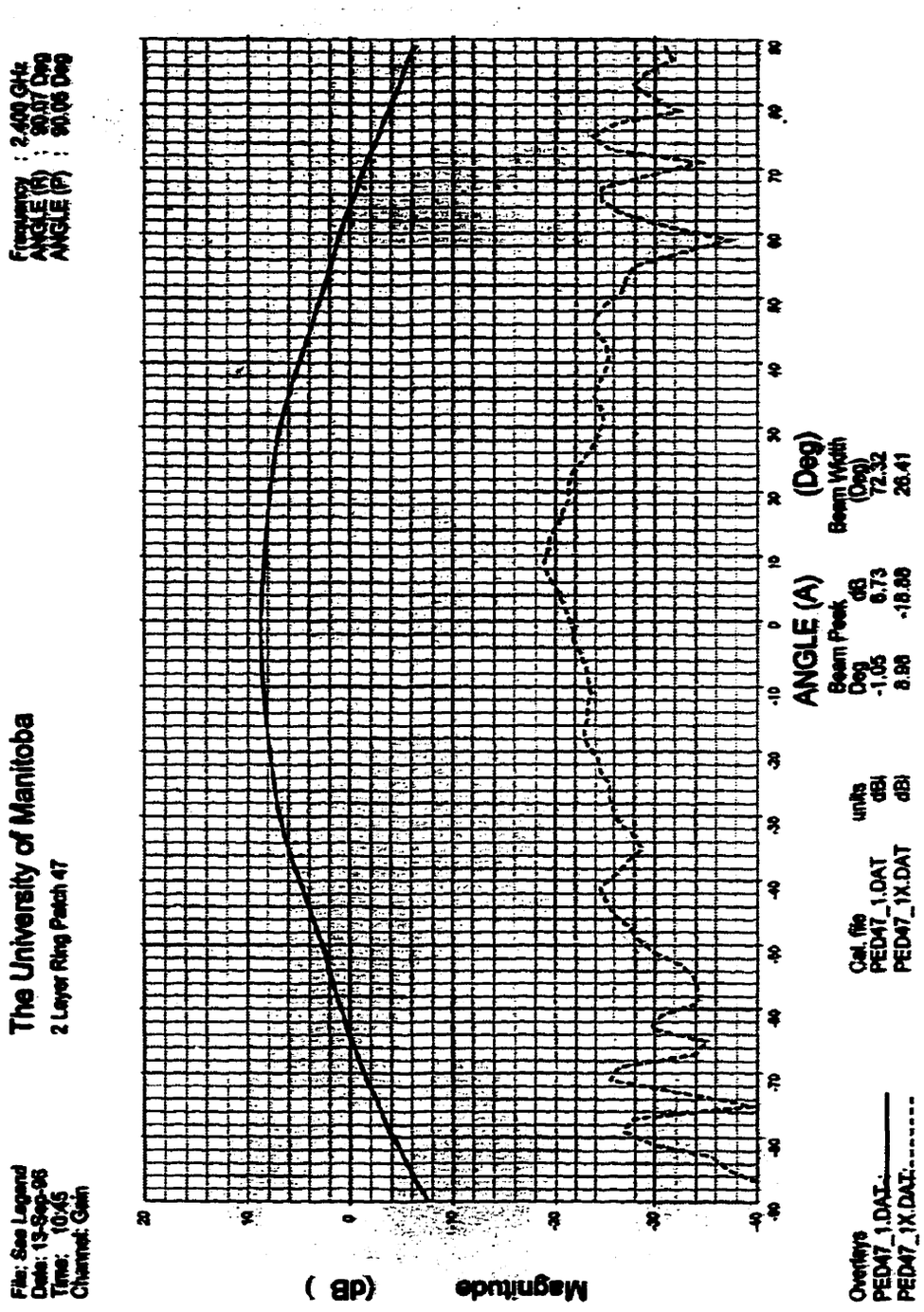

Figure 4.9: Measured H-plane radiation pattern of ring-patch antenna of Figure 4.4 (ground plane is 100 mm)

Their overall shapes are comparable except for the cross-polarization which is slightly higher in measurement. This is due to imperfection in fabrication and alignment of the ring with patch. The measured gain of this structure is 8.7 dBi.

The current on the surfaces of ring and patch are also computed and shown in Fig. 10. On the ring, the current intensity is high, and undergoes rapid variation at corners, which deteriorate the solution convergence in simulation.

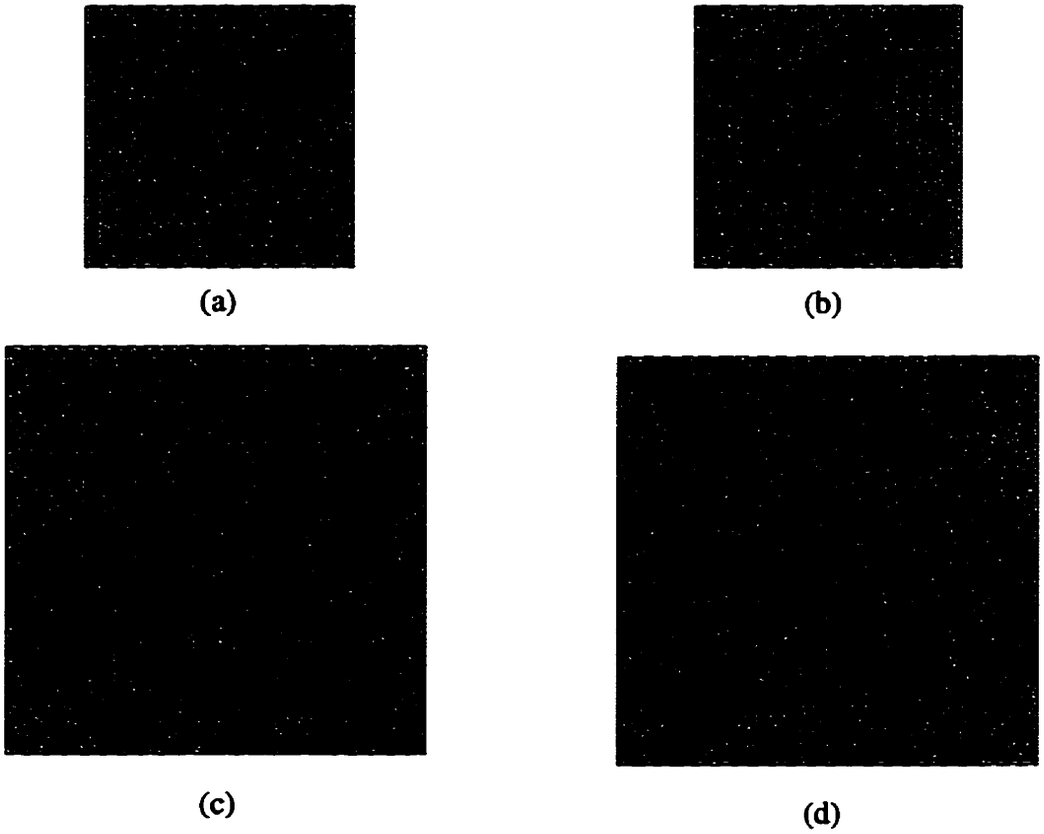

Figure 4.10: Real and imaginary normalized surface current components (a) Real current component on ring, I_{Rmax} = 0.002974 (b) Imaginary current component on ring, I_{Imax} = 0.010179 (c) Real current component on patch, I_{Rmax} = 0.008304 (d) Imaginary current component on patch, I_{Imax} = 0.003236

4.4.Stacked Ring-Ring

For stacking, it is possible to use another ring instead of the patch [35], to not only enhance the bandwidth, but also to reduce the total size of the antenna. The geometry of the antenna is shown in Figure4.11. It consists of a two layer ring with ε_{r1} =2.5, H_1 =1.5 mm, W_1 =30 mm, W_2 =14 mm, ε_{r2} = 1.05 (foam) H_2=5 mm, W_3=36 mm, W_4 =22 mm, d=1.27 mm, X_p=0 mm and Y_p= -13 mm,(X_p,Y_p are shown in Figure 2.2) which was designed and simulated.

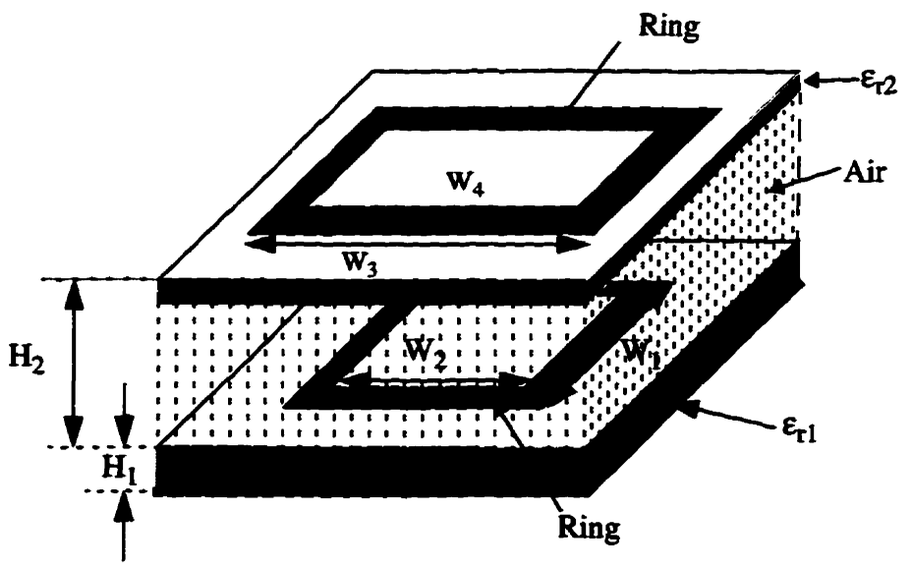

Figure 4.11: Configuration of stacked ring-ring antenna

One sample was fabricated and tested by "HP 8722C" network analyser and its midband radiation pattern measured in the "Anechoic Chamber". They are shown in Figure 4.12 to 4.17. Good agreement between the theory and experiment is observed for a coaxially fed antenna.

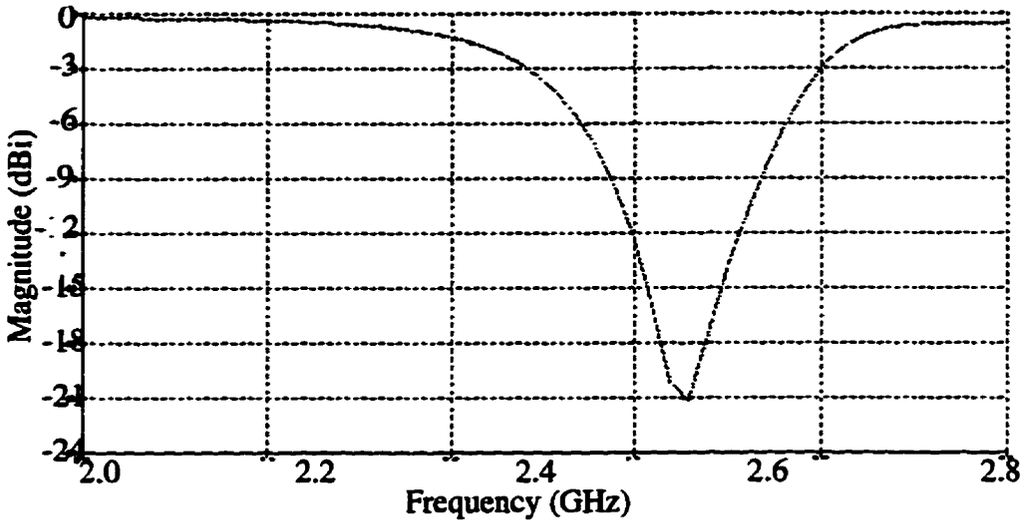

Figure 4.12: Computed return loss of the stacked rings, W_2/W_1=14/30, W_4/W_3=22/36,H_1=1.6 mm, H_2=5 mm, ε_{r1} =2.5, ε_{r2} = 1.05

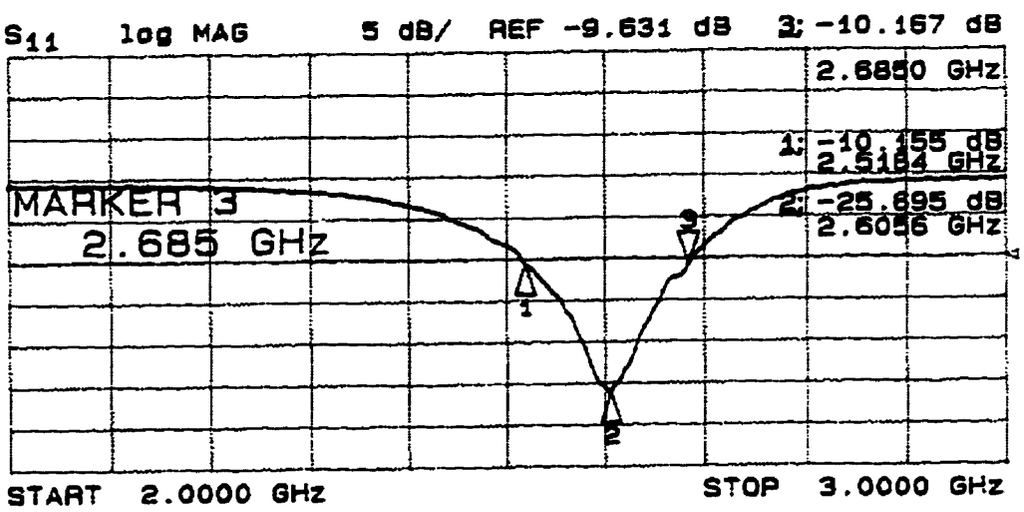

Figure 4.13: Measured return loss of the stacked rings of Figure 4.12

In numerical computation, the cell size for the top layer is $0.026\lambda_0$, and for the bottom layer $0.017\lambda_0$, where λ_0 is the wavelength at midband frequency of 2.6 GHz.

From Figures 4.12 to 4.14, the resulting bandwidths, for a VSWR<2, were about 6.4% experimentally, and 5.4% by simulation.

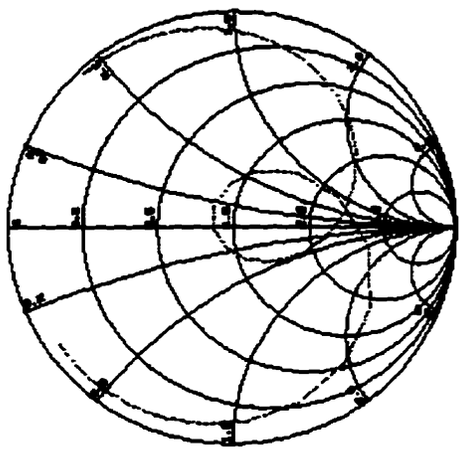

(a)

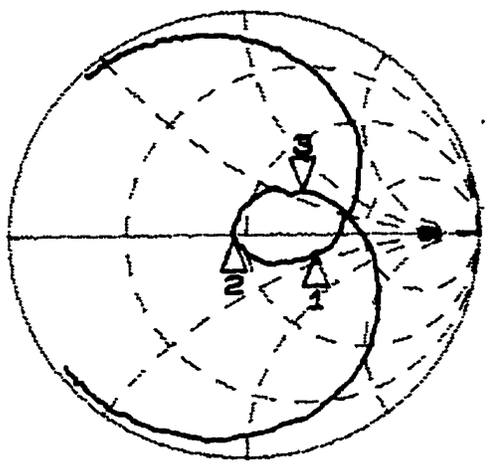

(b)

Figure 4.14: (a) Computed, (b) measured input impedance of stacked ring antenna of Figure 4.12

For the ring-ring antenna the 3dB beamwidths are 61° (H-plane) and 74° (E-plane), having a difference of 13 degrees. The overall shapes of measured and simulated results are comparable except for the cross-polarization which is slightly higher in the measurement, which is due to imperfection in fabrication alignment of the two layer rings. The Gain of this structure was found to be 8.0 dBi.

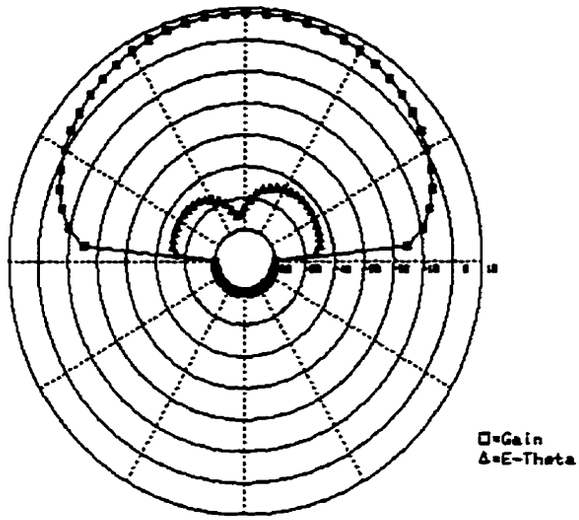

(a)

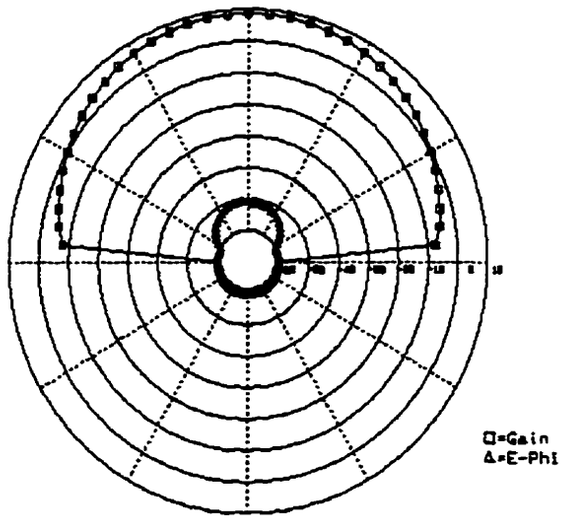

(b)

Figure 4.15: Computed (a) H-plane (b) E-plane radiation pattern of Figure 4.12

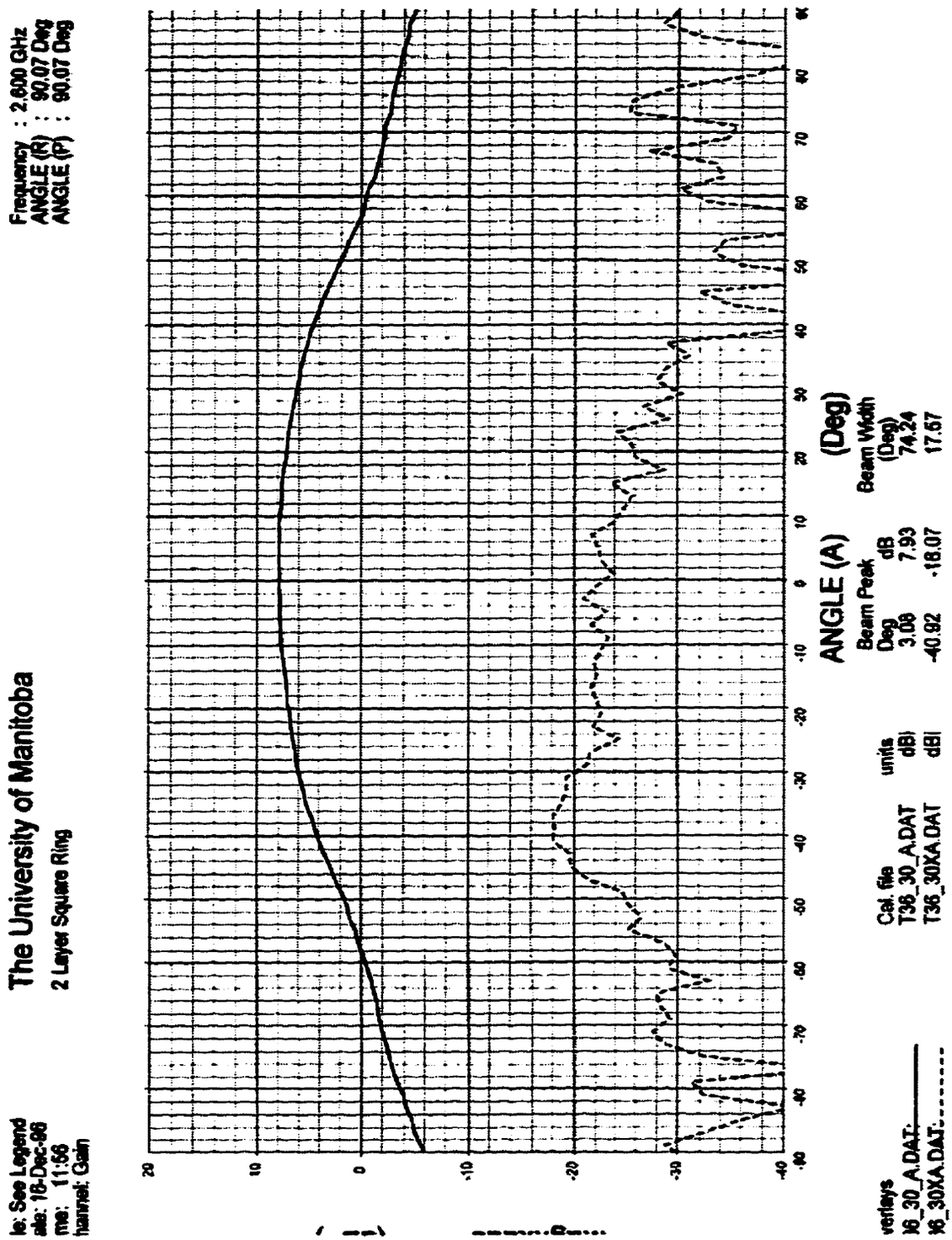

Figure 4.16: Measured H-plane radiation pattern with cross-polarization for Figure 4.12 (ground plane is 100 mm)

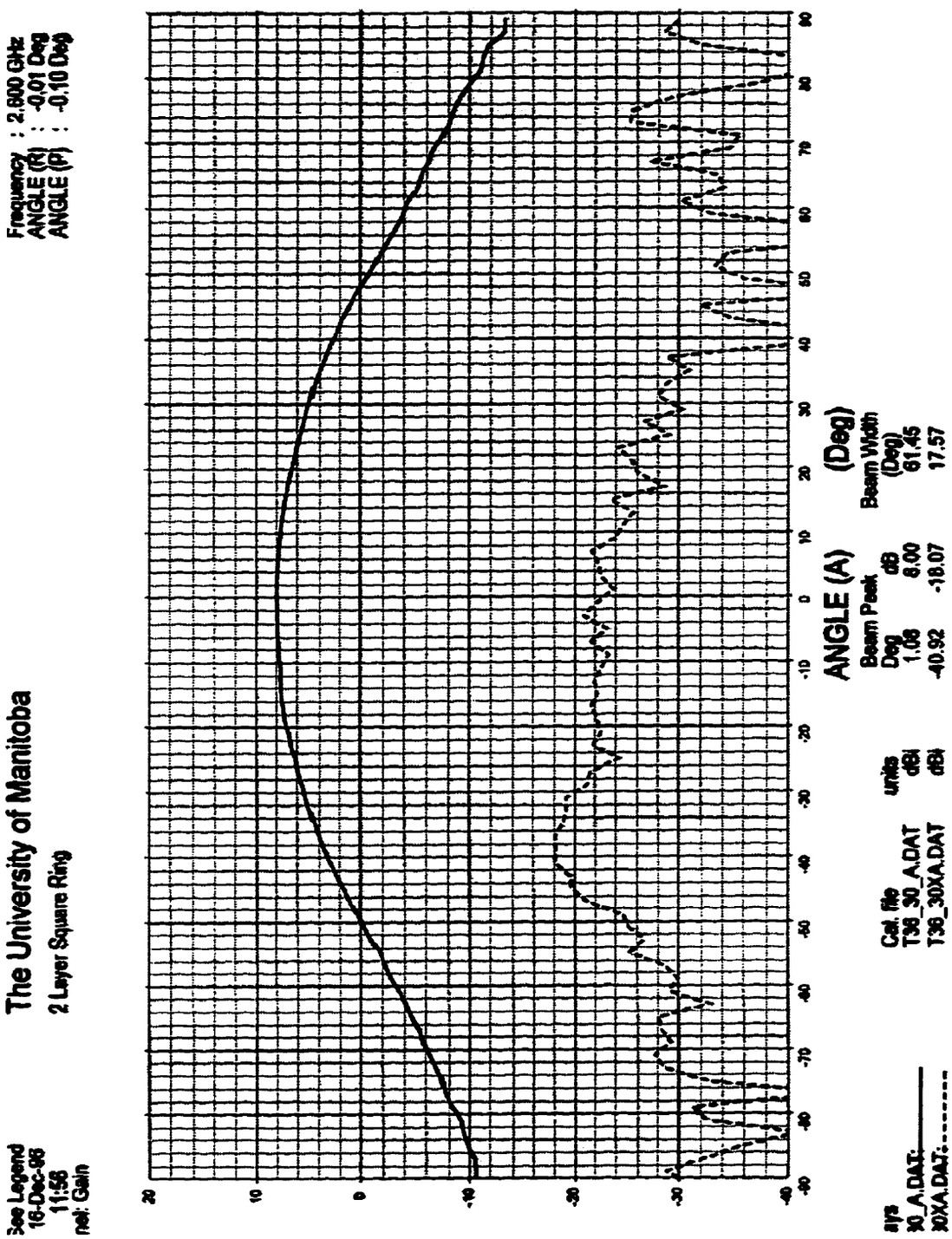

Figure 4.17: Measured E-plane radiation pattern with cross-polarization for Figure 4.12 (ground plane is 100 mm)

The current distribution on the surfaces of the rings was also computed and is shown in Figure 4.18.

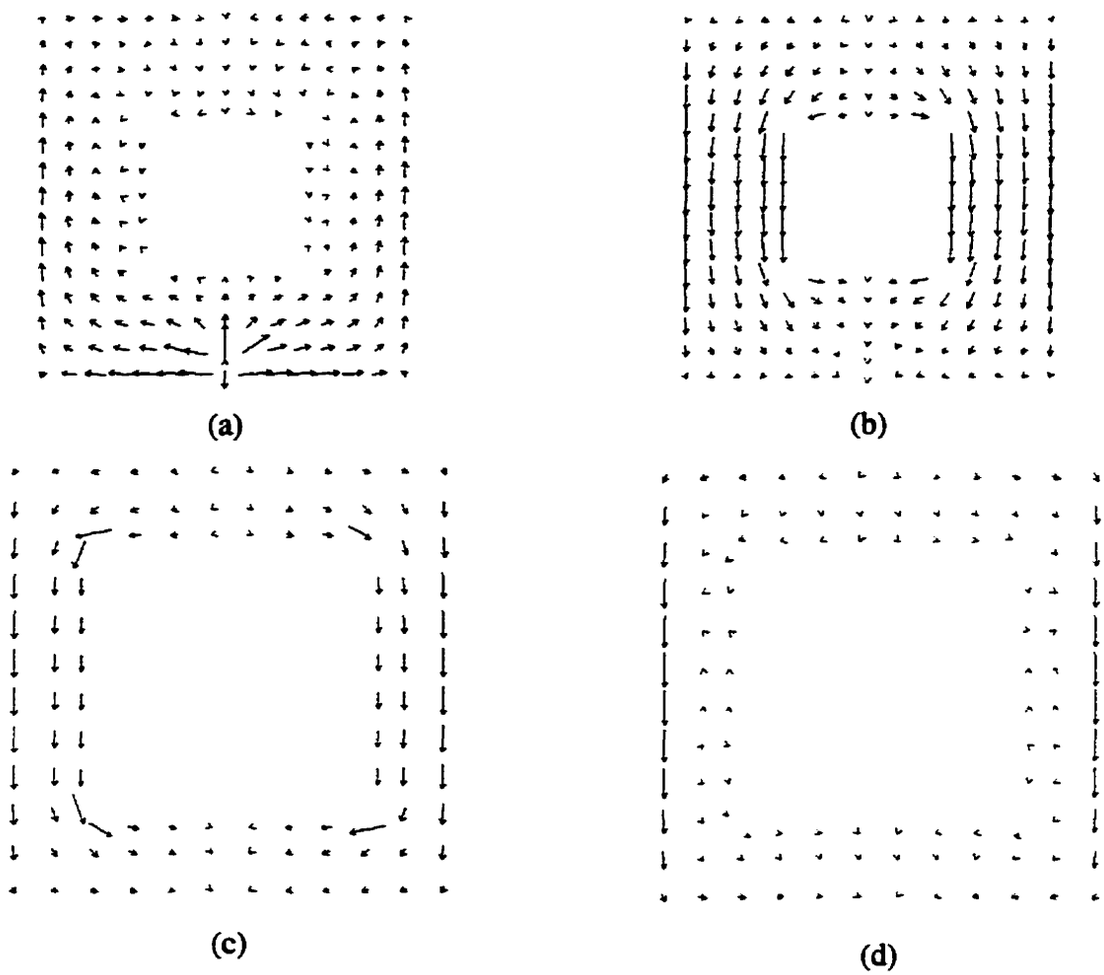

Figure 4.18: Real and imaginary normalized surface current components (a) Real current component on lower ring, I_{Rmax} = 0.005615 (b) Imaginary current component on lower ring, I_{Imax} = 0.009578 (c) Real current component on upper ring, I_{Rmax} = 0.019038 (d) Imaginary current component on upper ring, I_{Imax} = 0.002046

4.4.1. The effect of changing H_1

To consider the effect of changing the lower substrate thickness, two practical cases were simulated.

For the first case, the lower substrate thickness, with ε_r=2.5, is assumed to be 3.2mm. The other parameter are as follows: W_1 =30 mm, W_2 =15 mm, ε_{r2} = 1.05 (foam) H_2=5 mm, W_3=42 mm, W_4 =14 mm, d=1.27 mm, X_p=0 mm and Y_p= -13 mm.

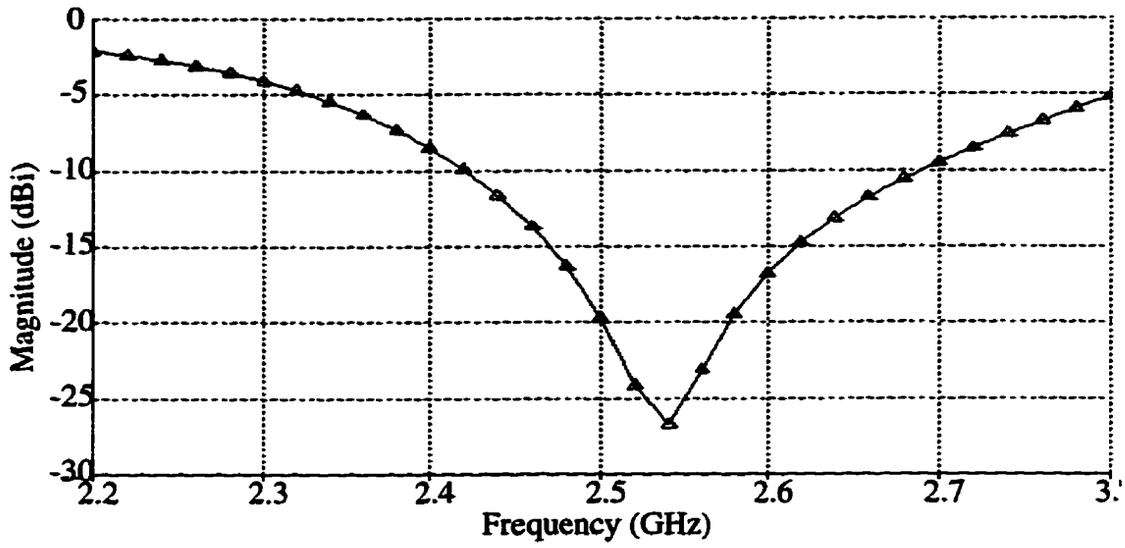

(a)

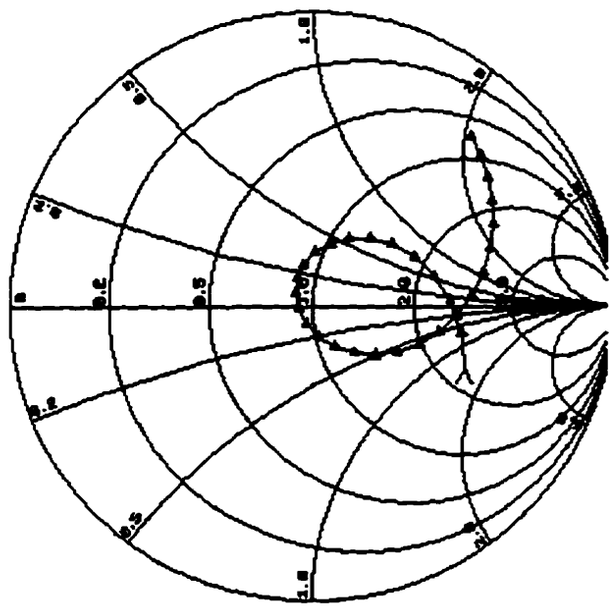

(b)

Figure 4.19: (a) Return loss and (b) input impedance for a stacked ring-ring antenna with H_1=3.2 mm

From Figure 4.19, the resulting bandwidth, for a VSWR<2, is about 11% by simulation. For this case, the 3dB beamwidths are 72° (H-plane) and 74° (E-plane), having a difference of 2 degrees.The Gain of this antenna is 8.2 dBi.

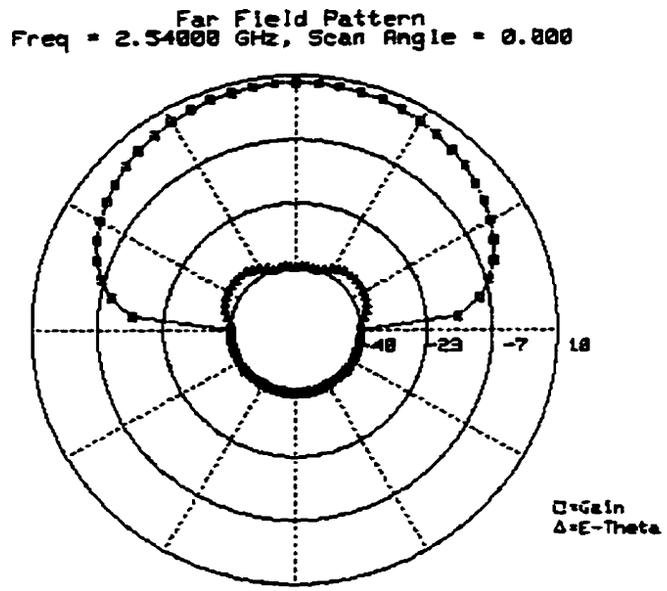

(a)

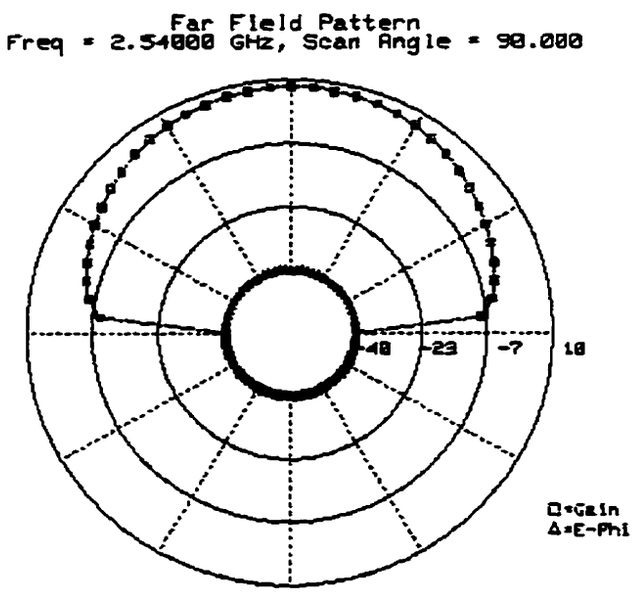

(b)

Figure 4.20: (a) H-plane, (b) E-plane radiation pattern of Figure 4.19

For the second case, the lower substrate thickness, with ε_r=2.5, is assumed to be 0.8 mm. The other parameters are as follows: W_1 =30 mm, W_2 =15 mm, ε_{r2} = 1.05 (foam) H_2=5 mm, W_3=42 mm, W_4 =22 mm, d=1.27 mm, X_p=0 mm and Y_p= -13 mm.

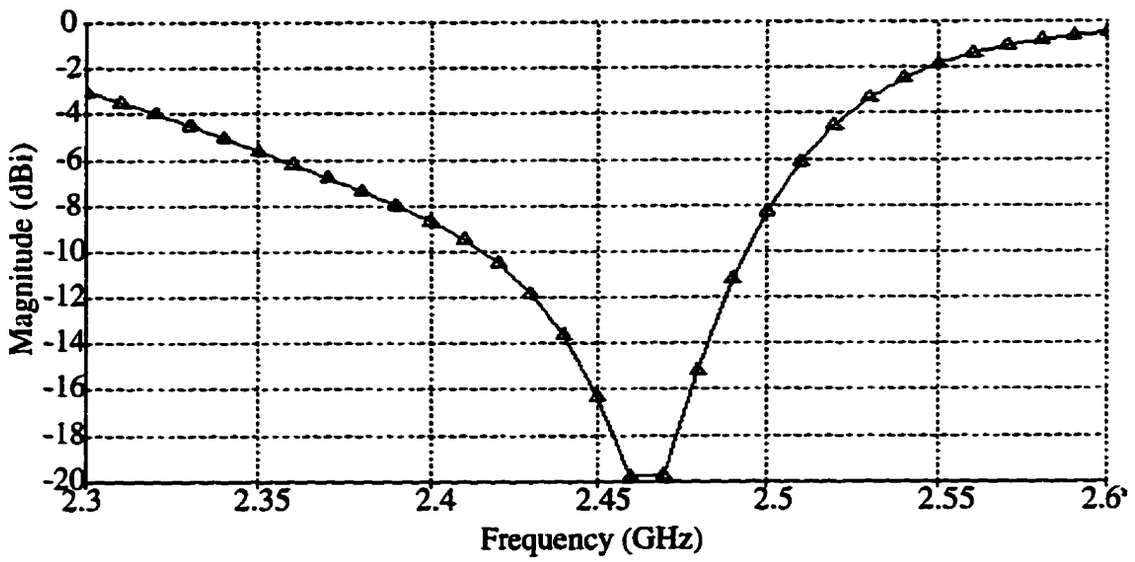

(a)

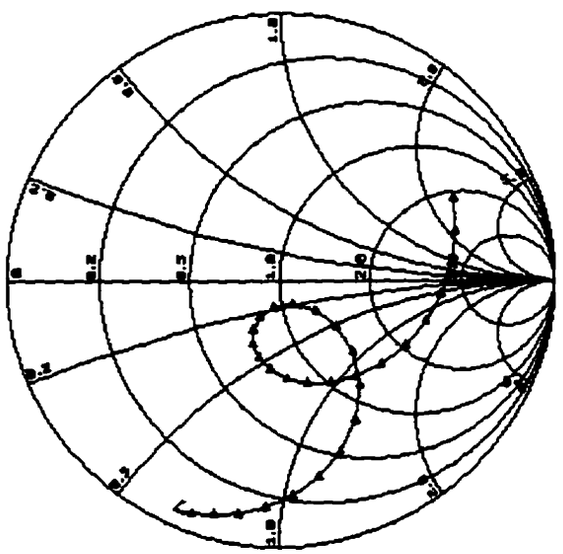

(b)

Figure 4.21: (a) Return loss, (b) input impedance for a stacked ring-ring configuration with H_1=0.8

From Figure 4.21, the resulting bandwidth, for a VSWR<2, is about 4.06% by simulation. For this case, the 3dB beamwidths are 70° (H-plane) and 60° (E-plane), having a difference of 10 degrees.The gain of this antenna is 9.15 dBi.

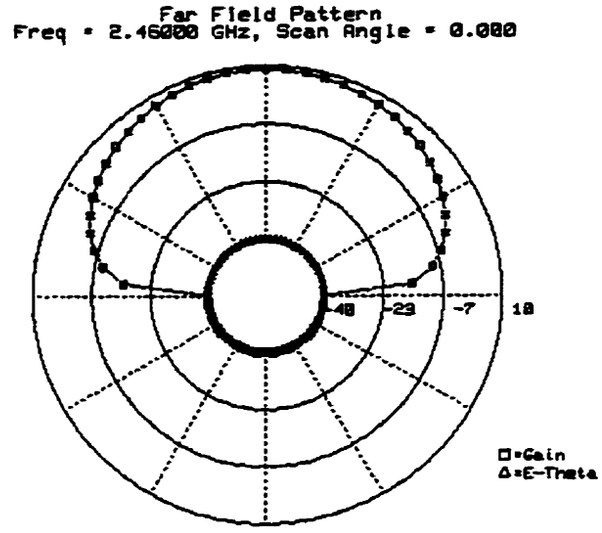

(a)

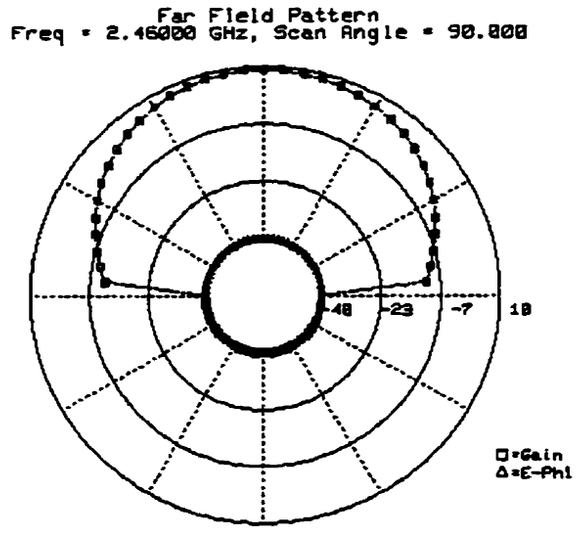

(b)

Figure 4.22: (a) H-plane, (b) E-plane radiation pattern of Figure 4.21

By comparing the results of three substrate heights, one can conclude that increas-

ing the lower substrate thickness increases the bandwidth of the stacked structure.

4.4.2. The effect of changing H_2

The best value for H_2 in the last section was 5 mm, however it is not constant and varies with the resonance frequency. To show the effect of changing the frequency on H_2, a new design is developed for a lower resonance frequency of 1.150 GHz.

This design consists of a stacked ring-ring configuration with ε_{r1} =2.5, H_1 =0.8 mm, W_1 =60 mm, W_2 =30 mm, ε_{r2} = 1.05 (foam) H_2=9 mm, W_3=90 mm, W_4 =45 mm, d=1.27 mm, X_p=0 mm and Y_p= -28 mm.

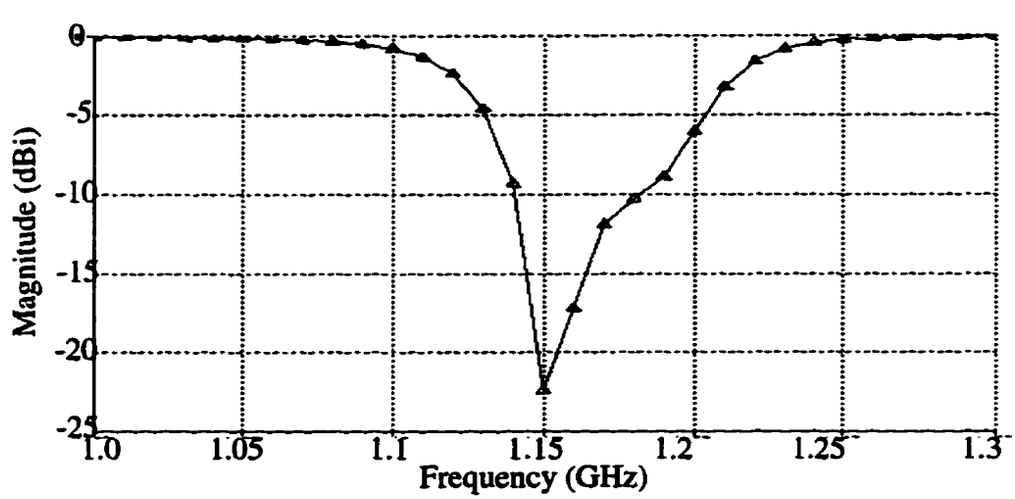

Figure 4.23: Return loss for a stacked ring-ring antenna H_2=9 mm and H_1=0.8mm, W_2/ W_1=30/60, W_4/W_3=45/90, ε_{r1} =2.5, ε_{r2} = 1.05

From Figure 4.23, the resulting bandwidth, for a VSWR<2, is about 4.34% by simulation. For this case, the 3dB beamwidths are 72° (H-plane) and 68° (E-plane), having a difference of 4 degrees.The gain of this antenna is 9.03 dBi.

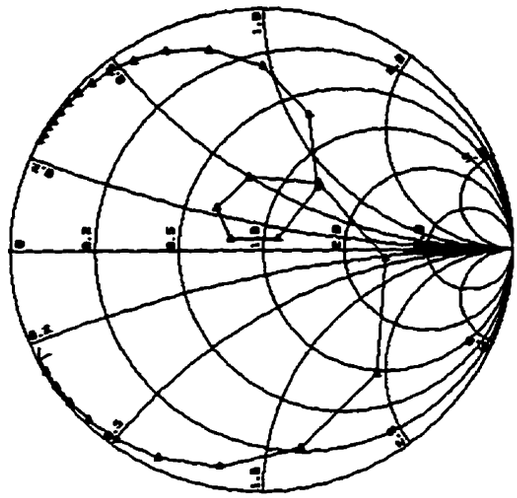

Figure 4.24: input impedance for antenna of Figure 4.23

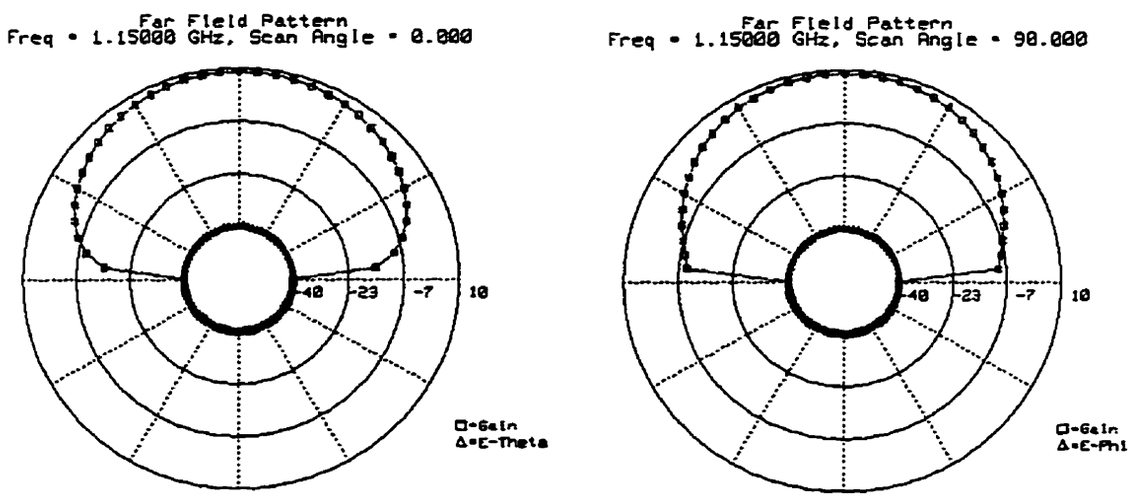

(a) *(b)*

Figure 4.25: (a) H-plane, (b) E-plane radiation pattern for Figure 4.23

4.4.3. The effect of using different substrates

In previous sections, the lower substrate dielectric constant was 2.5, which is an expensive material, specially at low frequencies when the dimensions of antenna increase. To overcome this problem, a new design with a foam substrate is performed.

This design consists of a two layer ring-ring configuration with ε_{r1} =1.05, H_1 =9 mm, W_1 =350 mm, W_2 =700 mm, ε_{r2} = 1.05 (foam) H_2=18 mm, W_3=700 mm, W_4 =230 mm, d=1.27 mm, X_p=0 mm and Y_p= -180 mm.

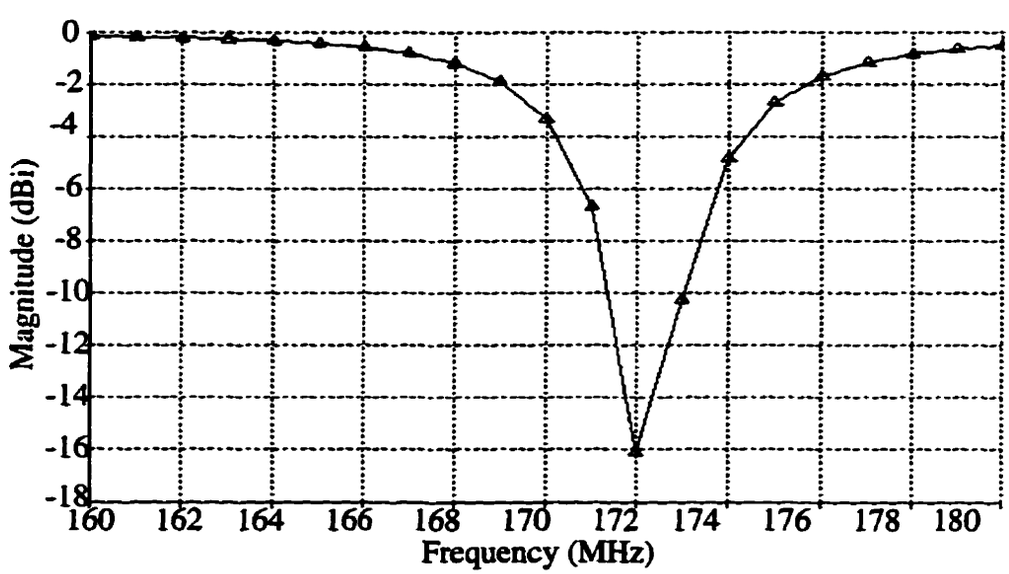

Figure 4.26: Return loss for two layer ring-ring antenna with $\varepsilon_{r1}=\varepsilon_{r2}=1.05$, $H_2=18$ mm and $H_1=9$ mm, $W_2/W_1=350/700$, $W_4/W_3=230/700$

From Figure 4.26, the resulting bandwidth, for a VSWR<2, is about 1.1% by simulation. For this case, the 3dB beamwidths are 70° (H-plane) and 64° (E-plane), having a difference of 6 degrees.The gain of this antenna is 9.34 dBi.

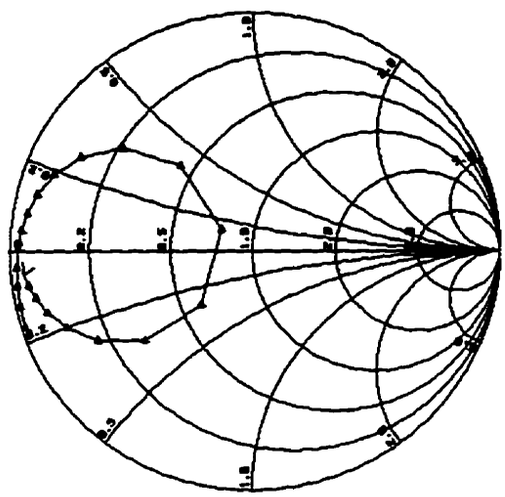

Figure 4.27: Input impedance for two layer ring for antenna of Figure 4.26

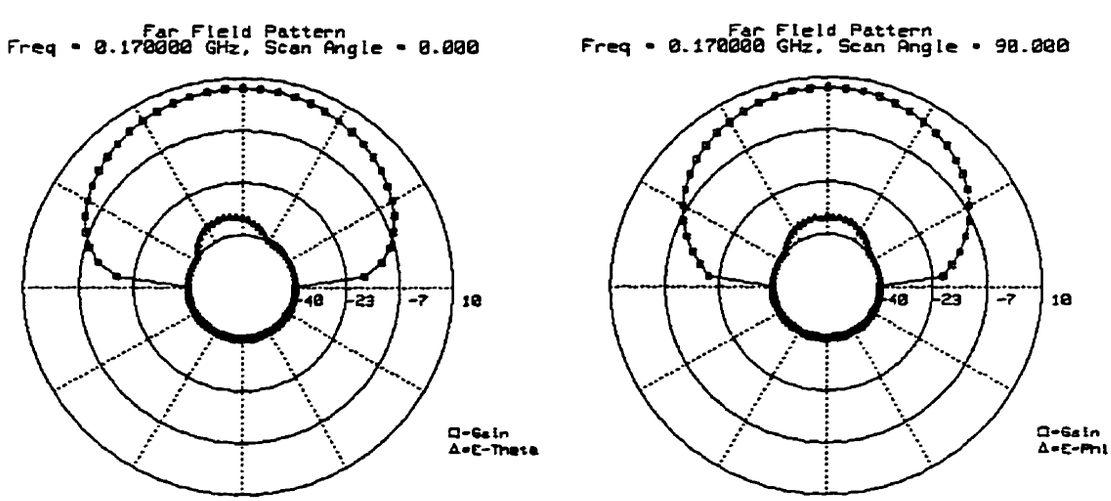

(a) *(b)*

Figure 4.28: (a) H-plane, (b) E-plane radiation pattern for Figure 4.26

4.5.Summary

In this chapter a stacked configuration was used to match the input impedance of the square ring to a 50Ω transmission line. Also with this technique the bandwidth of the structure was considerably enhanced.

Different designs were developed and investigated. In the first design, the lower resonator was a ring and the upper one a patch. A bandwidth of 10.5% and gain of 8.7dBi were obtained. Then, the upper patch was replaced by a another ring, resulting in a ring-ring configuration. For this case, several samples were simulated and realized. In all cases, the gain was almost constant and was around 9 dBi. The bandwidth depended on the lower and upper substrate thicknesses and could be tuned by properly choosing the heights. The overall shape of radiation pattern for all of these samples were almost the same.

Chapter 5

CONCLUSION

5.1.Summary

A study was carried out to determine the effects of removing the central conducting portion of the microstrip square patch antennas on their radiation characteristics. A numerical method based on a full-wave approach using mixed potential integral formulation in conjunction with the method of moment was utilized. In this method the resonance frequency, input impedance, current distribution, and radiation pattern are computed accurately. Adequate measurements were performed to confirm the computed results.

The bandwidth of this configuration was enhanced by using a stacked configuration. Then, a novel transmission-line model was developed to predict its resonance frequency.

The following conclusions were drawn:

☞ Perforating the square patch to become a square ring has significant effect on its resonance frequency and input impedance. The resonance frequency decreases by increasing the size of perforation and this reduction is faster for thinner substrates. By decreasing the ring width, the input impedance increases rapidly and also the bandwidth reduces at a faster rate than the size reduction. Inspite of reduction in

the antenna size, the directivity remains constant and does not change by modifying substrate thickness. Also, the perforation on conducting portion causes current discontinuities and therefore, results in rapid variation in its magnitude and direction.

☞ The transmission-line model can be deployed successfully to predict the resonance frequency of microstrip square ring antennas. This model is based on improved transmission-line model, where two more slots are added to consider the effects of the perforation area. These two slots bring new circuit elements to the model.

☞ For matching the square ring antenna to any impedance and also enhancing its bandwidth a stack technique was used. In this method both a patch, and another ring were used. The bandwidth and also input impedance of these structures were tuned by changing the substrate thickness and permittivity. The resonance frequency of this antenna was to be independent of the ring sizes.

5.2.Future Research

In this area, there are numerous subjects which need more careful investigations, some of which are listed below.

☞ A study on the effect of finite ground plane on the gain and other radiation charac-

teristics and possibility of controlling these parameters.

- Developing a new transmission-line model, which will be able to calculate the input impedance and radiation pattern of the microstrip square ring antennas.

- Because microstrip ring resonator size is smaller than the solid patch, it can be used in arrays effectively without creating grating lobes.

- Active device integration can be achieved easily to realize adaptive antennas using open ring microstrip elements.

- The bandwidth of square ring patches can also be increased by loading concentric square ring elements which operate at closed frequencies.

REFERENCES

[1] G.A. Deschamps, "Microstrip microwave antennas," *presented at the 3rd USAF Sypo-sium On Antannas*, 1953

[2] J.Q. Howell, "Microstrip antennas," *IEEE Trans. AP-S Int. Symp. Digest*, pp. 177-180, 1972

[3] R.E. Munson, "Conformal microstrip antennas and microstrip phased arrays," *IEEE Trans. Antennas Propag.*, vol. Ap-22, pp. 74-78, 1974

[4] L. Shafai, "Characteristics of printed ring antennas," *Symposium on Antenna Technology and Applied Electromagnetics, ANTEM 96*, pp. 379-382, Montreal, August 1996

[5] J.Q. Howell, "Microstrip antennas," *IEEE Trans. Antennas Propag*, AP-23, pp. 90-93, 1975

[6] A.G. Derneryd, "Extended analysis of rectangular microstrip resonator antenna," *IEEE Trans. Antennas Propag*, AP-27, pp. 846-849, 1979

[7] H. Pues, and A. Van De Capelle, "Accurate transmission-line model for rectangular microstrip antenna," *IEE Proc.*, 131H, pp.334-340, 1984

[8] J.R. Mosig, and F.E. Gardiol, "Analytical and numerical techniques in the Green's function treatment of microstrip antennas and scatterers," *IEE Proc.*, 132H, pp.424-432, 1985

[9] J.R. James, P.S. Hall, and C. Woods, "Microstrip antenna theory and design," Peter peregrinus, 1981.

[10] Y.T. Lo, D. Solomon, and W.F. Richards, "Theory and experiment on microstrip antennas," *IEEE Trans. Antennas Propag*, AP-27, pp. 137-145, 1979

[11] W.F. Richards, Y.T. Lo, and D.D. Harrison, "An improved theory for microstrip antennas and applications," *IEEE Trans. Antennas Propag*, AP-29, pp. 38-46, 1981

[12] I.J. Bahl, and P. Bhartia, "Microstrip antenns," Dedham, Massachusetts: Artech House, 1982

[13] K. Antoskiewicz, and L. Shafai, "Impedance characteristics of circular microstrip patches," *IEEE Trans. Antennas Propag*, AP-38, pp. 942-946, 1990.

[14] W.J. Bergman, and F.V. Schultz, "The circular traveling-wave antenna," *IRE Int. Conv. Rec.*, vol. 3, pt. 1, pp. 40-50 1955.

[15] Y.S. Wu, and F.J. Rosenbaum, "Mode for microstrip ring resonator," *IEEE Trans. Microwave Theory Tech.*, MTT-21, pp. 487, 1973.

[16] S. Pintzos, and R. Pregla, "A simple method for computing the resonant frequencies of microstrip ring resonator," *IEEE Trans. Microwave Theory Tech.*, MTT-26, pp. 809, 1978.

[17] I.J. Bahl, and S.S. Stuchly, and M.A. Stuchly, "A a new microstrip radiator for medical application," *IEEE Trans. Microwave Theory Tech.*, MTT-28, pp. 1464 1980.

[18] J.W. Mink, " Cicular ring microstrip antenna elements,"*IEEE Trans. AP-S Int. Symp. Digest*, pp. 605-608, 1980.

[19] S.A. Long, and M.D. Walton, "A dual-frequency, stacked circular disc antenna," *IEEE Trans. AP-S Int. Symp. Digest*, pp. 260-263, 1978

[20] R.T. Cock, and C.G. Christofedoulu, "Design of a two-layer, capasitively coupled, microstrip patch antenna element for broadband applications,"

[21] F. Croq, "Stacked resonator for bandwidth enhancment, a comparison of two feeding techniques," *IEE Proc.*, 140H, pp.303-309, 1993

[22] J.P Damiano et al., "Study of multilayer microstrip antennas with radiating elements of various geometry," *IEE Proc.*, 137H, pp.163-170, 1990.

[23] A.G. Derneryd, "Linearly polarized microstrip antennas," *IEEE Trans. Antennas Propag*, AP-24, pp. 846-851, 1976.

[24] E.O. Hammerstad, "Equations for microstrip circuit design," *in proceeding of the 5th European Microwave Conference*, pp. 268-272. Sept 1975.

[25] L. Shafai, and W. Chamma, "Bandwidth and polarization characteristics of perforated patch antennas," *IEE Int. Conference on Antenna Propag.*, pp. 43-46 1997.

[26] ENSEMBLE "Design, Review, & 1D Array Synthesis User's Guide," Boulder Microwave Technologies, Inc. 1995.

[27] J.R. James, and P.S. Hall, "Handbook of microdtrip antenna," vol. 1 Peter peregrinus,

1989.

[28] H.G. Oltman, and D.A. Huebner, "Electromagnetically coupled microstrip dipoles," *IEEE Trans. Antennas Propag*, AP-29, pp. 151-157, 1981.

[29] R.E. Collin and F.J. Zucker, "Antenna Theory" part I, NewYork: McGraw-Hill 1969.

[30] E. Van Lil, and A. Van De Capelle, "Transmission line model for mutual coupling between microstrip antennas," *IEEE Trans. Antennas Propag*, AP-32, pp. 816-821, 1984.

[31] T. Itoh, "Numerical Techniques for microwave and millimeter-wave passive structures" John Wiley & Sons 1989.

[32] E.H. Fooks, and R.A. Zakarevicius, "Microwave engineering using microstrip circuits," Prentice Hall of Australia Pty Ltd. 1990.

[33] K.C. Gupta, "Class notes for microwave circuit," University of Colorado, Boulder.

[34] P. Moosavi, and L. Shafai, "Characteristics and design of microstrip sqaure ring antennas", *5th Iranian Conference in Electrical Engineering ICEE97*, May, 1997

[35] P. Moosavi, and L. Shafai, "Stacked square ring resonators for bandwidth enhancment" *IEEE Trans. AP-S Int. Symp. Digest*, pp. 944-947, 1997